Continuous Solar Vapour Generation and Salt Harvesting from Seawater

Xiaolong Ma

Submitted in accordance with the requirements for the degree of
Doctor of Philosophy

The University of Leeds

School of Chemical and Process Engineering

June 2022

The candidate confirms that the work submitted is his own, except where work which has formed part of jointly-authored publications has been included. The contribution of the candidate and the other authors to this work has been explicitly indicated below. The candidate confirms that appropriate credit has been given where reference has been made to the work of others.

Parts of this thesis are based on work as follows which has been either published in academic journals or submitted in reviewing:

Xiaolong Ma, Xiaodong Jia, Hui Gao and Dongsheng Wen. 2021. Polypyrrole–Dopamine Nanofiber Light-Trapping Coating for Efficient Solar Vapor Generation. *ACS Applied Materials & Interfaces*, 2021, 13 (48), 57153-57162.

Xiaolong Ma, Xiaodong Jia, Guice Yao and Dongsheng Wen. Umbrella Evaporator for Continuous Solar Vapor Generation and Salt Harvesting from Seawater. *Cell Reports Physical Science*, 2022, 3 (7), 100940.

Xiaolong Ma, Xiaodong Jia, Guice Yao and Dongsheng Wen. Double-sided suspending evaporator with top water supply for concurrent solar evaporation and salt harvesting. *ACS Sustainable Chemistry & Engineering*, 2022.

As co-author, the candidate also provided data collection, result analysis and evaluation for the following papers:

Xia, D., Xu Y., Mannering, J., Ma, X.L., Ismail, M.S., Borman, D., Baker, D.L., Pourkashanian, M. and Manzel, R. 2020. Tuning the Electrical and Solar Thermal Heating Efficiencies of Nanocarbon Aerogels. *Chemistry of Materials*, 2020, 33 (1), 392-402.

Acknowledgements

This work was carried out thanks to the funding from China Scholarship Council (CSC).

First and foremost, I would like to extend my deepest gratitude to my supervisor, Prof. Dongsheng Wen, for his support, encouragement and providing me adequate laboratory equipment. He can always help me find the direction of my project and extract its core value. Every time talking with him, I can always feel a kind of power to make me positive. He sets me on fire in scientific research and sails my academic career. I would also like to extend my appreciation to my co-supervisor, Dr Xiaodong Jia, for his encouragement and suggestions during my study. The mentoring and support from them both help me a lot in my PhD career. I also would like to thank Dr Xiaojun Lai for his excellent management for the lab.

I also would like to thank Ben Douglas, Mohammed Javed, Stuart Micklethwaite John Harrington, Karine Alves Thorne, Adrian Cunliffe and Simon Lloyd for their technical training and help in characterizations.

I also would like to thank Zhongliang Hu, Guice Yao, Zeyu Kang, Maje Alhaji Haruna, Hangyu Chen, Shudan Wei, Lina Yang, Jiatong Jiang, Cheng Cheng and other colleagues and friends for their help, discussion and companionship during experiments.

Finally, want to thanks my parents for their endless support and encouragement.

Abstract

Fresh water on our planet is locked in the ocean as seawater, which has to be desalinated for domestic, industrial, and agricultural use. Solar vapour generation using photothermal materials to efficiently convert solar energy into heat for water evaporation is an emerging technology for seawater desalination. It is promising to mitigate the worldwide water scarcity problem in a green and sustainable way. However, developing high-efficient continuous solar evaporators for practical desalination applications still remains challenging due to the salt accumulation issue on the photothermal materials, the difficulties in scaling up the evaporators due to the limitation of water supply driven by capillary force, and the insufficient understanding of multiphase transport and salt harvesting mechanisms inside porous structures. To address these limitations, this work aims to develop high-efficient solar evaporators that can achieve continuous solar vapour generation and salt harvesting concurrently from seawater, with improved salt harvesting mechanisms understanding. For this, the thesis primarily focuses on the following four parts: i) light-trapping photothermal material development, ii) evaporator structure improvement for continuous concurrent solar vapour generation and salt harvesting, iii) salt harvesting mechanism exploration, and iv) scale-up of the evaporator for large area applications.

In this work, a light-trapping nanofiber photothermal coating was proposed by copolymerization pyrrole with dopamine, which can be rapidly synthesized at room temperature by ultrasonic spray coating. The highest solar absorptance reached 97.73%. This nanoscale coating significantly improved solar absorption at different incident angles across the full solar spectrum, achieving the highest solar evaporation rate of 1.385 $kg \cdot m^{-2} \cdot h^{-1}$ under 1 sun. Then an umbrella evaporator was developed, which achieved high efficiencies of continuous fresh water production and salt harvesting concurrently via double-sided evaporation. The evaporation process was simulated to reveal that better mass transfer condition of the umbrella evaporator by double-sided evaporation greatly improves the evaporation rate, and the influence of environmental conditions, surface height and opening angles on the evaporation performance were also analysed by this simulation. The salt

nucleation, growth and falling mechanisms were also revealed. The salt mobility on the evaporation surface determines if the salt accumulates at the edge to fall, affected by water supply, salinity, and Mg^{2+} and Ca^{2+} contents. The salt on the edge grows from the front by wicking the water through its porous structures inside and falls due to the dissolution of its connecting parts. Salt creeping behaviours on a glass slide can indicate if the pre-treated seawater fits for salt harvesting. To address the water supply and distribution problems of the umbrella evaporator for large area application, a double-sided suspending evaporator with top water supply and surface water distribution systems was developed. Top central water supply gets away from the limitation of capillary force and allows larger area application. Its evaporation rate achieved 1.40 $kg \cdot m^{-2} \cdot h^{-1}$ with deionized water under 1 sun (95.7% energy efficiency), with a remarkable low surface average temperature (28.2 ºC). Then the salt distribution process on the surface was simulated to develop a novel floriform evaporation surface with a radial arterial water distributor to forcedly expose salts at the edge for harvesting and efficiently distribute the water on a larger evaporation surface.

This work shows great potential of the polypyrrole-dopamine nanofiber light-trapping coating as photothermal materials for continuous vapour generation, provides new ideas for the structure design of the evaporators that achieve solar vapour generation and salt harvesting concurrently, and allows us to better understand and control the salt harvesting process.

Keywords: solar energy, solar thermal conversion, salt harvesting, solar vapour generation, polypyrrole, umbrella evaporator, interfacial evaporator, desalination

Table of Contents

List of Tables

List of Figures

Chapter 1
Introduction

1.1 Research background

Nowadays, one in three people do not have access to safe drinking water (WHO report, 2019). By 2050, half of our population will be living in water-stressed areas [1]. Fresh water scarcity has always been a pervasive problem due to increasing domestic, industrial and agricultural demands and fresh water contamination [2]. Seawater desalination technology separating salt from seawater to produce fresh water could mitigate the water scarcity problem. Now widely used desalination technologies, e.g. reverse osmosis desalination, multi-stage distillation, and multiple-effect distillation, consume too much energy for either creating high pressure environment or vaporizing seawater. If using fossil fuels, this may also in turn cause energy shortage and environmental problems

Water evaporation can produce highly pure fresh water, but it also requires a large amount of energy to supply the large latent heat (2256 kJ/kg) of water vaporization [3, 4]. Solar energy is regarded as the most abundant, clean and renewable energy among all the available renewable energy sources [5]. By utilizing solar energy, solar vapour generation (SVG) is a promising green technology for seawater desalination and sewage treatment. SVG process efficiently converts solar irradiation into heat to evaporation water by photothermal materials, directly producing drinkable water, whose energy efficiency can reach above 90%.

1.2 Motivation

SVG technology is potentially able to solve the water scarcity problem worldwide in a green and sustainable way. However, there are still some limitations preventing its widespread application. First of all, developing a high-efficient, low-cost, and durable photothermal material with easy availability still remains challenging for real industrial applications. Meanwhile, the intrinsic solar absorption of a material determines the upper limit of the solar energy capture. Hence, in addition to material itself, designing a light-trapping surface structure with open pores and channels would break this limit

and further improve the solar absorption for better SVG performance by enabling multiple reflections inside the material. The most common method for creating pores and channels in the evaporation layer are based on using prepared porous or fibrous templates as substrate and then coat a solar absorbing layer on this substrate to obtain a light-trapping structure, which would complicate the fabrication process [6, 7].

In addition to the photothermal material, the study of the solar evaporator structure to improve the system energy efficiency is still insufficient. More importantly, when the solar evaporator is applied on real seawater, salt would accumulate on the photothermal material and gradually slow down the evaporation rate and finally stop the whole system. The salt accumulation problem greatly affects the continuous operation of the evaporation system. Salt accumulation on the evaporation surface greatly affects the continuous operation of the evaporation system.

Considering the industrial value of sea salts, harvesting fresh water and salts from seawater at the same time is the optimal strategy. However, the salt harvesting process study is lacking, and the salt nucleation, growth and falling mechanisms on a porous media remains poorly understood for salt harvesting process control.

Moreover, water transport of most current evaporators is heavily driven by capillary force, which cannot keep up a higher evaporation rate on a larger evaporation surface. The water supply driven by capillary force greatly limits the scale-up of the evaporators for large area applications.

1.3 Aim and objectives

To address the limitations above, this work aims to develop high-efficient solar evaporators that concurrently achieves continuous vapour generation and salt harvesting from seawater, with improved salt harvesting mechanism understanding.

The key objectives of this work are as follows:

- Developing a high-efficient light-trapping photothermal material with open pores and channels to capture more solar energy into the evaporation system by enabling multiple reflectance inside the pores and channels.
- Improving solar evaporator structures to provide better vapour diffusion conditions by both experiments and evaporation simulations, and solve the salt accumulation problems to achieve continuous solar vapour generation and salt harvesting from seawater.
- Improving the understanding of the salt harvesting mechanisms on a porous media, including initial salt precipitation, salt accumulation, and salt growth and falling.
- Developing scale-up methods for the continuous solar evaporator that achieves concurrent vapour generation and salt harvesting for large area applications by both experiments and salt distribution simulations.

Throughout the work, it first demonstrates a facile polypyrrole-dopamine nanofiber light-trapping coating for efficient SVG by ultrasonic spray coating. Then, this work presents a novel umbrella evaporator that achieves high efficiencies of fresh water production and salt harvesting concurrently via double-sided evaporation, and shows its structural advantages by both experiments and simulations. Benefiting from the rational design, salt will fall down automatically from the edge by gravity. This work also explores the salt accumulation and falling behaviours from macroscale to microscale, and notably proposes the salt nucleation, growth, and falling mechanisms. To address the water supply and distribution problems of the umbrella evaporator for large area application, a double-sided suspending evaporator was further developed with top water supply and radial arterial surface water distribution systems for concurrent solar evaporation and salt harvesting. Top central water supply gets away from the limitation of capillary force and allows larger area application.

1.4 Thesis outline

This thesis is structured into eight chapters: an introduction chapter (Chapter 1), a literature review chapter (Chapter 2), a photothermal material chapter (Chapter 3), two solar evaporator structure chapters (Chapter 4-5), a salt harvesting from real seawater chapter (Chapter 6), a scale-up of the evaporator chapter (Chapter 7), and a conclusion chapter (Chapter 8), as shown in Figure 1.1. Chapter 3 demonstrates a polypyrrole-dopamine nanofiber light-trapping photothermal material. This chapter introduces the coating method, and characterizes the surface physical microstructures and chemical structures, and characterization of its solar trapping performance. Base on this light-trapping material, Chapter 3 presents a high efficient interfacial solar evaporator with salt back diffusion pathways to achieve continuous operation. Chapter 5 shows the advantages of an umbrella evaporator in evaporation performance by comparison with the interfacial evaporator, and reveals the reasons. Meanwhile, based on the evaporation simulations, key factors affecting the energy efficiency are discussed in this chapter. Benefiting from the rational design of the umbrella evaporator, salt can be harvested from the evaporation surface edge, and Chapter 6 discusses the factors affecting the salt falling from the umbrella evaporator, and proposes the salt harvesting mechanism. Applications on real seawater and simulated seawater are different, how different components in real seawater affect the salt harvesting is studied, and finally a facile test for if the saline water fits for salt harvesting is proposed in this chapter. Chapter 7 shows a double-sided suspending evaporator with top water supply and radial arterial surface water distribution systems for large-area high-efficient concurrent solar evaporation and salt harvesting. Through both simulations and experiments, a radial arterial water distribution system and a floriform evaporation surface are designed to efficiently distribute the water on a larger evaporation surface and accumulate the salt at the edge. Chapter 8 summarizes the main conclusions and indicates future works.

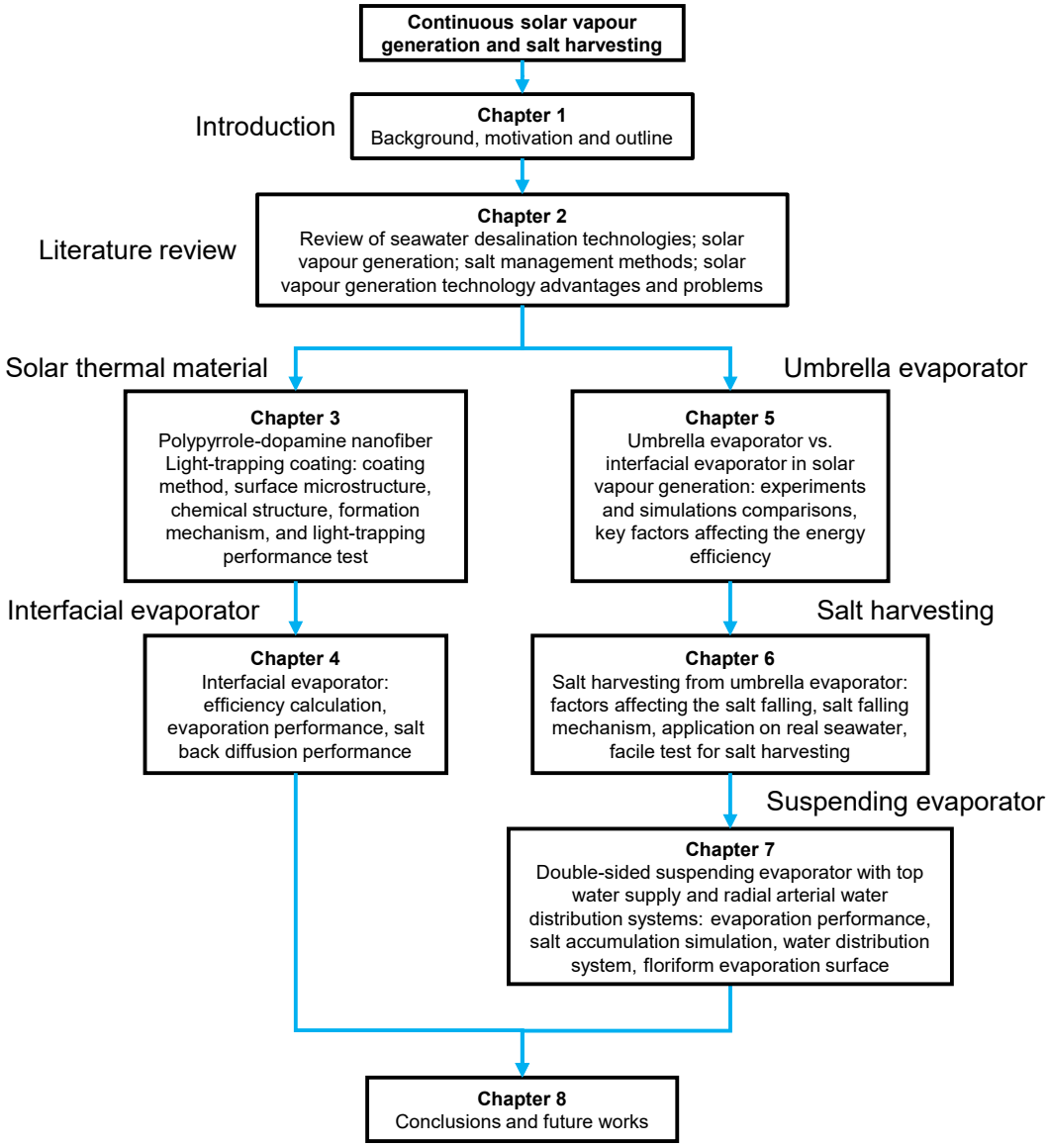

Figure 1.1 Structure of this thesis.

Chapter 2

Literature review

2.1 Seawater desalination

Seawater desalination technology generally falls into two categories: thermal-based desalination and membrane-based desalination [8]. Thermal-based desalination utilizes thermal energy to evaporate seawater to obtain fresh water, with multi-stage flash distillation (MSF) and multiple-effect distillation (MED) being the most common thermal-based desalination processes. Membrane-based desalination utilises a semi-permeable membrane through which salt cannot pass to separate the fresh water. Reverse osmosis (RO) and forward osmosis (FO) desalination processes are the most common membrane-based desalination processes. Overall, the total seawater desalination capacity is about 86.5 million m^3/day, therein RO process is dominating the desalination market in the world (65%), followed by MSF (21%) and MED (7%) as shown in Figure 2.1.

Recently, interests in solar driven desalination are increasing, as it harvests renewable solar energy to generate water vapour to obtain fresh water, which is promising to solve the water crisis in a green way without consuming fossil fuels.

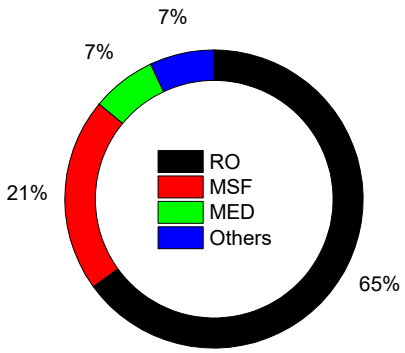

Figure 2.1 Desalination capacity of membrane and thermal process in the world (Total: 86.5 million m^3/day) [9].

2.1.1 Multi-stage flash distillation (MSF)

MSF is a typical thermal-based desalination process. Thermal energy is used to evaporate seawater in multiple stages, in which the temperature and pressure are successively lower caused by hot brine evaporation and vapour condensation (Figure 2.2) [10]. The feed seawater exchanges heat with water vapour in each stage and is heated by steam to reach the required top brine temperature (~100 ºC). The heated brine flashes through stages to generate water vapour and is finally discharged [11]. Due to its suitability to scale up, large handling capacity, not requiring pre-treatment, and easy maintenance, MSF is taking the second share in the desalination market after the RO process.

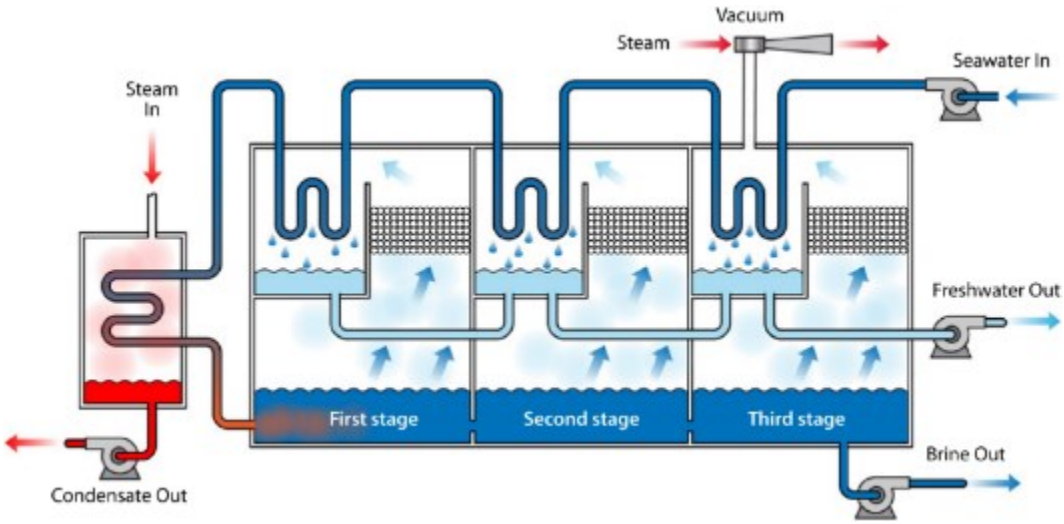

Figure 2.2 MSF system schematic [12].

2.1.2 Multiple-effect distillation (MED)

Similarly, MED process also heats the seawater to generate fresh water vapour which is to be condensed as fresh water (Figure 2.3). The preheated seawater sprays from the top at each stage. Steam heats the tube bundles in the first stage to partly evaporate the seawater. The water vapour goes into the tube bundles in the next stage to make the seawater evaporate. Apart from the first stage, the next stage heat source comes from the latent heat of vapour condensation from the previous stage. The condensed water goes out as the fresh water product, and the unevaporated seawater is discharged as waste brine. The temperature and pressure decrease gradually from each stage. The hottest temperature in the first stage is typically below 70 ºC [13].

As MED process works at a lower temperature than MSF (70 ºC vs. 100 ºC), MED process consumes less heat energy and lowers the production cost. In addition, due to lower working temperature, it is more easier to utilize waste heat or low pressure steam, and combine with solar energy [14]. Therefore, recent developments in the MED process help this technology to be gaining the market share.

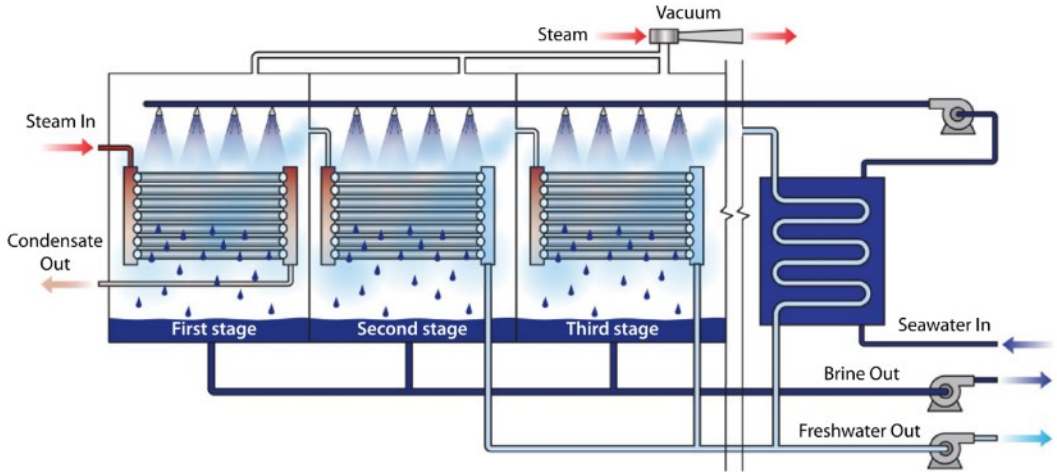

Figure 2.3 MED system schematic [12].

2.1.3 Reverse osmosis desalination (RO)

Traditional thermal-based water distillation for desalination requires lots of fossil fuels to supply the high enthalpy of water vaporization (2256 kJ/kg), which speeds up greenhouse gases emission. This technology solves the water scarcity problem at the expense of causing environmental problems and energy shortage. Reversed osmosis desalination as a typical membrane-based desalination technology, separates the water and salts by a semi-permeable membrane, which is driven by pressure. Since 1980s, reverse osmosis desalination develops rapidly as it avoids the energy consumption of the enthalpy of water vaporization based on thermal desalination [8]. As shown in Figure 2.4, a typical RO system consists of four subsystems: (i) a pre-treatment section to reduce the scaling and fouling; (ii) a high pressure pump to push the water through the membrane; (iii) a membrane to separate the fresh water from the seawater; (iv) a post-treatment section to make the water quality up to stand [15]. Nowadays, RO process is the most commonly used desalination method in the world.

Although RO process forbids the energy consumption of the water phase change, RO process requires a high pressure (typically around 6 MPa), to overcome the osmotic pressure of seawater, which still costs much electricity energy and requires a high mechanical strength of the membrane and the supporting systems [8]. In addition, the concentrated seawater will be discharged back to the sea, which will harm the ecosystem around [16].

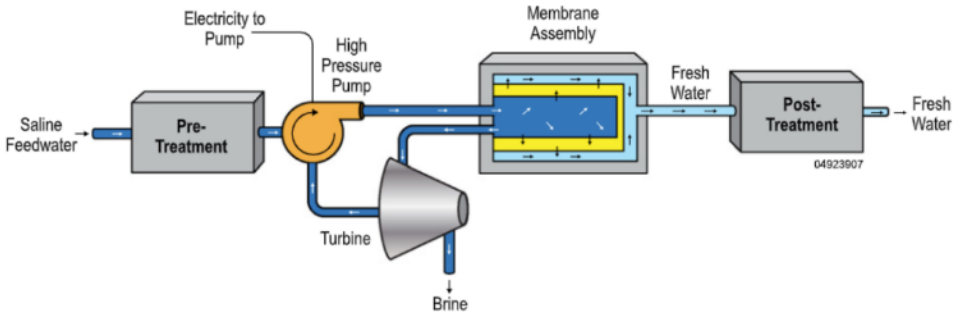

Figure 2.4 RO system schematic [12].

2.1.4 Forward osmosis desalination (FO)

FO is also a membrane-based separation process driven by osmotic pressure gradient to draw water across the semi-permeable membrane from feed solution to draw solution (Figure 2.5). As this process is driven by osmotic pressure, FO has many advantages such as low energy intensity, less membrane fouling, very low hydraulic pressure, low membrane and equipment requirement, and high water recovery [17-23]. In the past decade, forward osmosis (FO) technology has been extensively studied for seawater desalination, wastewater treatment, food processing and power generation [20, 23].

The main problem for FO desalination is how to extract water from draw solution and make it regenerate to keep the osmosis pressure gradient. The draw solution regeneration process usually requires high electrical energy-consuming processes, which restricts the development of this technique [24].

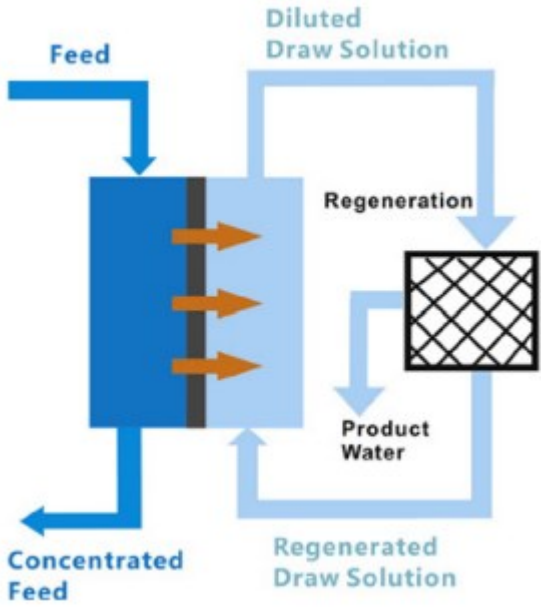

Figure 2.5 FO system schematic [25].

2.1.5 Solar energy in desalination

With the seawater desalination market expansion, energy crisis intensification, and environmental problems aggravation, renewable solar energy is attracting more and more attentions to power the desalination processes.

i) Solar energy in MSF and MED: MSF and MED are both thermal-based desalination processes. Steam powered by solar parabolic through thermal collectors can be utilized as heat source [26]. Typically, a thermal storage system should be connected to the desalination system to smooth the solar energy supply variation and make it possible to continuously produce fresh water during nights or less sunny periods.

ii) Solar energy in RO: Solar photovoltaic electricity can drive the pumps of the RO system [27]. Battery banks are also needed to store electricity energy to allow night running. Investment cost of the solar photovoltaic RO system is higher than conventional RO system. The overall economic gains vary in different areas according to the solar irradiation intensity.

iii) Solar energy in FO: Although osmotic pressure drives the water to pass through the semi-permeable membrane. With water collecting in the draw solution, the osmotic pressure would decrease due to its concentration reduction. Therefore, the draw solution needs to be regenerated, which

consumes much energy [28, 29]. Solar energy can be used to separate fresh water from the draw solution to make it regenerated [30].

iv) Solar vapour generation: Recently, direct solar vapour generation technology is gaining more and more attention, which directly converts solar energy into heat to evaporate seawater. The energy conversion efficiency of this process can achieve over 90%, which is very attractive [31]. This work focuses on this technology and the details will be reviewed in the following section.

2.2 Solar vapour generation

Clean and fresh water shortage causes many problems worldwide: 1.2 billion people lack safe drinking water, 2.6 billion have little or no sanitation, and every year millions die from preventable illnesses relating to unsafe water or human excreta [2]. However 96.5% of the total water on the Earth is in the oceans and exists as saline water with a salinity of 3.5 wt% [32]. Therefore, the technologies for desalination and sewage water treatment are heavily in need. Among them, solar vapour generation is receiving more and more attention because of its producing fresh water directly with nearly no other forms of energy consumption except free sunlight. In the nature, the way humans obtain fresh water also mainly relays on solar evaporation caused by the transpiration of plants or sunlight heating seawater, in which process the water vapour produced condenses as rains and snows to feed the earth fresh water supply. Solar vapour generation technology is to supplement this vapour generation process to supply fresh water in certain areas and it can also be utilized to treat waste water.

2.2.1 Solar energy utilization

Solar energy is regarded as the most abundant energy among all the available renewable energy sources [5]. The Sun emits energy at a rate of 3.8×10^{23} kW, of which the energy that can be captured by the Earth is estimated to be 1.8×10^{14} kW [33]. Nearly 40% of the total energy is reflected into space, leaving only 60% of them reaching the surface of the Earth [34]. Even so, more energy from solar irradiation strikes the Earth per hour than all the energy consumption by humans per year [35]. Approximately, if 0.1% of the

solar energy that reaches the Earth can be utilized at an efficiency of 10%, it will generate 4 times of the world's total generating capacity of about 3000 GW [33]. Besides, solar energy is almost everywhere, which makes it to be ubiquitous renewable energy against other renewable energy forms, e.g. tidal and wind energy.

Nowadays, 80% of the energy humans used comes from fossil fuels, and world demand for fossil fuels is expected to exceed annual production probably in the next two decades [33]. Furthermore, combustion of fossil fuels causes a serious of global environment problems by releasing carbon dioxide, nitrogen oxide, sulphur dioxide, inhalable particles, etc. With increasing demand for energy and decreasing storage of conventional fossil fuels, abundant and clean solar energy peaks out among all other energy sources and is attracting more and more attention.

The utilization of solar energy comes mainly in two categories: photovoltaic conversion and photothermal conversion [36]. Photovoltaic (PV) conversion is to turn sunlight into electric power by solar cells using semiconducting materials that exhibit the photovoltaic effect. Invented 50 years ago, single-crystalline Si solar cell remains the basis of the current PV industry due to its abundant reserves and high reliability and high efficiency [37]. Currently photovoltaic technology are progressing with the intense R&D efforts and helping to improve the conversion efficiency, including water-based cells (traditional crystalline silicon or gallium arsenide), commercial thin-film cells (cadmium telluride, amorphous silicon, copper indium gallium diselenide) and new thin-film technologies (perovskites, organic materials, quantum dots) [38-40]. The improvements in research-cell efficiencies achieved over the past 40 years are shown in Figure 2.6, depicting all verified records for PV conversion technologies, collected from solar companies, universities and national laboratories. It can be seen that so far the energy efficiency for photovoltaic conversation is usually below 50%.

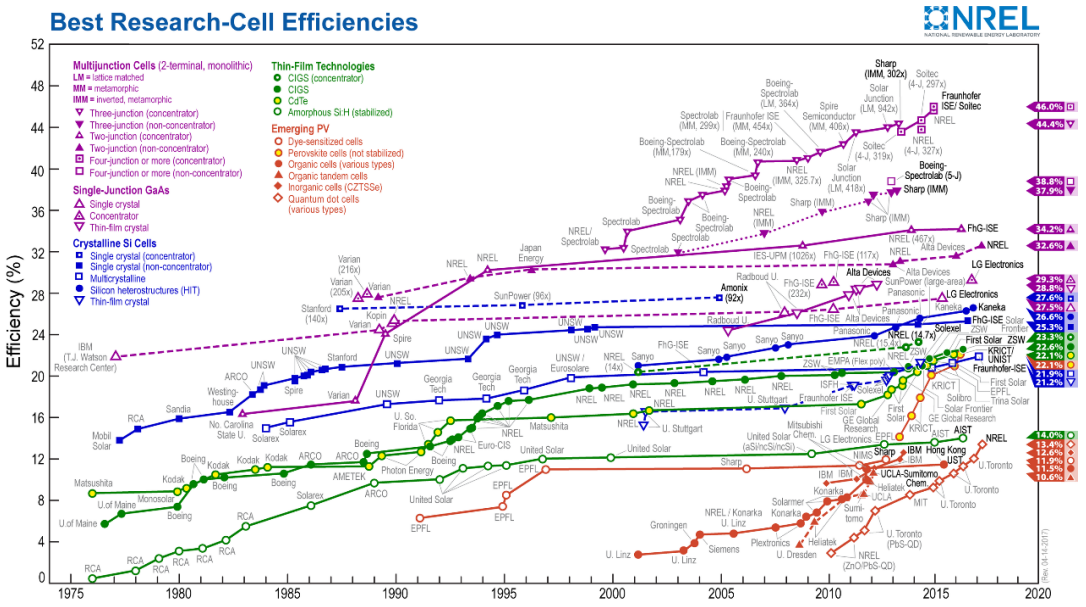

Figure 2.6 A timeline for reported best research-cell efficiencies from 1975 to 2017, showing the most recent 46% efficiency in multijunction cell [41].

By contrast, the solar thermal conversion efficiency is much higher (usually above 70%, some are even over 90%), making it more suitable to realize extensive application, such as solar vapour generation, solar desalination and solar sterilization et al [30, 42, 43]. Solar thermal conversion technology is to harness solar irradiation energy to generate thermal energy for use in industry, in residential or commercial sectors. Solar thermal energy has been utilized by humans for a long time, such as solar water heaters, solar cookers and solar driers [44-49].

In recent years, concentrated solar power (CSP) systems are being widely built [50]. CSP uses mirrors or lenses to concentrate a large area sunlight onto a small area to collect high-quality heat, which drives a heat engine to generate electricity, shown in Figure 2.7 [51-53].

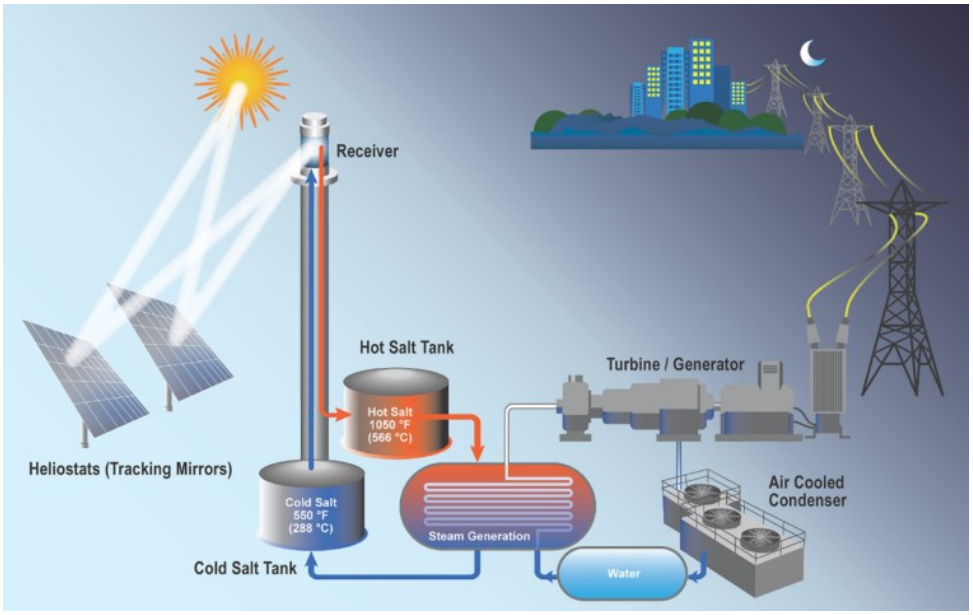

Figure 2.7 A molten salt power tower CSP system with a Rankine power cycle [51].

Solar vapour generation can be widely used in the fields of domestic water heating, sewage treatment, desalination and distillation [54-56]. This promising technology attracts lots of researchers to search and develop suitable materials, design reasonable structures for solar evaporators, optimize heat transfer environment and finally improve the energy conversion efficiency. SVG utilizes photothermal materials to convert solar energy to thermal energy to evaporate water. The photothermal material, solar heating forms, and solar evaporator structure all affect the overall energy conversion efficiency.

2.2.2 Photothermal materials

The ideal materials for solar vapour generation should meet the following properties: (1) they should have a wide sunlight absorption bandwidth covering the full solar spectrum from 250 nm to 2500 nm; (2) they should have excellent solar-to-heat conversion efficiency with less thermal radiation to the environment; (3) they should be easy to get and have good high-temperature durability [57, 58]. It has been proved that the wettability of the top absorber surface has little influence on the evaporation rate which mainly depends on the wettability of the bottom supporting layer [59].

The materials for solar vapour generation can be mainly classified into three categories: plasmon-based materials, carbon-based materials and polymers. **Plasmon-based materials** utilize the surface plasmon resonance effect to generate thermal energy under resonant illumination and have a narrow band of sunlight resonance peak. Generally, plasmon-based materials refer to metal, metal oxide or metal nitride nanoparticles [58]. Au, Cu, Ag and Al are the most widely studied nanoparticles for solar steam generation because of their stability [6, 60-62]. Some alloys were also developed for solar steam generation such as Al-Cu and Ag-Au [63]. For metal oxides, Ti_2O_3, Fe_3O_4, Fe_2O_3 and CuO were also experimentally tested [57, 64-66]. Metal nitrides with broad light absorption bandwidth have also been explored for solar-thermal conversion, such as MoN and TiN [67].

Unlike plasmonic materials, **carbon-based materials** have higher sunlight absorption under the whole solar spectrum with excellent stability, and they are low-cost with easy availability, which makes them technologically important in solar water evaporation [68-70]. It has been experimentally proved that the crystallinity of carbon (or degree of graphitization) and BET surface areas affect little on the solar thermal conversion efficiency [71]. Almost all the common carbon materials have been explored in different absorber structures, for example, graphite, expanded graphite, carbon black, carbon nanotube, carbon nanofiber, graphene, graphene oxide, reduced graphene oxide [30, 42, 69, 70, 72-76]. Among them, carbon nanotube (CNT) is one of the blackest materials (also known as super black material) in the world with extremely high solar irradiation absorbance [73]. Generally, pristine carbon material is hydrophobic, however its wettability can be tuned by oxidation process introducing oxygen-containing hydrophilic groups.

It has been reported that, some conjugated **polymers** exhibited broadband light absorption spectra, such as, polypyrrole, polydopamine, polyaniline and other conjugated polymers [77-79]. Compared with plasmon-based or carbon-based materials, polymers have many advantages. They are inexpensive and suitable for mass production [77]. Among them, polypyrrole (PPy) is outstanding with black colour and wide adsorption and can be easily coated or deposited on all kinds of substrates, including hydrophilic, hydrophobic and even curved structures [79]. PPy can be obtained by electrochemical

polymerization and oxidation polymerization. Electrochemical polymerization requires the substrate to be conductive. Oxidation polymerization is facile, using ferric trichloride ($FeCl_3$) or ammonium persulfate (APS) as oxidizing agent [80, 81]. Besides, polypyrrole is chemically stable which is insoluble in water and most organic solvents and its melting point is higher than 300°C. Huang et al coated polypyrrole on a polypropylene mesh by a dip-coating method [79]. The polypropylene mesh was dipped into a pyrrole/water solution with $FeCl_3$ as oxidizing agent for 8 h, reaching a thickness of 300 nm of PPy deposition. The contact angle of the PPy coating is 60° on the flat surface indicating a hydrophilic surface and it was further tuned to hydrophobic to make it float on the surface. The solar vapour generation efficiency was 72% under 1 sun. Hao et al coated PPy on a cotton fabric and introduced a polystyrene foam as the thermal insulator layer [82]. The cotton before and after PPy coating is shown in Figure 2.8. The cotton fabric wicked the water and PPy converted light into heat. The efficiency for this structure achieved 82.4% under one sun.

Figure 2.8 Pristine cotton and PPy/cotton [82].

Polydopamine (PDA) is the main composition of melanin and adhesive protein of mussel [78]. It is black with strong adhesion and can be obtained by self-polymerization of dopamine under alkaline conditions [83]. Wu et al coated PDA on a piece of treated pine wood twice (pH = 8.5) and achieved the efficiency of 87% under one sun and 135% under 3.5 sun, as shown in Figure 2.9 [78]. The catechol structure itself (in PDA) is responsible for the excellent adhesion, which can be used to improve adhesive strength by adopting catechol functionalities [84].

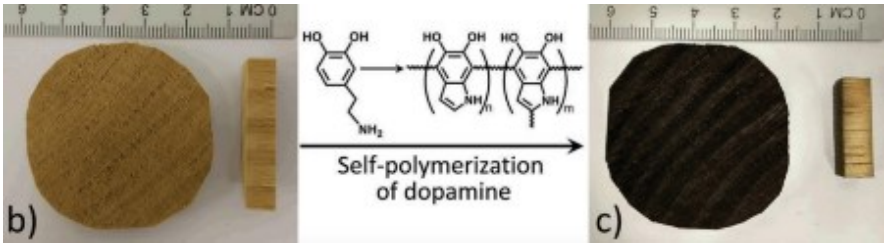

Figure 2.9 Nature pine wood and PDA-coated wood [78].

2.2.3 Solar heating forms

There are mainly three forms of solar heating: bottom heating, bulk heating and interfacial heating, as shown in Figure 2.10.

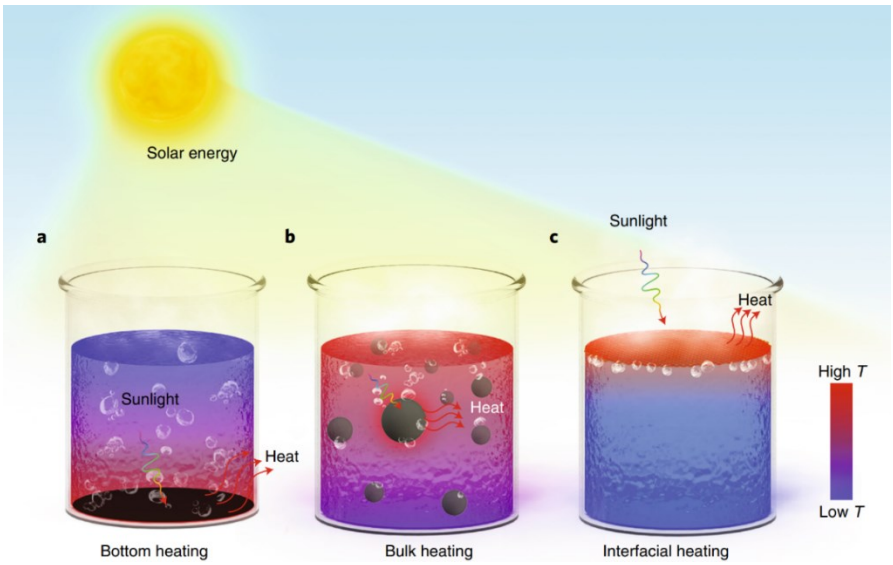

Figure 2.10 Three forms of solar heating steam evaporation [58].

Bottom heating is a traditional solar heating method. Solar absorbers are placed at the bottom of water to convert solar irradiation into heat to heat up the whole water from bottom to generate steam, which inevitably causes heat loss and pulls down the evaporation efficiency of 30~45% [85].

Bulk heating is heating the bulk fluid in a solar trough or a solar tower system, which is usually under concentrated solar irradiation by optical lens [4]. Nanoparticles dispersed directly in the fluid usually act as solar absorbers and their good distribution can reduce the temperature difference between the absorbers and the fluid [86]. The advantage of bulk heating is that the whole volume of fluid can absorb solar irradiation not only from bottom or surface but also from side walls, which is an excellent property for concentrated solar

power (CSP) systems. While, the robust dispersion of nanofluids is still a challenge in long-term operation under concentrated sunlight [87, 88].

Nanoparticles with surface plasmon resonance properties can efficiently absorb solar irradiation and generate heat around when excited by resonance [89]. This heat generation process can be widely used in many fields, such as, photothermal cancer therapy, laser-induced drug release and photothermal imaging [90-92]. For bulk heating, the nanoparticles with surface plasmonic effect would rapidly increase the particle temperature and generate steam. It is hypothesized that the rapid heating is due to the nanobubbles round the nanoparticles, which raise the particles to the surface and release the steam produced [93, 94]. However, theoretical calculation of the kinetics of nanobubbles formulation shows that about 1×10^{10} sun is required to form nanobubbles, which is unlikely to occur under normal solar irradiation [95]. It is widely believed that, nanoparticles create superheated zone because of high non-uninform of temperature and radiation distribution along the incident light, leaving the bulk fluid subcooled at initial stage [4]. Then they will reach equilibrium with the surrounding fluid, and steam generation is caused by the temperature increase of the bulk fluid [96].

Metal or metallic oxide nanoparticles, due to the resonant characteristics of surface plasmon excitations, inherently have a narrow absorption bandwidth of the wavelength and different materials peak at different wavelength [97]. Therefore, carbon-based nanoparticles with a broad absorption bandwidth attract more interests, which can utilize the full spectrum of sunlight [96]. Figure 2.11 shows the absorbance spectrum of Au and carbon black nanoparticles, indicating that carbon-based materials have a much higher absorbance over the full wavelength [98]. Besides, the linear relationship between fluid concentration and absorbance conforms to Beer's law [98]. Therefore, increasing solution concentration will improve the light absorbance. While nanoparticles with higher concentration trend to aggregate with ease leading to an unstable fluid, which restrains further improvements of absorbance.

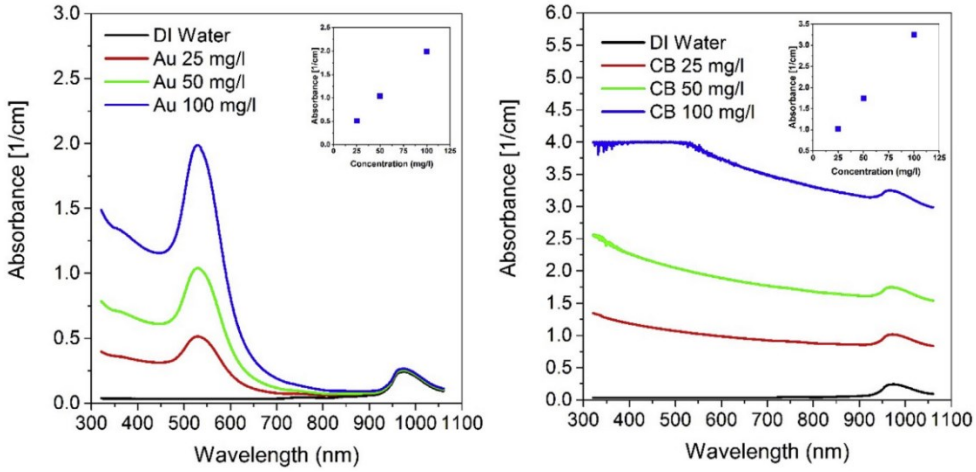

Figure 2.11 Absorbance spectrum of Au and Carbon Black with different concentrations [98].

The solar thermal conversion efficiency of bulk heating achieved moderate improvement, mainly in the range of 60~80% in high solar concentration. Typically, Jin et al used gold nanoparticles to achieve the efficiency of 80.3% with the concentration of 12.75 ppm under 220 sun [4], and under 10 sun the efficiency of 60.3% was achieved using Fe_3O_4@CNT nanoparticles of 0.5 g/L by Shi et al [64].

Interfacial heating is a newly developed heating method for vapour generation, as evaporation is an interfacial mass transfer process between air and water. Solar absorbers float on the water surface and generate heat to evaporate the water on the surface. To avoid heat loss to the bulk fluid, multi-layers structures are designed to localize the heat on the surface [42, 99]. Heat localized on the surface is mainly used to generate steam rather than heating up the bulk water beneath. Generally, this evaporation system should consist of three key components: (1) a top broadband sunlight absorber to convert solar irradiation to heat; (2) a thermal insulator to minimize heat transfer from the surface to the bulk water and support the system float on the surface; (3) a water transport system to pump water to the top sunlight absorber layer [58, 75]. A rational design for the interfacial heating structure is also helpful in trapping the irradiation. For example, a rough surface with microstructures is usually desirable for reducing diffuse reflection resulting higher sunlight harvest [100].

In 2014, Ghasemi [42] and Wang [101] et al separately proposed this interfacial heating method for solar steam generation, which are one of the first to introduce the interfacial heating concept [58]. In Ghasemi's work, hydrophilic and porous exfoliated graphite acted as solar absorber, and hydrophilic and porous carbon foam was used to insulate heat transfer to the bulk fluid and float the structure, achieving the thermal efficiency of 64% under 1 sun (1 $kW \cdot m^{-2}$) and 85% under 10 sun, as shown in Figure 2.12.

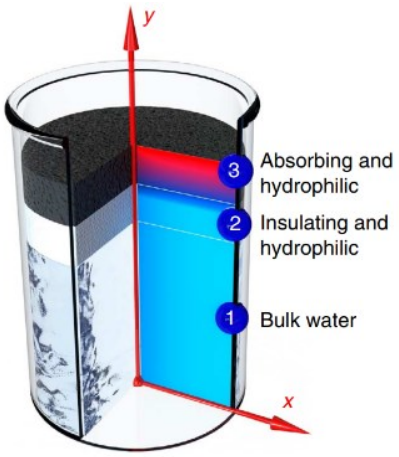

Figure 2.12 Schematics diagram for interfacial heating with heat localization [42].

The hydrophilic thermal insulator will be filled with water, whose thermal conductivity (0.6 $Wm^{-1} \cdot K^{-1}$ at 20°C) is much higher than the thermal insulation materials [102]. Therefore, high content of water would increase heat conductivity and reduce the system energy efficiency. To avoid this, Li et al proposed a 2D water path structure, as shown in Figure 2.13 [103]. Graphene oxide is used to absorb sunlight and polystyrene foam acts the thermal insulator between the absorber and water. Water is pumped to the top absorber by a 2D water path made of a layer of cellulose that wrapped over the polystyrene foam. This structure improved the thermal efficiency to 80% under one sun. Similarly, Shi et al directly coated polystyrene foam with porous reduced graphene oxide which is darker and has more sunlight absorbance than graphene oxide itself [75]. This structure was used for solar-driven interfacial steam generation and achieved the efficiency of 83% under one sun. Zhao et al synthesized a hierarchically nanostructured hydrogel with internal gaps, micron channels and molecular meshes inside, which helps

reduce vaporization enthalpy [31]. Polypyrrole particles penetrate the polyvinyl alcohol matrix to absorb sunlight and the resulting gel was treated by freezing-thawing process for 10 times to create the channels inside. The thermal efficiency reached 94% under 1 sun irradiation.

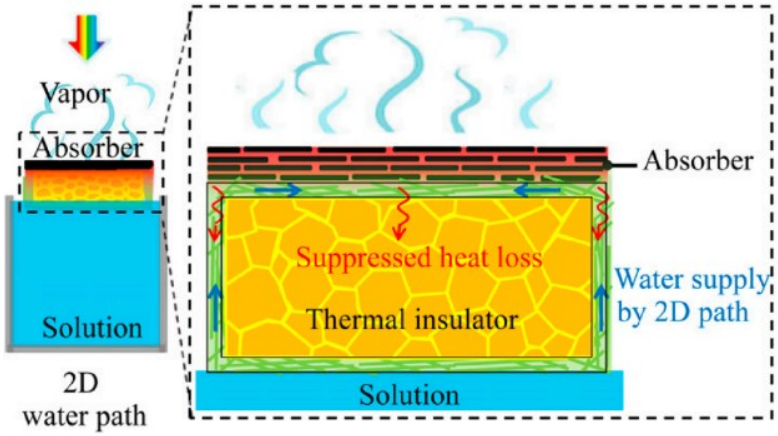

Figure 2.13 Schematics of 2D water supply for vapour generation [103].

Interfacial heating is most promising for natural sunlight steam generation without optical concentration because of its high thermal efficiency, which is usually from 80% to 90% and some are even higher than 90% [57, 69]. Even under one sun without optical concentration, 100°C steam can also be generated by thermal concentration structure, which collects heat rather than sunlight into a small evaporation slot to produce high temperature steam [99].

2.2.4 Solar evaporator structures

The structure of a solar evaporator also affects the overall evaporation performance by improving the vapour diffusion environment, reducing heat loss to the bulk water or environment. Many solar evaporator structures have been developed and each kind of evaporator has its own characteristics in improving the evaporation efficiency. The most classic evaporator is a sandwich structure. They usually consist of three key components: solar absorbing layer, water wicking path and thermal barrier. Wang et al deposited Ti_2O_3 nanoparticles on a cellulose membrane in vacuum, as shown in Figure 2.14 [57]. Ti_2O_3 nanoparticles absorb solar energy and convert it into heat, and the cellulose substrate pumps the water to the top and insulates the upper heat to the bulk fluid. The porous silica substrate wicks the water and acts as thermal barrier, and CNT membrane absorbs sunlight to generate heat.

Huang et al synthesized C-TiO_2 solar absorber and placed it on a polyvinyl alcohol (PVA) fibre material which acts as the steam generation layer, and the whole structure was floated by a foam (also as heat insulator), as shown in Figure 2.15 [104]. The C-TiO_2 layer converts sunlight to heat and heats the PVA fibre below, and the PVA fibre will both wick the water to the surface and make evaporation.

Figure 2.14 Schematic diagram of the bilayer solar steam generator [57].

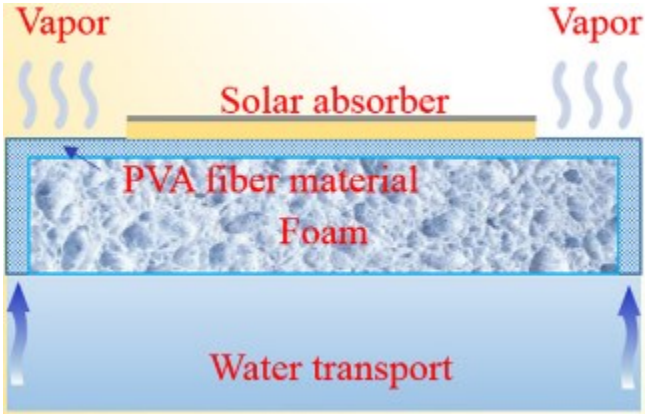

Figure 2.15 Schematic illustration of the solar evaporator structure [104].

Some solar absorber is just a sheet floating on the surface without thermal barrier, whose efficiency is relatively lower due to heat loss to the bulk water. Liu et al cured carbon black on a gauze by poly (dimethylsiloxane) (PDMS) and obtained a superhydrophobic membrane, as shown in Figure 2.16 [70]. Because of its hydrophobicity, the membrane itself can float on the water surface and has self-cleaning ability. Lou et al dropped graphene oxide solution onto airlaid paper and reduced it with ethanol to get a reduce graphene oxide layer [105]. To add photocatalytic degradation capacity, they

subsequently dropped TiO_2 nanoparticle solution on the airlaid paper and made it dry. This is an all-in-one water treatment structure which can both evaporate water and degrade organics. Chen et al carbonized facial tissue in Ar and used it as a self-floating solar membrane evaporator [106].

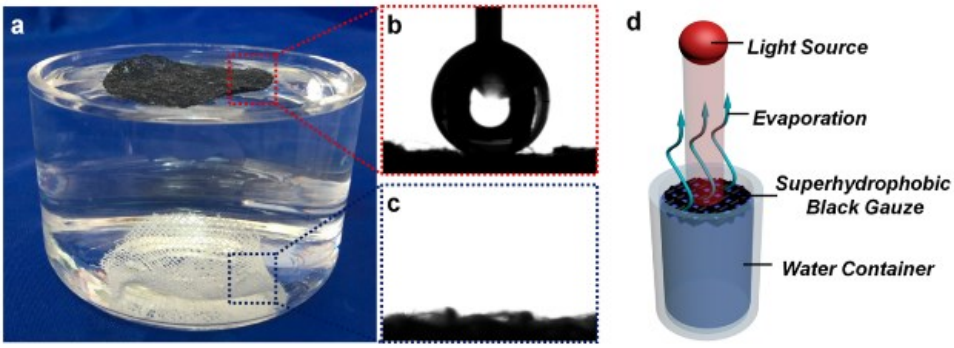

Figure 2.16 The as-prepared gauze and surface evaporation process [70].

Floating sheet is a 2D structure, thus both heat loss to the bulk water and diffuse reflection of the sheet will affect the efficiency. Therefore, 3D membrane with microscopic porous structure is a solution. Zhou et al deposited aluminium nanoparticles on an anodic aluminium oxidation membrane (AAM) (effective thickness ~85 nm), as shown in Figure 2.17 [6]. Aluminium is the only raw source material for this 3D structure. By physical vapour deposition, Al nanoparticles were deposited not only on the surface but also in the vertical channels in the membrane, which efficiently prevents sunlight diffuse reflection and achieves the efficiency of ~57% under 1 sun.

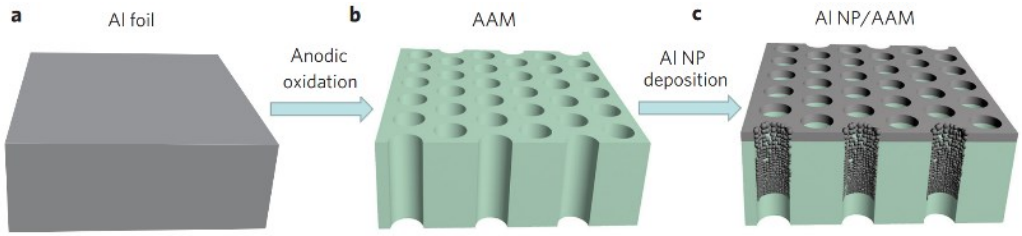

Figure 2.17 Fabrication of the Al nanoparticle-based absorber [6].

Multilayer structure is widely adapted due to its higher efficiency, while a single solar absorber sheet without thermal barrier usually bears lower efficiency. However, a monolithic solar absorber can realize solar absorbing and water wicking and heat insulating in a single unit. Mu et al carbonized conjugated microporous polymer nanotubes to get a monolithic carbon aerogel, which

contained hierarchically nanoporous network structure, as shown in Figure 2.18 [107]. Then it was treated by ammonium peroxydisulfate/sulphuric acid to realize superhydrophilic wettability. For this solar evaporator, the nanoporous structure itself plays the role of thermal barrier, and the conversion efficiency reached 86.8% under 1 sun. Similarly, Lin et al carbonized porous melamine foams through a one-step calcination process in nitrogen to get an integrative solar absorber for steam generation, achieving the efficiency of 87.3% [56].

Figure 2.18 Images of conjugated microporous polymers before and after carbonization [107].

In order to reduce heat loss to the fluid, reducing contacting area with water is another feasible way. Mushroom structure with 1D path water supply efficiently hinders heat loss to the bulk water through the wicking structure. Xu et al carbonized mushrooms and used it to harvest solar energy for steam generation, as shown in Figure 2.19 [108]. The carbonized mushroom was inserted through a polystyrene foam to make the stripe contacting the water below for water supply to the pileus. The mushroom contained porous structures inside and shrank 30% after carbonization. This carbonized mushroom achieved the efficiency of 78% under 1 sun. Liu et al were also inspired by water transportation plants and designed a 1D capillary-driven pump for solar water evaporation, which is essentially a flat-top mushroom structure [109]. This solar evaporator achieved the efficiency of 73% under 1 sun.

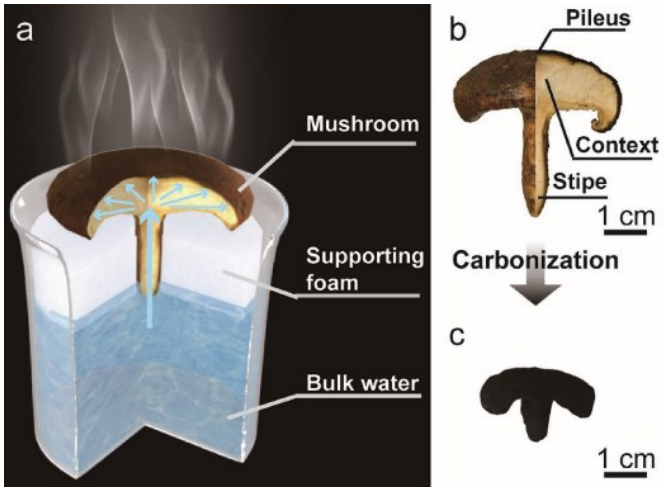

Figure 2.19 Schematic of a mushroom-based solar steam generator [108].

Mushroom structure will reflect light to the environment due to its round head facing outside. Wang et al reversed the cones to trap the incident light, making the light reflect inside the cones multiple times (Figure 2.20) [100]. By chemical vapour deposition polymerization, polypyrrole was coated on a hydrophilic polyvinylidene fluoride (PVDF) membrane that has interconnected porous structure to wick water and capture light. Then the cone was inserted into a polystyrene foam, leaving the tip contacting water. Both the inside and outside surfaces can evaporate water for this structure. After optimization, the solar conversion efficiency reached 93.8% under 1 sun.

Figure 2.20 Schematic illustration for the solar thermal cone preparation [100].

Floating spheres are a simple structure for solar evaporation, which are easy to be applied on the water surface. Furthermore, they are easy to carry and scale up for real application. Zhou et al fabricated hollow carbon spheres for

solar evaporation by carbonizing hollow polymer spheres (~1.2 mm in diameter) , as shown in Figure 2.21 [110]. The polymer spheres were obtained by a phase-inversion process. Organic drops with blowing agent ($(NH_4)_2CO_3$) inside were dropped in hot water, then the blowing agent decomposed and released gas to form hollow polymer spheres. To enhance mechanical properties, carbon nanotubes were added, which also help to make the colour deepened to dark. Similarly, floating hybrid magnetic particles (Fe_3O_4/C) particles (500 nm in diameter) were synthesized for light absorbing [111]. They can float on the water due to their hydrophobicity and low density. Because of magnetism, these particles can be recycled by a magnet.

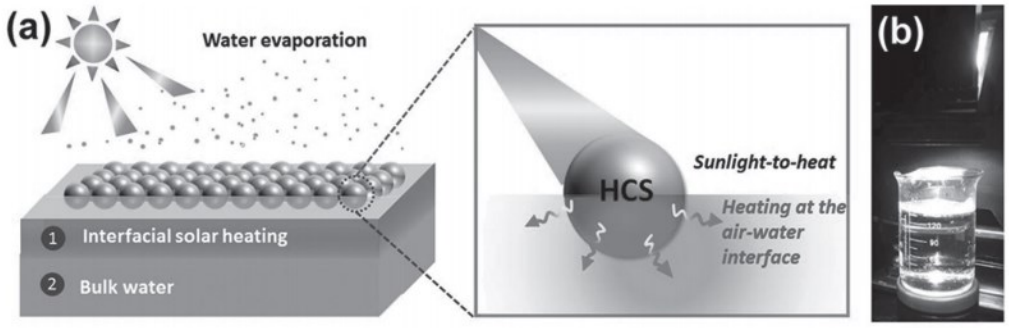

Figure 2.21 Schematic illustration for water evaporation by floating hollow carbon spheres (HCS) [110].

Water evaporation is a natural process even in the absence of solar irradiation, which draws the environmental energy around. The combination of natural evaporation and solar vapour generation will greatly improve the evaporation rate, even exceed the upper limit of the efficiency based on classical calculation method. Li et al designed a cylindrical vapour generator (10 cm in height), as shown in Figure 2.22 [112]. Cotton cores were coated by carbon black nanoparticles and inserted into a polystyrene foam. When it is working, the temperature of the side surfaces is lower than the environment, making it possible to draw energy from the environment. Based on the calculation of this work, an evaporation rate of 1.62 $kg \cdot m^{-2} \cdot h^{-1}$ was achieved under 1 sun (equal to ~ 110% of the solar conversion efficiency). Song et al adopted similar idea that takes environmental energy into the evaporation system to generate cold vapour [113]. The temperature of the cold region is obviously lower than the environment temperature, which makes it possible to obtain energy from the environment. Carbon black was deposited on a piece of paper and the

paper was folded to cover a vertical foam, which floated the whole structure on the water. By increasing the evaporation area and decreasing parts of the evaporator temperature, this structure realized a remarkable evaporation rate of 2.20 $kg \cdot m^{-2} \cdot h^{-1}$ under 1 sun (equal to solar conversion efficiency of ~131%) based on their calculation.

Figure 2.22 Image of the cylindrical solar vapour generator [112].

2.2.5 Solar thermal conversion efficiency

Solar thermal conversion efficiency reflects the evaporation performance of solar evaporators and also indicates the upper limit of the evaporation rate [114]. The most widely used efficiency calculation method is based on the ratio of the energy used for evaporation to the energy of solar irradiation input [42, 78, 82, 115, 116]:

$$\eta = \frac{E_{evap}}{E_{input}} \times 100\% \tag{2-1}$$

$$E_{evap} = mh_{LV} \tag{2-2}$$

$$E_{input} = C_{opt} q_i \tag{2-3}$$

$$h_{LV} = Cp_{water}\left(T - T_0\right) + H_{LV} \tag{2-4}$$

E_{evap} denotes the energy used to evaporate water; E_{input} is the energy input of solar irradiation; m is the mass flux; h_{LV} is the total enthalpy required for liquid-vapour transition including sensible heat and the enthalpy of vaporization; C_{opt}

is the optical concentration; q_i is normal direct solar irradiation input (1 kW·m^{-2}); Cp_{water} means the water specific heat capacity (~4.2 kJ·kg^{-1} at 1 atm); T and T_0 are the final temperature (100°C) and initial temperature of water; H_{LV} is the water enthalpy of vaporization (~2260 kJ·kg^{-1} at 1 atm).

Based on the equations above, slight differences occurred in different works. In some works, the sensible heat of water was directly overlooked [31, 71, 73, 79]. In some literature, T denotes the final surface temperature rather than 100°C [106, 117]. Wang et al used the enthalpy of vaporization (2380 kJ·kg^{-1}) at the measured equilibrium temperature (50°C) rather than that at 100°C (2260 kJ·kg^{-1}) [71]. The calculation of the solar thermal conversion efficiency is not uniform and needs to be further studied based on the evaporation mechanism to determine the upper limit of evaporation rate.

The environment temperature, humidity and air turbulence affect the solar conversion efficiency as well. At the same time, solar concentration has an obvious effect on the efficiency, and generally, higher optical concentration leads to a higher solar conversion efficiency [6, 42, 78, 109, 115].

The upper limit of an efficiency should be less than 100%, while the solar conversion efficiency beyond 100% was reported in some works. Song and Li et al broke through the conversion efficiency upper limit (100%) under 1 sun by drawing environmental energy into the solar evaporation system [112, 113]. Wu et al coated wood with polydopamine and achieved the conversion efficiency above 100% (126% under 2 sun and 135% under 3.5 sun) [78]. They observed the burst of vapour bubbles on the solar absorber surface, and some water was directly transferred into the air without evaporation. This greatly saved relating evaporation energy and explains the conversion efficiency beyond 100%. Zhao et al achieved a solar conversion efficiency of 94% via hierarchically nanostructured gels, and further proved the vaporization enthalpy was lowered in the molecular meshes by experiment and calculation [31]. The solar evaporation mechanism and the solar conversion efficiency calculation deserve more discussion [114, 118].

2.3 Salt management

2.3.1 Salt accumulation problems

A typical solar evaporator floats at the water-air interface, which usually has a thermal insulation layer to localize the heat on the evaporation surface, known as interfacial evaporator (IE) [42, 119-121]. However, when applied on real seawater, salt will precipitate on the photothermal materials, reducing its solar absorption and blocking the water transport channels [122]. The accumulated salt will gradually slow down the evaporation and finally stop the whole system.

2.3.2 Salt back to bulk water

To solve the salt accumulation problem, a series of studies have been conducted. Designing salt back diffusion pathways back into the bulk water can forbid salt to accumulate on the evaporation surface. Kuang et al. drilled channels in a surface-carbonized wood [123]. With evaporation, salt participates on the surface and diffuses back through the pits, wood channels and drilled channels (Figure 2.23). This self-regenerating solar evaporator exhibits a high efficiency (75%) in 20 wt% NaCl solution under 1 sun and achieves 100 h continuous operation. Zhang et al. make the salt diffuse back by introducing polyester pillars under the evaporation surface and demonstrate the anti-salt-clogging performance can be changed by changing the number of the pillars [124]. Similarly, Ni et al. design a salt-rejecting floating solar still by adding wicks under the evaporation surface [125]. Xu et al. decoupled solar absorbing and water pump into different layers [126]. The absorbing layer is hydrophobic to forbid salt accumulation and the water transport system beneath is hydrophilic to dissolve salt back to the bulk water.

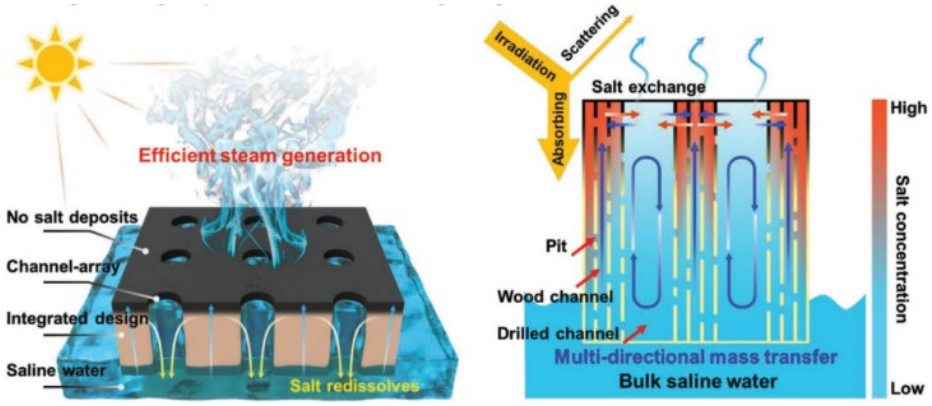

Figure 2.23 Self-regenerating solar evaporator design, and multidirectional mass transfer in the evaporator [123].

In addition to salt diffusion back to the bulk water, casting salt crystals back is another solution. Kashyap et al. reported an anti-clogging graphite film with pores inside, through which salt crystals would fall back into the bulk water to make the evaporation surface self-clean (Figure 2.24) [122]. Xia et al. proposed a self-rotating solar evaporator (Figure 2.25) [127]. Salt precipitates on the top surface of the cylindrical evaporator. When the gravity balance is upset, the cylindrical evaporator will rotate to sink the top surface with salt crystals in the bulk water to regenerate.

Figure 2.24 Schematic of the anti-clogging salt solar evaporator [122].

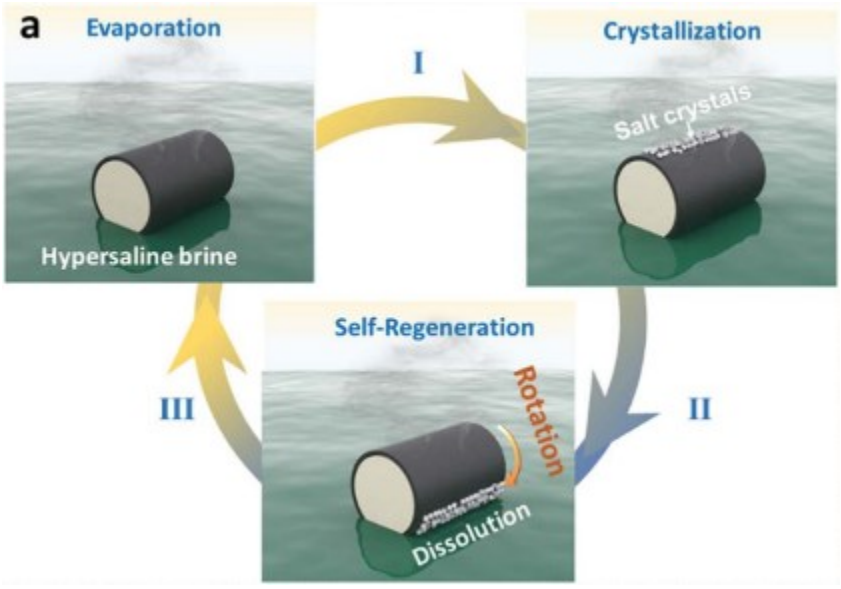

Figure 2.25 Schematic of the self-rotating solar evaporator [127].

2.3.3 Salt harvesting

Discarding salt back to the bulk water is an easy way to allow the solar evaporator to work continuously. However, considering the salt value, salt should not be treated as a waste discharging back to the sea, but a high added-value product. A ton of seawater contains 35 kg sea salt costing $4.2 ($120 per ton) and a ton of fresh water equals $2.8 on average for 30 main cities in the US (Statista, 2021). Thus, the price of the salt in 1 ton seawater is even higher than 1 ton fresh water. Harvesting salt with SVG is the optimal strategy from both environmental and economic perspectives, realizing zero liquid discharge.

Wu et al. made a three-dimensional solar evaporator by 3D printing, with salt precipitation on the top (Figure 2.26). The crystallized salt can be easily harvested manually.

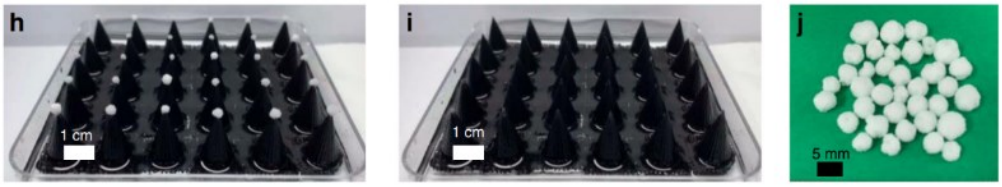

Figure 2.26 Salt harvesting manually [128].

Shi et al. designed a 3D cup solar evaporator (Figure 2.27), which can be operated at high salt concentration (27 wt% NaCl solution). Salt precipitates on the walls and can be removed by a stainless steel scraper manually.

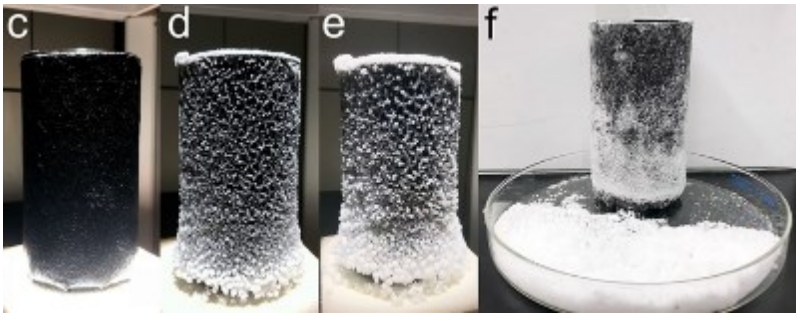

Figure 2.27 Salt harvesting by a stainless steel scraper [129].

Recently, attention is shifting to an umbrella-shaped evaporator [130-133]. It features a central water supply and an edge salt collection (Figure 2.28). This type of evaporator is promising as it achieves SVG and salt harvesting at the

same time. However, very few studies have been dedicated to understand its structural affection on the system energy efficiency in SVG, the salt precipitation behaviours, the salt falling mechanism, and more importantly how the real seawater affects its continuous operation.

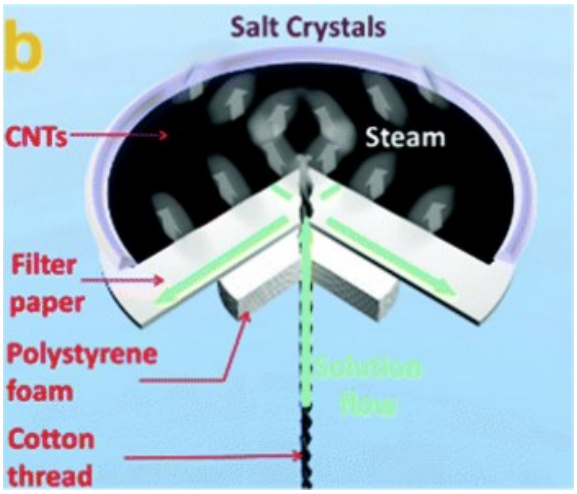

Figure 2.28 Continuous solar vapour generation with salt harvesting [130].

2.4 Chapter summary

The research related to seawater desalination driven by solar energy, photothermal materials, solar evaporator structures, and salt management have been reviewed in this chapter. Solar vapour generation is a promising technology for obtaining fresh water from brine or sewage because of its high efficiency in solar thermal conversion process. From the literature review, we can conclude the following:

i) Seawater desalination technology falls into two categories: thermal-based desalination (MSF and MED) and membrane-based desalination (RO and FO). MSF and MED processes are easy to scale up and easy to maintenance with easy pre-treatment procedures. However they consume much energy to vaporize the seawater. RO and FO processes utilize semi-permeable membranes to separate fresh water from saline water, which avoids the water vaporization enthalpy consumption. However, RO also requires much electricity energy to create high pressure to drive the process and FO costs much energy in draw solution regeneration process. All the most commonly used desalination methods above do not harvest salt, instead, they return salt

back as brine to the sea, which would potentially harm the ecological environment around. Solar energy is attracting more and more attentions to power the desalination processes above. Notably, solar vapour generation technology which directly converts solar energy into heat to evaporate water is promising due to its high efficiency and simple equipment.

ii) SVG is an integrated system, whose system energy conversion efficiency is greatly affected by photothermal materials, solar heating forms, and solar evaporator structures. So far, metals, metal alloys, metal oxides, metal nitrides and carbon materials as potential photothermal materials have been extensively explored but still show certain deficiencies. However, developing a high-efficient, low-cost, and durable material with easy availability still remains challenging for real industrial applications. As SVG is an interfacial mass transfer process, interfacial heating is the optimal heating form to achieve a higher energy efficiency. Different solar evaporators have been proposed in different labs. However, the solar evaporator structure still lacks adequate research to improve the system energy efficiency, especially lacks evaporation performance comparison in the same test environment. At the same time, the numeric simulation mechanism study linking the energy efficiency theories and the experiments is still lacking.

iii) When applied on real seawater, salt would precipitate on the photothermal material and gradually slow down the evaporation rate and finally stop the whole system. To solve the salt accumulation problem, a series of studies have been conducted, including designing salt back diffusion pathways into the bulk solution, removing salt mechanically, and returning salt crystals back to the bulk water. By calculation, the price of the salt in 1 ton seawater is even higher than 1 ton fresh water. Harvesting salt with SVG is the optimal strategy. Recently, attention is shifting to an umbrella-shaped evaporator, which can achieve SVG and salt harvesting at the same time. However, very few studies have been dedicated to understand its structural advantages, the salt precipitation behaviours, the salt harvesting mechanism, and more importantly how the real seawater affects its continuous operation.

Based on the research gaps mentioned above, this thesis is performed as follows:

1. Designing a light-trapping surface structure with open pores and channels would further improve the solar absorption for better SVG performance by locking the solar irradiation into the surface. A polypyrrole-dopamine nanofiber light-trapping coating is proposed in Chapter 3. The surface physical microstructure and chemical structure are characterized, and the formation mechanism is proposed. Finally, the light-trapping performance is tested.

2. The nanofiber coating is directly coated on a polystyrene foam to be an interfacial evaporator in Chapter 4. The evaporation performance of the coatings with different microstructures are compared by energy efficiency. The salt precipitation and back diffusion are also tested by salt water.

3. A double-sided evaporation umbrella evaporator is proposed in Chapter 5. Its structural advantages in SVG over a typical IE have been proved by both experiments and simulations. The factors in energy efficiency are analysed in details by simulation.

4. Benefiting from the rational design, salt will fall down automatically from the edge by gravity. The factors affecting the salt harvesting, the salt precipitation, growth and falling behaviours at a micro level, and the salt harvesting mechanism are studied in Chapter 6. Finally, a facile method to determine if the pre-treated seawater can achieve salt falling is proposed.

5. To address the water supply and distribution problems of the double-sided evaporator, a suspending evaporator with top water supply and surface water distribution systems is developed for concurrent solar evaporation and salt harvesting. The evaporation performance of this suspending evaporator, salt accumulation simulation, a radial arterial water distribution system and a floriform evaporation surface are performed in Chapter 7 to make this evaporator applicable for large area application.

Chapter 3
Polypyrrole-dopamine nanofiber light-trapping coating

3.1 Introduction

The photothermal material is an important factor in determining the total energy captured into the solar vapour generation system. Developing a high-efficient, low-cost, and durable material with easy availability still remains challenging for real industrial applications. At the same time, the solar absorptance of a material determines its upper limit of the solar energy absorption. Designing a light-trapping surface structure with open pores and channels would break this limit by locking the solar irradiation into the surface.

Polypyrrole (PPy) is well known as a black conjugated conducting polymer, which exhibits broadband light absorption spectra, making it an excellent photothermal material [77, 82]. PPy has excellent chemical and thermal stability, and it is insoluble in water and other conventional solvents [134]. As PPy is electrically conductive, it has been widely explored in battery electrodes, supercapacitors, sensors, electrocatalysis, electromagnetic wave absorption and other electricity relating fields [135-143]. Moreover, the morphology of PPy particles can be tuned from globular to fibrous by introducing dopamine (DA) in the reaction solvent as demonstrated in previous reports [83, 84, 144]. Dopamine is the main composition of adhesive proteins in mussels displaying excellent interfacial adhesion properties on various substrates [144]. It is worth mentioning that, the self-polymer of dopamine, polydopamine (PDA), is black and insoluble, also exhibiting superior solar thermal conversion efficiency [78].

In this chapter, a novel and facile ultrasonic spray coating method is proposed to produce a nanofiber light-trapping coating by copolymerization polypyrrole (PPy) with dopamine (DA). This coating can be rapidly (30 min reaction time) synthesized at room temperature without using any prepared fibrous template as the substrate, greatly simplifying production procedures. This nanofiber coating can be directly coated on various surfaces to make them light-trapping. The fibrous surface structure enables multiple reflections of sunlight inside the pores and channels and significantly improves solar absorption at different incident angles across the full solar spectrum. Due to capillary force, this

fibrous coating has excellent water spreading for water transportation, making it possible to integrate the water transport system into the top solar absorbing layer. Also, this study demonstrates that, the surface structure can be easily tuned into granular or plane-granular or plane-fibrous structures by using ammonium persulfate (APS) as oxidant or sodium dodecyl benzene sulphonate (SDBS) as surfactant. The corresponding formation mechanisms of different structures are also proposed based on qualitative chemical characterization. This nanofiber coating shows great promise for solar vapour generation and other applications based on PPy materials, especially for those requiring certain specific surface morphology.

The preparation method of this coating is in Section 3.2. Its surface physical microstructure is analysed in Section 3.3 and its chemical structure is analysed in Section 3.4. Furthermore, its formation mechanism is proposed in Section 3.5. The light-trapping properties were tested in Section 3.6. Finally, conclusions are given in Section 3.7.

3.2 Coating preparation

3.2.1 Raw materials

Pyrrole (Py) was purchased from Alfa Aesar. Dopamine hydrochloride was obtained from Acros Organics. Anhydrous ethanol and Iron (III) chloride ($FeCl_3$) were purchased from Fisher Chemical. Hydrochloric acid (HCl, 37 wt%) and sodium dodecyl benzene sulfonate (SDBS) were from Sigma-Aldrich. Tween 20 was purchased from BioServ. Ammonium persulfate (APS) was from Honewell. Deionized water (DI water) was made in the lab.

3.2.2 Coating method

Figure 3.1 shows the fabrication process of the PPy−DA nanofiber coating. Briefly, this process needs to spray a Py−DA solution (mixture A) onto the substrate pre-wetted with an oxidant solution (mixture B) by ultrasonic spray coating at room temperature (10 s of spraying time and 30 min of reaction time). The photographs of the polystyrene (PS) foam before and after coating with a PPy−DA nanofiber are also shown in Figure 3.1, presenting a white PS

foam and a black PPy−DA coating appearance. The PS foam helps to reduce the heat loss to the bulk water.

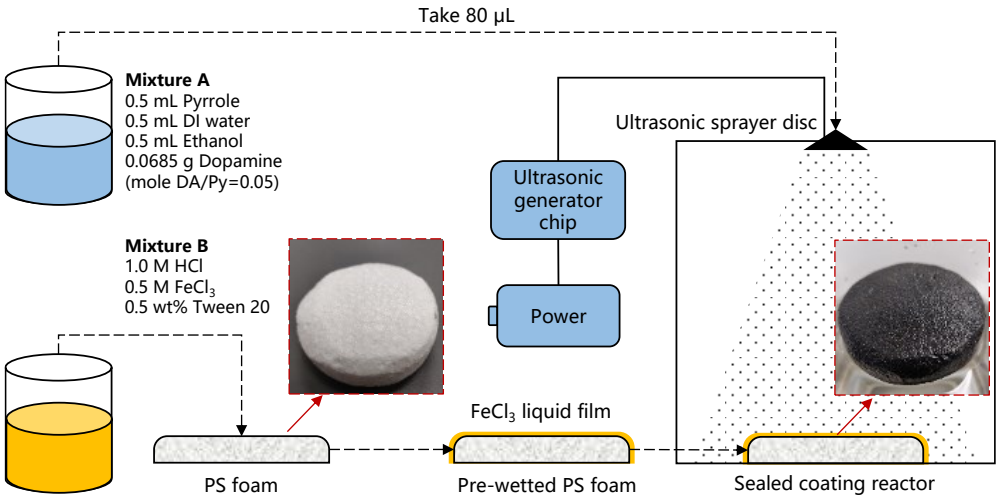

Figure 3.1 The fabrication process of polypyrrole nanofiber light-trapping coating by ultrasonic spray coating.

As shown in Figure 3.1, to obtain Mixture A, DA hydrochloride (0.0685 g) was dissolved in 0.5 mL of DI water. Then, 0.5 mL of pyrrole (Py) was added to the above mixture. The molar ratio of Py-DA was 0.05. Ethanol (0.5 mL) was added to completely dissolve Py in the mixture. By doing so, Py and DA monomers can be fully mixed. To obtain Mixture B, $FeCl_3$ was added in 1 M HCl solution to get a 0.5 M $FeCl_3$ solution. To improve the wettability of the PS foam substrate (with a thermal conductivity of 0.035 $W \cdot m^{-1} \cdot K^{-1}$), 0.5 wt% Tween 20 was added in Mixture B. PS foam was cut into a disc and further abraded by a sandpaper (P120) to remove its hydrophobic surface and improve the bonding strength between the coating and the PS substrate. The as-prepared PS disc substrate was finally 4.8 cm in diameter and 1.5 cm in thickness with a rough surface. Then, the substrate was washed with DI water and dried at 40 ºC for 2 h. After that, the substrate was immersed in Mixture B for 10 min and placed in a sealed coating reactor at room temperature (~20 ºC). 80 µL of Mixture A was dropped on the ultrasonic sprayer disc, and then the ultrasonic spray coating (113 kHz vibration) process was carried out until Mixture A was completely atomized in the sealed coating reactor (it took ~10 s). The polymerization reaction took 30 min. After that, the coated solar vapour generator was washed with plenty of DI water and ethanol in turns and dried

at 40 ºC for 2 h. This nanofiber can be easily coated on a variety of surfaces, such as glass, wood, plastic, and filter paper (Figure 3.2)

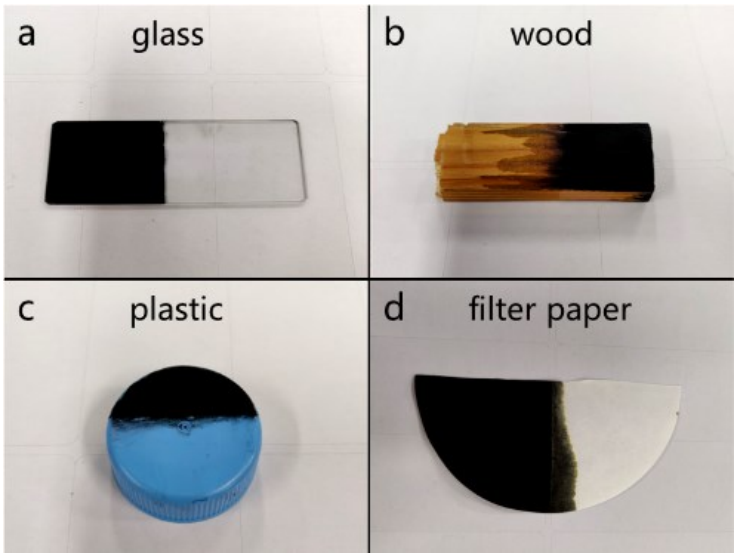

Figure 3.2 Fibrous PPy-DA coatings on (a) glass, (b) wood, (c) plastic and (d) filter paper.

3.3 Surface physical microstructure

The detailed surface microstructures were characterized by field emission scanning electron microscopy (FESEM, Hitachi SU8230) with energy dispersive X-ray spectroscopy (EDS). At the micro level, the cell walls consisting PS foam are smooth (Figure 3.3a). After coating PPy alone, the surface presents a rough plane structure with small bulges (Figure 3.3b), on which the sunlight unabsorbed will be easily reflected out.

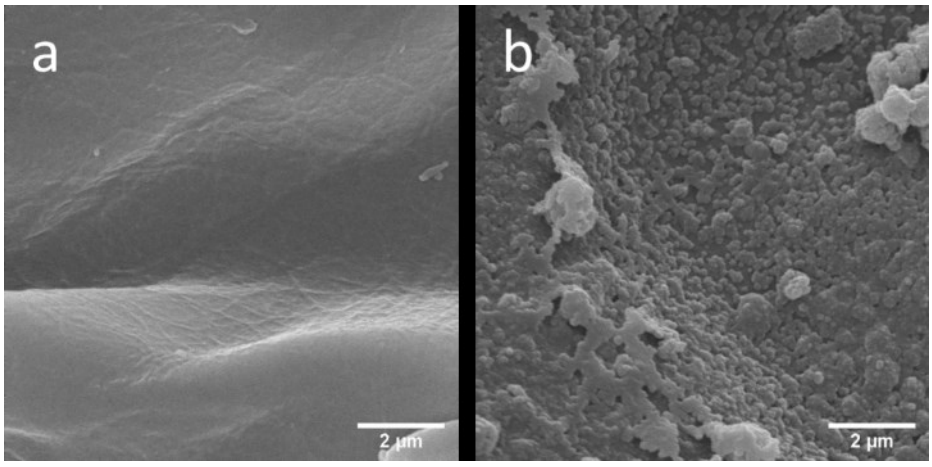

Figure 3.3 (a) Pristine abraded polystyrene foam. (b) Plane PPy coating.

When dopamine (DA) was added into Mixture A (mole DA/Py is 0.05), the plane structure was tuned into a fibrous PPy-DA nanofiber coating and the resulting fibre was ~100 nm in diameter (Figure 3.4a-c). The fibres intertwine randomly, making the coating stronger. Sunlight shooting into the gaps among the fibres will reflect inside, allowing this fibrous structure to trap more sunlight to further improve the solar-to-thermal conversion efficiency.

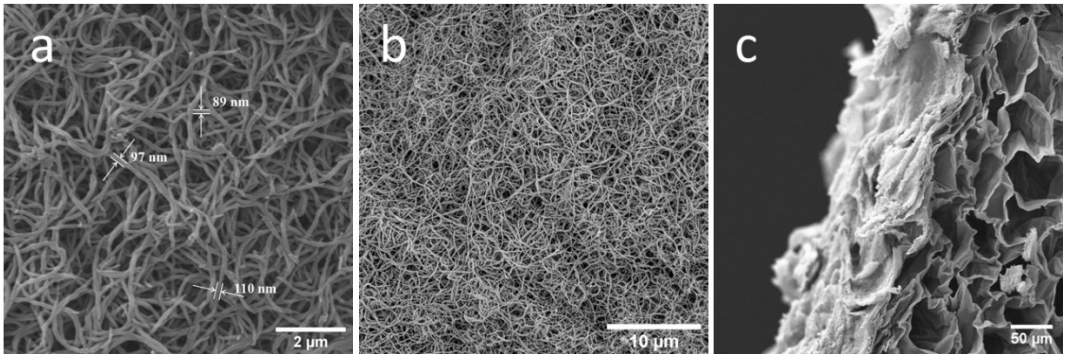

Figure 3.4 (a-b) Fibrous PPy-DA nanofiber coatings with different scales and (c) its side view.

$FeCl_3$ and ammonium persulfate (APS) are commonly used as the oxidant for PPy oxidative polymerization. If APS is used to replace $FeCl_3$ as the oxidant for this PPy-DA coating, a granular structure would be obtained rather than a fibrous one (Figure 3.5).

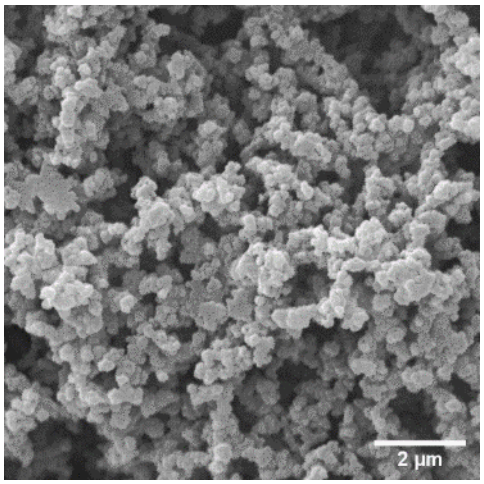

Figure 3.5 Granular PPy-DA coating by APS.

The mole ratio DA/Py also affects the surface structure, when DA/Py was decreased to 0.01, the fibers became very short (Figure 3.6a); when DA/Py was increased to 0.1, the gaps between the fibers became large (Figure 3.6b).

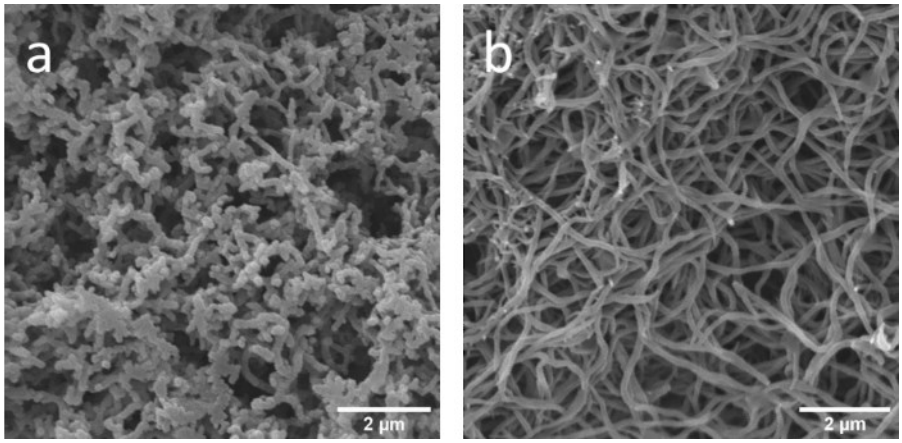

Figure 3.6 The fibrous PPy-DA ($FeCl_3$) coatings in different DA/Py ratios. (a) DA/Py = 0.01 mole. (b) DA/Py = 0.1 mole.

H^+ plays an important role in this reaction, if HCl is not added in Mixture B, the coating would turn into a coexistence morphology of fibrous and granular structures (Figure 3.7a). Similarly, if HCl is replaced by H_2SO_4 with the same H^+ concentration, we could also obtain a fibrous structure (Figure 3.7b).

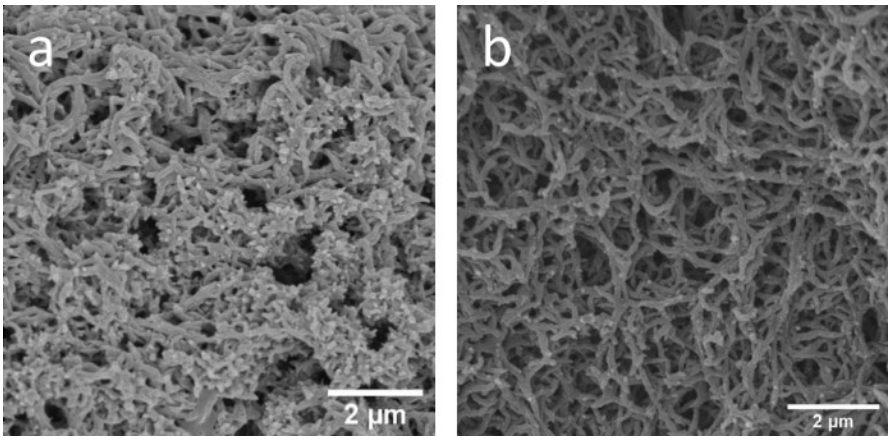

Figure 3.7 (a) PPy-DA coating without HCl. (b) HCl was replace by H_2SO_4 in the same concentration of H^+.

The surface structure can be further tuned by using different surfactant and it is easy to obtain more complex composite structures. As pyrrole is slightly soluble in water (60 mg/mL at 20 °C), ethanol was added to help pyrrole completely dissolve in water in Mixture A. However, during the ultrasonic spray coating process, if Tween 20 (solubilizer) is not added in Mixture B, aqueous solution (Mixture B) would first extract the hydrophilic components from Mixture A (i.e. ethanol, dopamine, water), and then with reaction going

on, pyrrole would partly dissolve into Mixture B to copolymerize with DA, leaving part of pyrrole to self-polymerize on the surface (Figure 3.8).

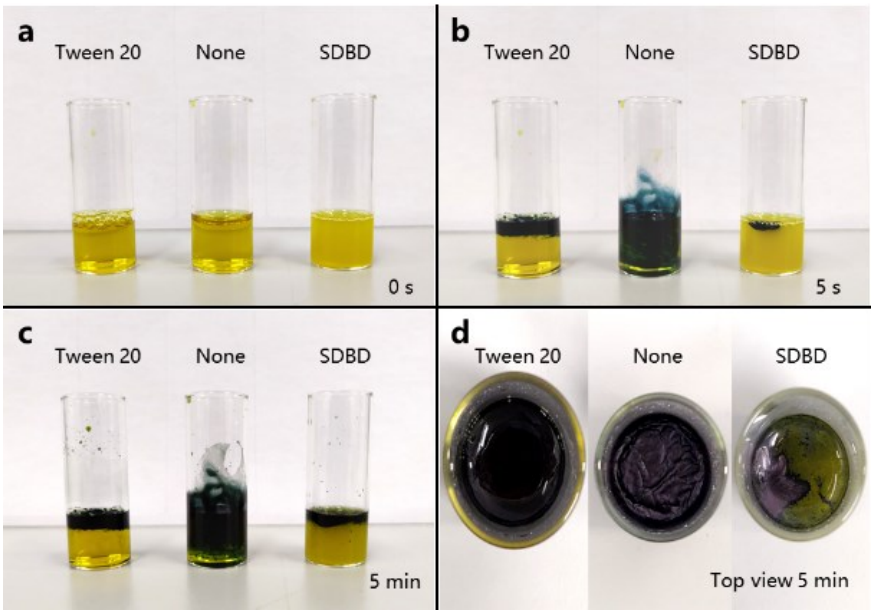

Figure 3.8 Effect of surfactants on the surface morphology of PPy-DA fibrous coating. (a) Tween 20, SDBS and no surfactant cases at 0 s. (b) Side view at 5 s after dropping 20 µL Mixture A into the test tubes. (c) Side view at 5 min. (d) Top view at 5 min.

Therefore, we could get a fibrous coating with a pierced PPy film on the top (Figure 3.9a). The PPy film on the top can also be reinforced by using sodium dodecyl benzene sulphonate (SDBS) as surfactant in Mixture B to get a plane-fibrous composite structure (Figure 3.9b). Similarly, if SDBS is used as surfactant and APS as oxidant in Mixture B, we could get a plane-granular structure (Figure 3.9c).

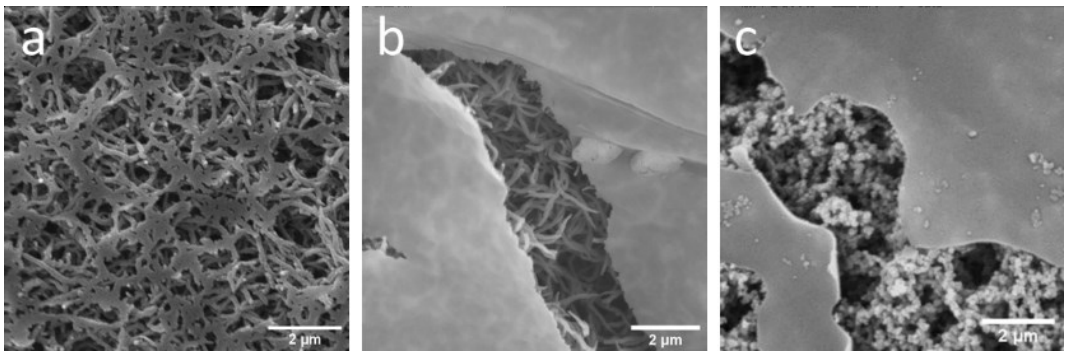

Figure 3.9 (a) PPy-DA coating without surfactant (Tween 20). (b) Plane-fibrous structure. (c) Plane-granular structure. For b and c, the cracks were intentionally made to reveal the structures underneath.

The plane, granular and fibrous structures were used to conduct the following comparative study. The BET surface area was measured by surface area and porosity analyzer (Micromeritic TriStar 3000). After tuning structure, the coating specific surface area significantly increased (Figure 3.10), from plane structure (12.57 $m^2 \cdot g^{-1}$) to granular structure (29.77 $m^2 \cdot g^{-1}$), with fibrous structure (34.05 $m^2 \cdot g^{-1}$) being the highest. Larger specific surface area indicates more light-trapping gaps and channels in the coating.

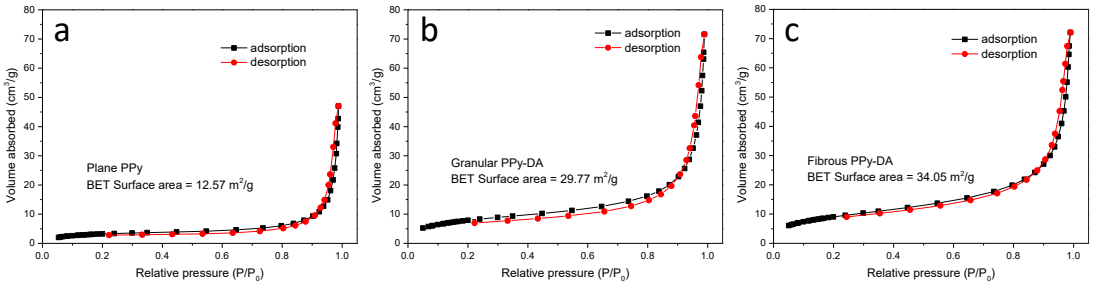

Figure 3.10 BET surface area calculated from nitrogen adsorption-desorption isotherms. (a) Plane PPy structure. (b) Granular PPy-DA structure. (c) Fibrous PPy-DA structure.

This fibrous light-trapping structure makes the evaporating surface highly hydrophilic. The water spreading property on the coatings was captured by a goniometer (KSV CAM 200). Water drop spread out and disappeared into the surfaces of granular PPy-DA and fibrous PPy-DA coatings in less than one second (Figure 3.11), providing a good water transport to the top evaporating surface by capillary force. By contrast, the plane PPy took 5 seconds. The resulting nanofiber can be directly coated on the thermal insulating layer, integrating the water transport system in the top solar absorbing layer. Therefore, it does not require to be coated on an extra water transport layer (e.g. filter paper, airlaid paper or cotton) [54, 118, 145].

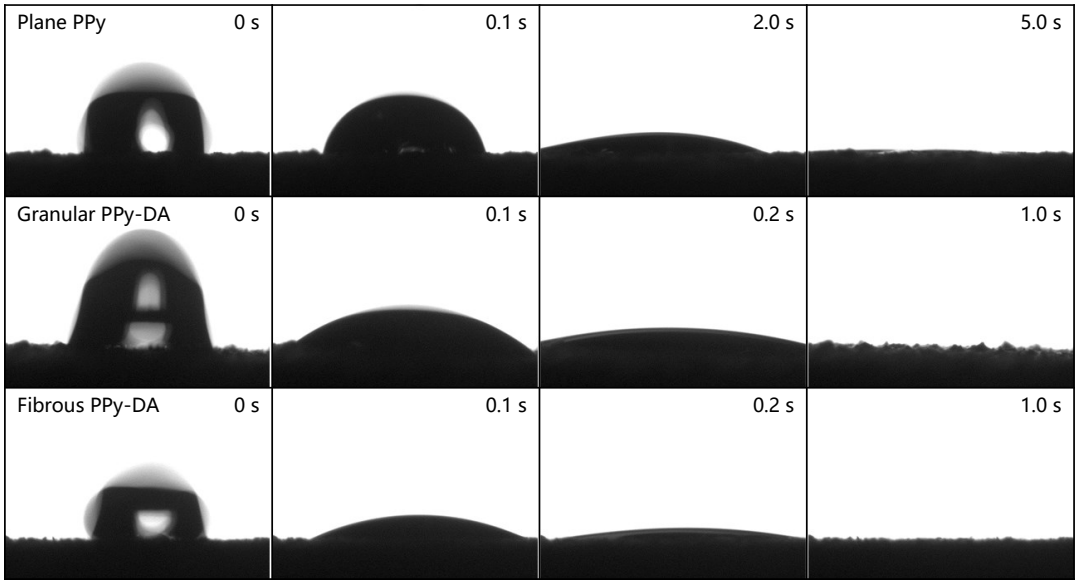

Figure 3.11 Time-lapse snapshots of a water drop (10 µL) spreading on the plane PPy, granular PPy-DA and fibrous PPy-DA coatings on abraded PS foams.

3.4 Surface chemical structure

The plane, granular and fibrous structures of the coatings were qualitatively characterized by Fourier transform infrared (FTIR, Thermo Scientific Nicolet iS10) spectrometer with an attenuated total reflection (ATR) accessory from 4000 to 400 cm^{-1} at room temperature (Figure 3.12). The PPy characteristic peaks at 1543 and 1174 cm^{-1} are respectively assigned to the C=C stretching vibration and C-N stretch bending of the five-membered ring [146]. The transmission band at 904 cm^{-1} is due to =C-H in-plane vibration [118, 147]. The peaks at 1299 cm^{-1} are due to C-O stretching, indicating PPy body was oxidized during synthesis and the presence of catechol structure from dopamine in granular and fibrous PPy-DA structures [148]. The peak for plane PPy at 3437 cm^{-1} is due to N-H stretching vibration. The broad peaks for granular and fibrous structures at 3430 and 3433 cm^{-1} respectively are due to N-H and O-H stretching vibrations in catechol groups, indicating that successful copolymerization with dopamine [149]. The peaks at 1700 and 1735 cm^{-1} for granular and fibrous PPy-DA respectively are due to C=O stretching vibration, indicating carbonyl group [150]. In fibrous and granular structures the peaks at 2958 and 2924 cm^{-1} (C-H symmetrical and C-H asymmetrical stretching in the aromatic ring respectively) also confirm the incorporation of dopamine into PPy [146].

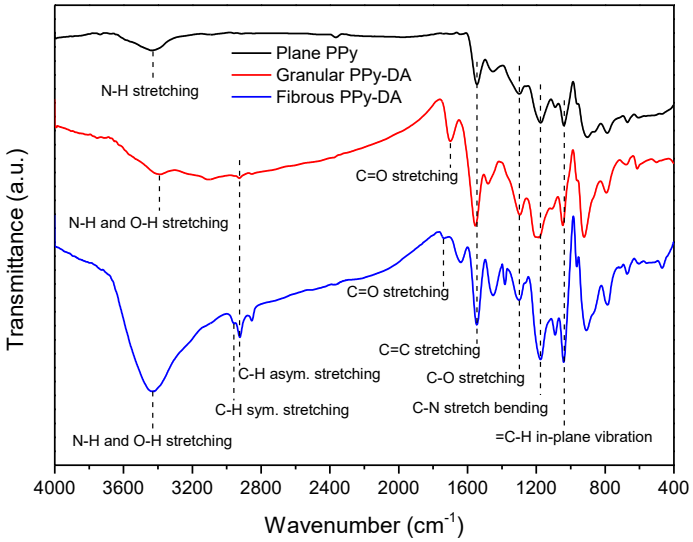

Figure 3.12 FTIR spectra of plane, granular and fibrous structures of the coatings.

The polymer structures of plane PPy, granular PPy-DA and fibrous PPy-DA were further verified by X-ray photoelectron spectroscopy (XPS, Specs EnviroESCA). It was conducted in 7 mbar of argon environment, and thusly argon peaks are present in the survey spectra (Figure 3.13). There are oxygen peaks in all cases, even in pure PPy sample, indicating that PPy was oxidized during the synthesis process. Chlorine peaks in the survey spectra indicate that HCl was successfully doped. Sulfur was also found in the granular PPy-DA. Iron was not clear in the fibrous PPy-DA.

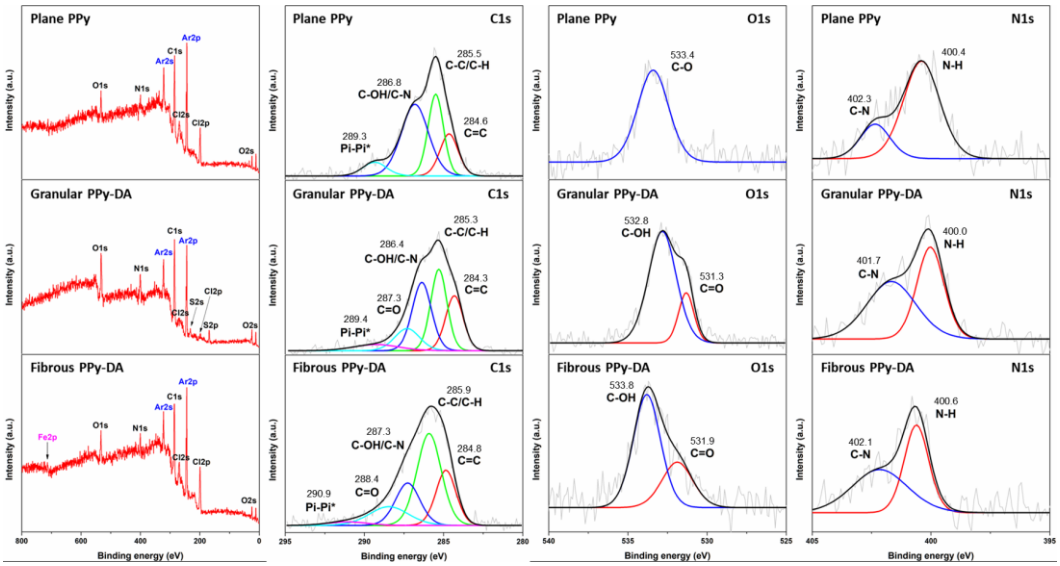

Figure 3.13 XPS survey spectra and C 1s, O 1s, and N 1s spectra for plane PPy, granular PPy−DA, and fibrous PPy−DA.

As XPS is a surface analysis technique (typically less than 5 nm in depth), Energy Dispersive X-ray Spectrometer (EDS) was further used to explore a deeper range typically from 1 to 2 μm. Abundant iron was observed distributed in the whole field (Figure 3.14), indicating iron mainly distributed inside the PPy-DA nanofibres. Fibrous PPy-DA contains up to 9.01 wt% Fe, by contrast, plane PPy without dopamine contains only 0.94 wt% (Table 3.1). Granular and fibrous PPy-DA have both C-OH peaks and C=O peaks in C1s and O1s spectra. Peaks of sp^2 carbons (C=C) from pyrrole or benzene rings were detected in all cases, accompanied by sp^3 carbons peaks (C-C and C-H). C-N peaks in C1s and N1s spectra were assigned to the C-N groups from both pyrrole and dopamine. π-π* interaction was also observed due to pyrrole and benzene aromatic rings [151, 152].

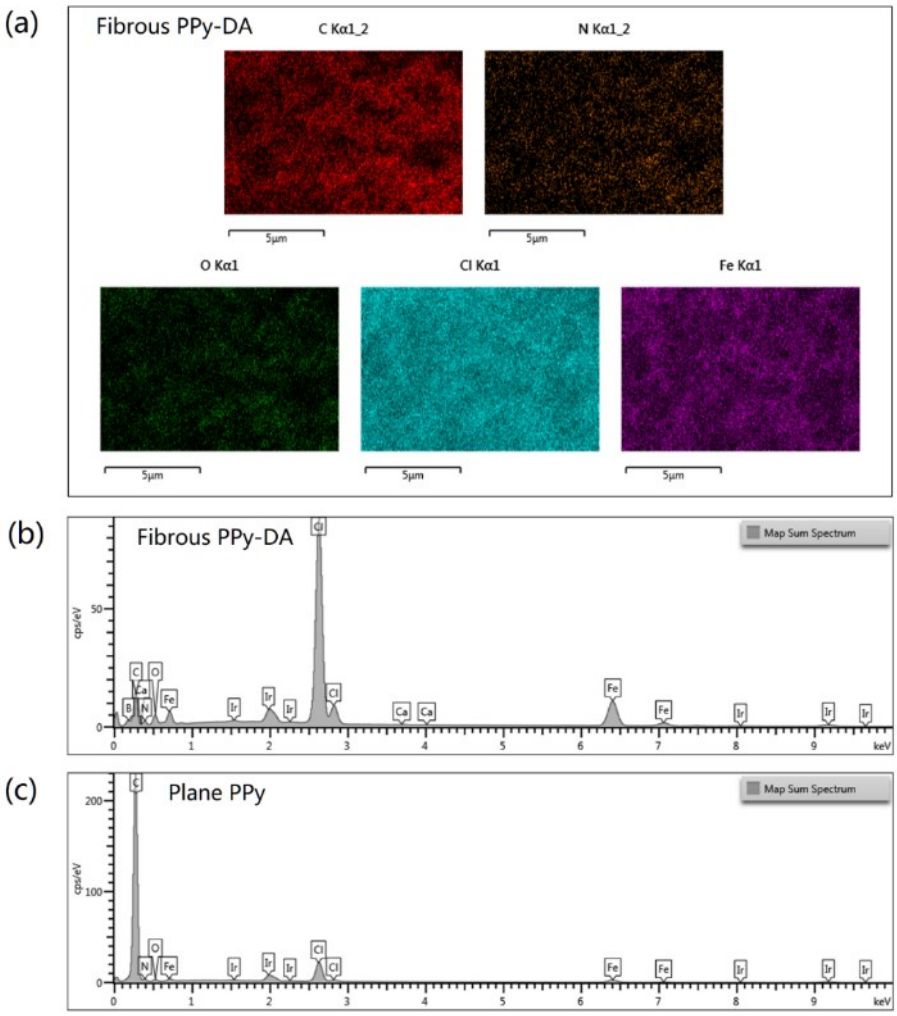

Figure 3.14 (a) Fibrous PPy-DA coating EDS elemental mapping (C, N, O, Cl and Fe). (b) Fibrous PPy-DA coating EDS spectrum. (c) Plane PPy EDS spectrum.

Table 3.1 Element contents for fibrous PPy-DA and plane PPy coatings from EDS.

Element	Fibrous PPy-DA [wt%]	Plane PPy [wt%]
C	52.54	84.26
N	11.56	10.14
O	9.27	2.78
Cl	17.62	1.88
Fe	9.01	0.94
Total	100	100

3.5 Formation mechanism

As PPy and PDA are both insoluble in conventional solvents, traditional solution-based characterization methods are unsuitable and thereby the detailed structure of PDA alone remains unclear [153]. Therefore, obtaining the PPy-DA composite structure is more challenging. Here in order to explain the formation mechanism of plane PPy, fibrous PPy-DA and granular PPy-DA different structures, a schematic illustration is given in Figure 3.15.

For plane PPy (Figure 3.15), pyrrole self-polymerizes as backbones and also interchain links itself during the oxidation, accompanied by side chains at the same time, which makes a plane morphology [84, 154, 155].

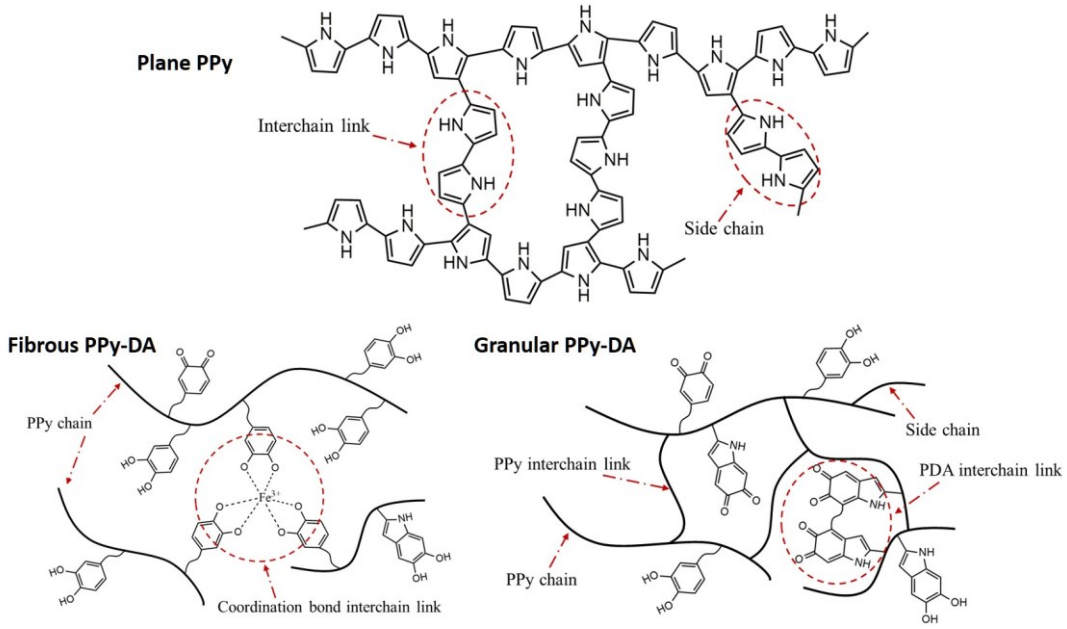

Figure 3.15 Schematic illustration of the plane PPy, fibrous PPy-DA, and granular PPy-DA structure formation mechanism.

For fibrous PPy-DA (Figure 3.15), dopamine would occupy the active sites on the PPy backbones to restrain PPy self interchain links, resulting a fibrous structure. Meanwhile, Fe^{3+} could also form coordination bond interchain link with three catechol groups (from dopamine) to crosslink the PPy chains into a stronger one, which explains the presence of Fe (9.01 wt%) inside the nanofibers from EDS results [156, 157]. The catechol groups connected to the PPy backbones contribute better water spreading and adhesion to the whole structure.[144, 158] It should be noted that, HCl is important for the formation of the fibrous structure. Synthesizing PPy by oxidation (e.g. $FeCl_3$) would also produce HCl (Figure 3.16a). Therefore, adding HCl into the oxidant could weaken the interchain links of PPy itself. Without HCl, the morphology would turn into a fibrous and granular composite structure.

For granular PPy-DA (Figure 3.15) which was obtained by ammonium persulfate (APS) oxidization. According to the standard electrode potentials, APS is a much stronger oxidant than $FeCl_3$ ($Fe^{3+}+e^- \rightarrow Fe^{2+}$ 0.77 V, $S_2O_8^{2-}+2e^- \rightarrow 2SO_4^{2-}$ 2.01 V), hence it can both link dopamine to the PPy backbones and create PPy and PDA interchain links at the same time. Due to the crosslinks, when the droplets (from the ultrasonic sprayer) of pyrrole and dopamine drop into oxidizer solution (APS), they would instantly form granular structures. FTIR and XPS results also confirm this, as obvious C=O peaks are detected from 5,6-indolequinone (one of the intermediates, Figure 3.16b), which is the precursor of PDA [159].

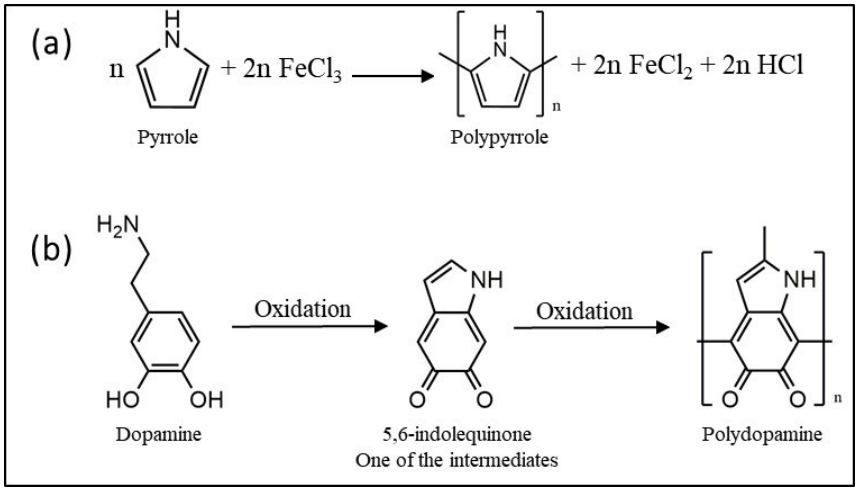

Figure 3.16 (a) Reaction of pyrrole oxidative polymerization into PPy by $FeCl_3$. (b) Formation of PDA precursors 5,6-indolequinone (one of the intermediates).

To sum up, stronger oxidant (APS) can turn the fibrous structure (by $FeCl_3$) into granular due to the instant crosslinks. To form the composite structures (plane-granular/plane-fibrous), aqueous oxidant solution preferentially extracts hydrophilic components and leaves part of the hydrophobic pyrrole self-polymerize covering the fibrous or granular structures below. Tween 20 acts as solubilizer to dissolve the hydrophobic pyrrole monomer into the aqueous oxidant solution, directly exposing the fibrous and granular structures. On the contrary, SDBS would hinder the dissolution of pyrrole into the aqueous oxidant solution, hence reinforcing the covering formation. The interaction of these two effects leads to the above different surface structures.

3.6 Light-trapping performance

To confirm the light-trapping performance of the nanofiber coatings, the reflectance (R) and transmittance (T) spectra were measured in the ultraviolet-visible-near-infrared range from 250 to 2500 nm (Figure 3.17). The reflectance and transmittance spectra were measured by ultraviolet-visible-near-infrared (UV-Vis-NIR) spectrometer (PerkinElmer Lambda 950) with a 60 mm integrating sphere (PerkinElmer). In comparison with pristine PS foam, all the coatings significantly decreased the reflectance and transmittance, meaning improvements in absorptance (A). By calculation (calculation method is shown below and the results are summarized in Table 3.2), the plane PPy coating can absorb 95.34% solar energy across the solar spectral irradiance from 250 to 2500 nm, which indicates that polypyrrole itself is excellent solar-thermal material. After coating with granular PPy-DA, the solar energy absorptance increased to 96.62%. Further, the fibrous PPy-DA reached an impressive absorptance of 97.73%. Therefore, after tuning the surface structure, the PPy-DA nanofiber coating obviously improved the solar energy absorption by enabling multiple reflections within the pores and channels, trapping more light.

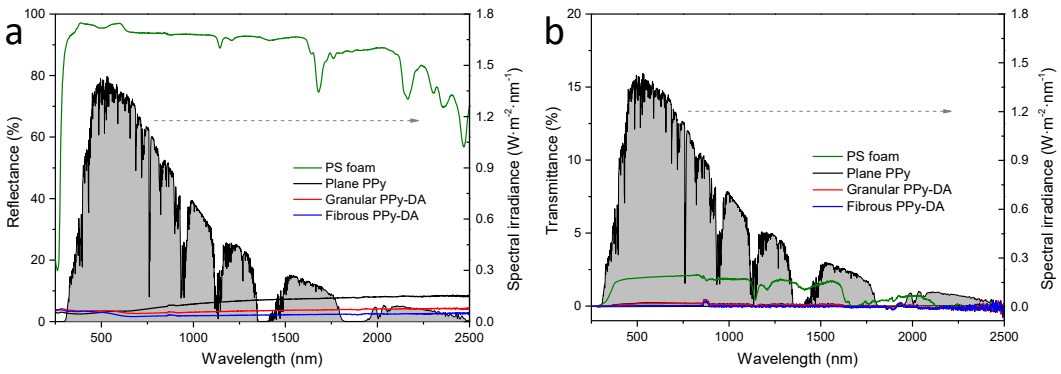

Figure 3.17 (a) Diffuse reflectance spectra and (b) transmittance spectra of PS foam, plane PPy, granular PPy-DA, and fibrous PPy-DA coatings on PS foam. The standard solar spectral irradiance (AM 1.5 G) serves as a background reference.

Solar energy absorptance calculations: the absorptance of the coatings is calculated by the following equation:

$$A = 1 - R - T \tag{3-1}$$

Where A is absorptance, R is reflectance and T is transmittance.

The solar energy absorption across the standard solar spectral irradiance (AM 1.5G) is calculated by the following equation:

$$A_{solar} = \frac{\int A \cdot I_{solar} d\lambda}{\int I_{solar} d\lambda} \tag{3-2}$$

Where A_{solar} is solar energy absorption, I_{solar} is solar spectral irradiance ($W \cdot m^{-2} \cdot nm^{-1}$) and λ is the wavelength (nm).

Similarly:

$$R_{solar} = \frac{\int R \cdot I_{solar} d\lambda}{\int I_{solar} d\lambda} \tag{3-3}$$

$$T_{solar} = \frac{\int T \cdot I_{solar} d\lambda}{\int I_{solar} d\lambda} \tag{3-4}$$

Table 3.2 Solar energy absorptance, reflectance and transmittance of different coatings and the pristine PS foam.

Samples	A_{solar} (%)	R_{solar} (%)	T_{solar} (%)
PS foam	5.53	92.7	1.77
Plane PPy	95.34	4.58	0.08
Granular PPy-DA	96.62	3.32	0.06
Fibrous PPy-DA	97.73	2.25	0.02

In real applications, most of the time sunlight does not irradiate on the earth vertically. Therefore, it is critical to study the influence of sunlight incident angles on the light-trapping structures. The solar evaporators were inclined to generate different incident angles. The surface temperature distribution at different light incident angles was detected by FLIR ONE infrared camera (sensitivity of 0.1 ºC). The surface average temperatures of plane, granular and fibrous coatings were compared at different incident angles (0º, 20º and 40º). As shown in Figure 3.18, in 0º incident light (vertical), granular and fibrous structures trapped more light, achieving 75.0 ºC and 75.7 ºC respectively. The plane structure can only reach 73.5 ºC. With the incident angle increasing to 40º, the temperature of the plane and granular structures dramatically decreased by 9.1 ºC and 10.5 ºC respectively. Although the granular structure contains lots of channels, the channels mostly located inside, leaving few open pores on the surface, which makes the granular structure reflect out some irradiation as well. By contrast, the surface average temperature of the fibrous structure only decreased 6.5 ºC, holding the final temperature of 69.2 ºC at 40º incident angle. As a consequence, PPy-DA nanofiber coating can trap more light and work at high efficiency at different sunlight incident angles. At the same time, it should be noted that the possible degradation of this polymer coating under long-term sunlight (especially the ultraviolet radiation) may cause contamination to the environment around, which should be further studied before real application.

Incident angle	Plane PPy	Granular PPy-DA	Fibrous PPy-DA
0°	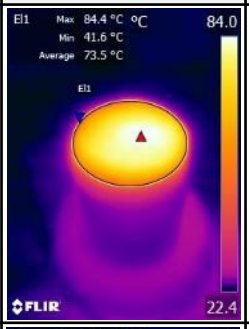	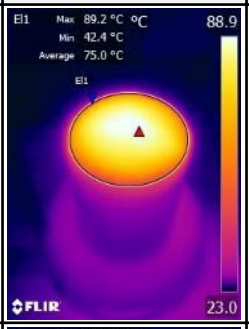	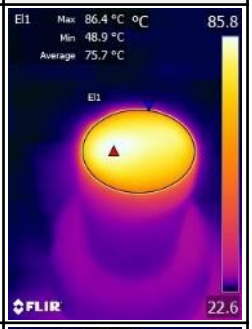
20°	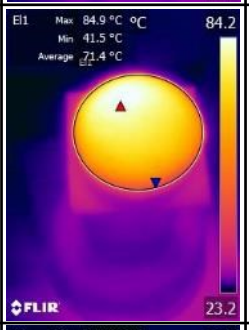	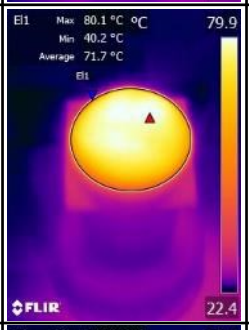	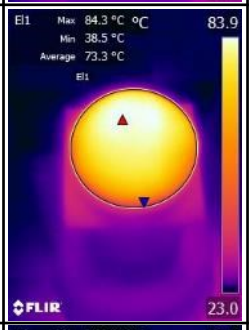
40°	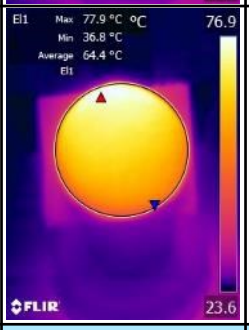	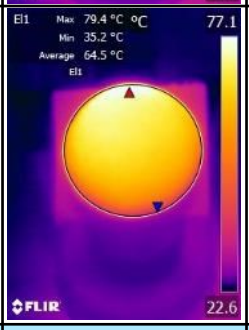	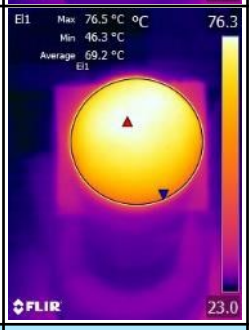
ΔT (T0°-T40°)	9.1°C	10.5°C	6.5°C

Figure 3.18 Infrared thermal images for plane, granular, and fibrous structure coatings on PS foam substrates at different incident angles (0, 20, and 40º) under 1 sun after reaching thermal equilibrium. ΔT is the surface average temperature difference between 0 and 40º incident angles of each coating.

3.7 Chapter summary

In summary, a PPy-DA nanofiber light-trapping coating method was developed for efficient solar vapour generation. This nanofiber coating can be directly synthesized without using any prepared fibrous template as the substrate, and easily coated on various substrates by ultrasonic spray coating at room temperature rapidly (30 min reaction time). In addition, the surface structure can be further tuned by simply using APS as oxidant to obtain a granular structure, or using SDBS as surfactant to obtain plane-fibrous or

plane-granular composite structures. Stronger oxidant (APS) can turn the fibrous structure (by $FeCl_3$) into granular structure due to the instant crosslinks. The composite structures (plane-fibrous/plane-granular) are due to that aqueous oxidant solution preferentially extracts hydrophilic components and leaves part of the hydrophobic pyrrole self-polymerize covering the fibrous or granular structures below. This nanofiber coating has excellent water spreading for water transportation, meaning this coating can act the water transport layer as well. The special light-trapping design at the nanoscale promotes multiple reflections and significantly improves the solar absorption at different incidence angles across the full solar spectrum. The highest solar absorptance achieved 97.73%. This PPy-DA nanofibrous coating shows great potential for solar vapour generation and other applications based on PPy materials, especially for those requiring certain surface morphology.

Chapter 4
Interfacial evaporator with salt back diffusion

4.1 Introduction

Solar vapour generation is a mass and heat transfer process occurring at the air-water interface, it is more efficient to localize the heat at the interface [42, 99, 103]. Based on this, a typical solar vapour generator tends to float on the water surface and has the following features to enhance vapour generation: an efficient solar absorbing top layer to convert solar irradiation into heat; a thermal management design to minimize heat loss to the bulk water below; and a well-designed water transport system to pump the water onto the top layer [58, 73, 75, 101, 111, 128].

In this chapter, polypyrrole-dopamine light-trapping coating was coated on the polystyrene foam and introduced a cross-shaped water transport tape, assembling an interfacial solar evaporator, which floats at the air-water interface (Figure 4.1). The evaporation performance of the plane PPy and granular PPy-DA coatings were also tested for comparison with the fibrous PPy-DA coating.

This evaporator achieves a highest solar-to-thermal conversion efficiency of 95.8% at the evaporation rate of 1.385 $kg \cdot m^{-2} \cdot h^{-1}$ under 1 sun. When applied on salt water, salt accumulates on four separate parts of the surface, which prevents salt from covering the central area with the highest evaporation rate and achieves self-cleaning of salt in absence of solar irradiation.

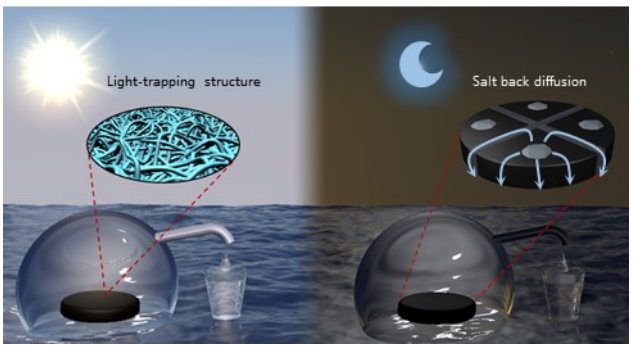

Figure 4.1 Schematic view of solar vapour generation in the sun and salt back diffusion in the dark of the interfacial evaporator coated by polypyrrole-dopamine nanofiber.

4.2 Solar evaporator assembly

Based on the PPy-DA nanofiber photothermal material in the previous chapter, a solar interfacial evaporator was made by coating on a polystyrene (PS) foam (4.8 cm in diameter and 1.5 cm in thickness). Although the fibrous PPy-DA coating has good water spreading due to its porous structure, this thin coating cannot supply enough water to keep up with the solar evaporation rate on a large surface. Hence, a cross-shaped water transport tape was applied, which consists of two separate stripe tapes vertically stacking together on the evaporation surface. Each type (7 cm × 3 mm) was made from airlaid paper, which has excellent water absorption, coated by fibrous PPy-DA in the same way (Figure 4.2).

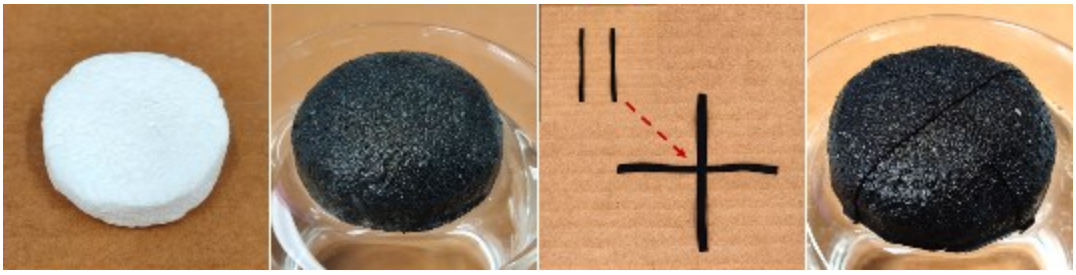

Figure 4.2 Solar evaporator assembly.

By introducing the tapes, the evaporation surface coated by fibrous PPy-DA could be wetted completely in 40 s, presenting excellent water supply (Figure 4.3).

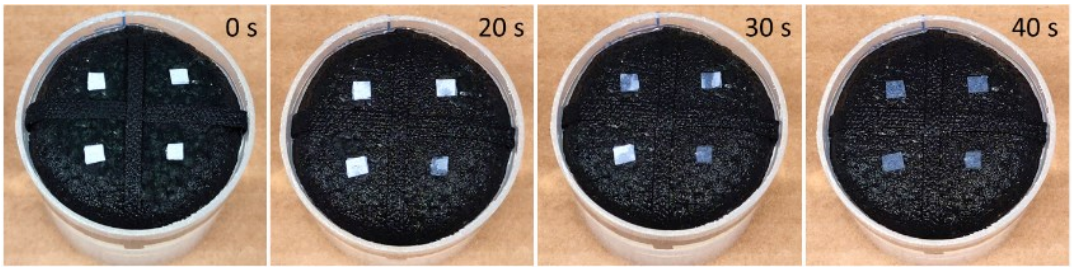

Figure 4.3 Wettability performance of the solar evaporator.

4.3 Energy efficiency calculation

To evaluate the evaporation performance, the solar thermal conversion efficiency in this work was calculated by the following equation [160]:

$$\eta = \frac{m\left[Cp_{water}\left(T - T_0\right) + H_{LV}\right]}{E_{input}} \times 100\% \quad (4\text{-}1)$$

Where m is the evaporation rate ($kg \cdot m^{-2} \cdot h^{-1}$); E_{input} denotes the normal direct solar irradiation input (1000 $W \cdot m^{-2}$); Cp_{water} is water specific heat capacity (4.2 $kJ \cdot kg^{-1} \cdot K^{-1}$ at 1 atm); T and T_0 are the surface average temperature and initial temperature of water respectively; H_{LV} is the water enthalpy of vaporization at the surface equilibrium average temperature (The Engineering ToolBox 2020 Water – Heat of Vaporization: https://www.engineeringtoolbox.com/water-properties-d_1573.html).

4.4 Evaporation of DI water

The evaporation performance of DI water of the evaporator was tested under a solar simulator. The simulated solar light was provided by a xenon arc lamp from a solar simulator (ORIEL® Sol3ATM CLASS AAA SOLAR SIMULATOR) with an optical filter for air mass 1.5 global (AM 1.5 G) standard spectrum (Figure 4.4). The lab environmental temperature was around 20 °C and humidity was around 35%. The mass change was recorded every second by an analytical balance (Discovery DV144C Ohaus Corporation with a sensitivity of 0.1 mg) connecting to a computer for real-time monitoring. In the experiment, the solar steam generator floated on the water surface in a polypropylene beaker. A PS foam was placed between the beaker and the tray of the balance to insulate heat from the bottom.

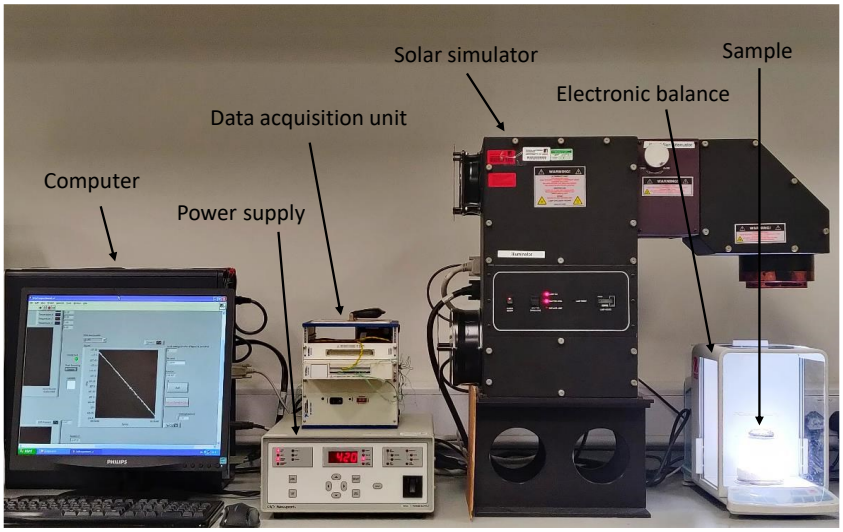

Figure 4.4 Solar evaporation performance test system.

For comparison, the evaporation performance was tested for all the three solar thermal coatings as prepared in the previous chapter in both dark and simulated solar environment with DI water first. In dark evaporation (no light), the evaporation rate of water was only 0.072 $kg \cdot m^{-2} \cdot h^{-1}$ (Figure 4.5). In comparison, the solar evaporators promoted the evaporation performance even in dark. Among them, due to larger specific surface area, the fibrous PPy-DA reached 0.162 $kg \cdot m^{-2} \cdot h^{-1}$, followed by granular PPy-DA (0.157 $kg \cdot m^{-2} \cdot h^{-1}$) and plane PPy (0.144 $kg \cdot m^{-2} \cdot h^{-1}$).

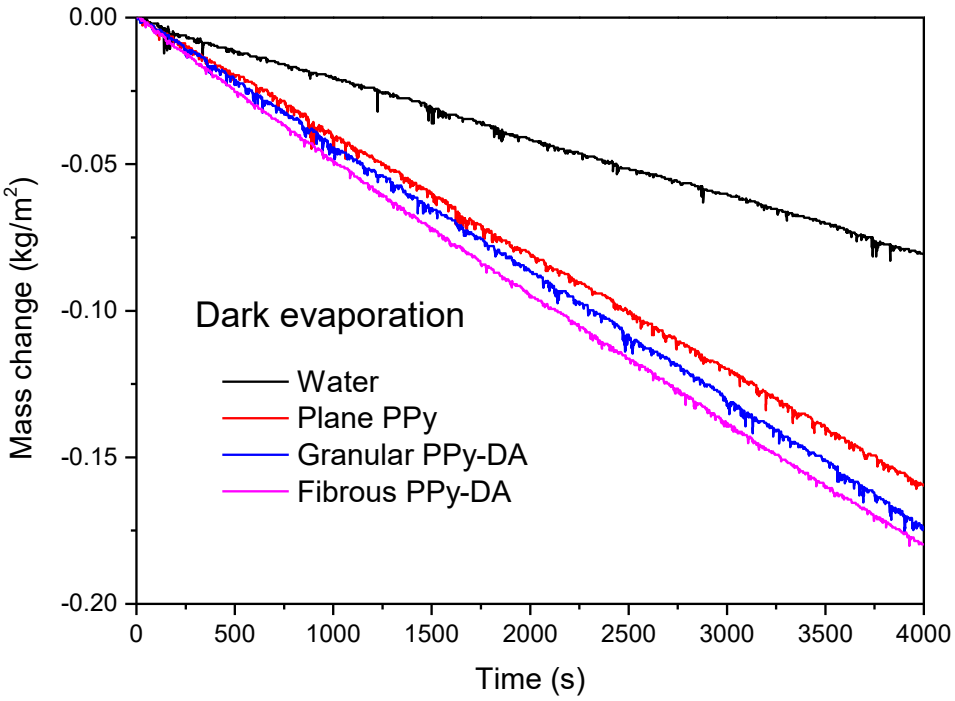

Figure 4.5 Dark evaporation of DI water.

In solar evaporation (Figure 4.6), water evaporation rate reached 0.252 $kg \cdot m^{-2} \cdot h^{-1}$. The evaporators notably improved the evaporation rate. Plane PPy itself has good solar evaporation performance, achieving 1.223 $kg \cdot m^{-2} \cdot h^{-1}$, and the corresponding solar thermal conversion efficiency reached 84.6%. After tuning the surface structure, the efficiency was further improved. Fibrous PPy-DA has the best performance, achieving 1.385 $kg \cdot m^{-2} \cdot h^{-1}$ with the corresponding efficiency of 95.8%, followed by granular PPy-DA (1.326 $kg \cdot m^{-2} \cdot h^{-1}$, 91.7%).

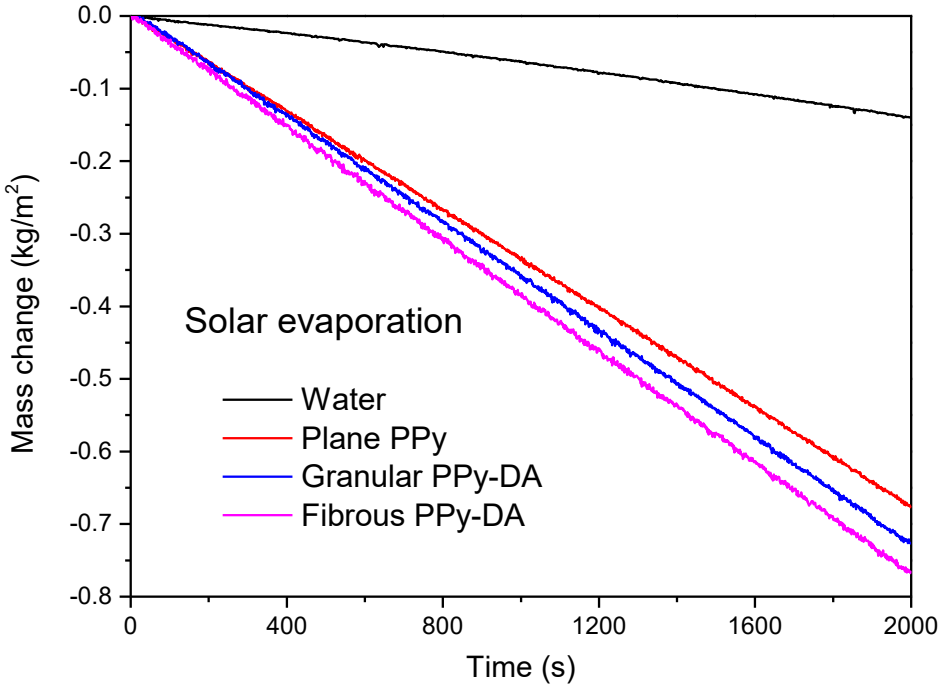

Figure 4.6 Simulated solar evaporation of DI water under 1 sun (1 kW·m^{-2}).

For the fibrous PPy-DA light-trapping coating, with no solar irradiation, the evaporation surface temperature (15.7 °C) was lower than the ambient temperature (Figure 4.7). This temperature difference drives the heat from the environment to transfer to the evaporator to continue the evaporation. When the light was on, the surface temperature soared to ~45 °C in 100 seconds (not surface average temperature, it is a single point temperature at central part by a thermocouple). The temperatures below the evaporating surface 1.5/3.0/4.5 cm slowly increased, and with the depth increasing the temperature increase was slower. This shows the thermal insulating layer well localized the heat on the surface for evaporation. When the light was off, the surface temperature rapidly decreased below ambient temperature again, and the bulk water temperatures below were gradually levelling off. From the thermal image (Figure 4.7), the evaporating surface temperature was not uniform and the central part was hotter. The average surface temperature was 40.3 °C. The highest temperature point reached 47.9 °C and the lowest was 28.0 °C at the edge. From the side view, the temperature decreased from the top (39.7 °C) to the bottom (24.8 °C).

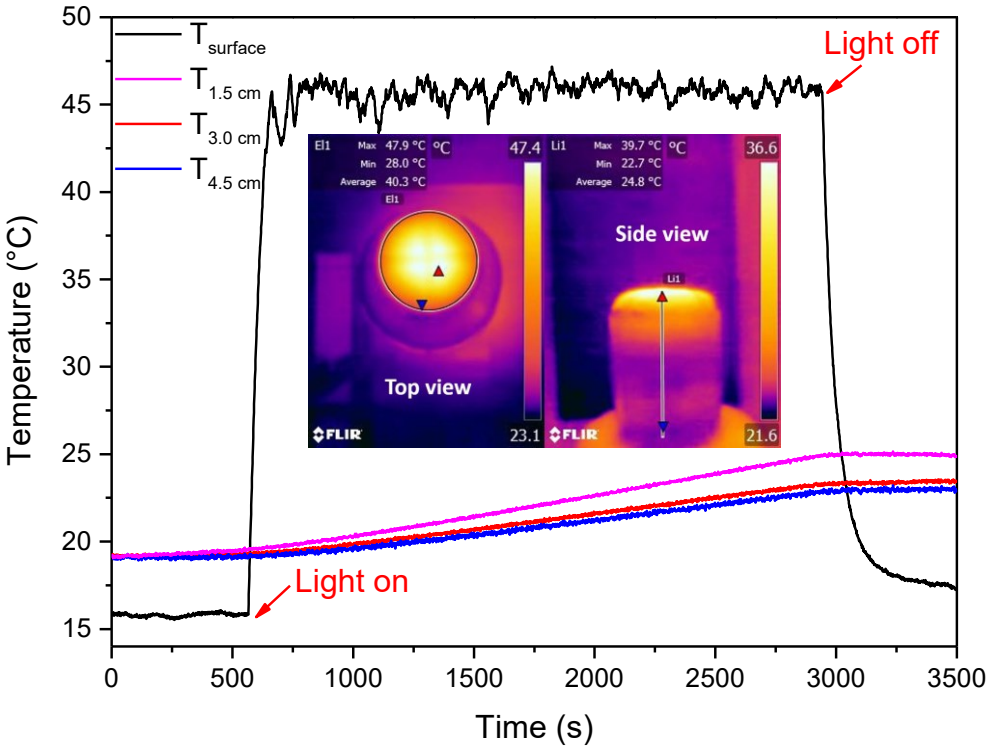

Figure 4.7 Temperature variation at different position through the solar evaporation process under 1 sun ($T_{1.5,\ 3.0\ \text{and}\ 4.5\ \text{cm}}$ mean the temperature at a certain distance below the surface). The thermal images (just before light off) of top and side views were inserted.

The comparison of solar vapour generation performance between recently reported materials and this work is listed in Table 4.1. It should be noted that the solar-to-thermal conversion efficiency depends on not only the solar absorbing material but also the whole evaporation structure and the test environment. Notably, many factors could potentially influence the repeatability of the evaporation results. First of all, the environmental conditions would affect the evaporation rate, including the ambient temperature, ambient humidity, and the flow of the surrounding air. Then the uniformity and stability of the light source, the thermal conductivity of the thermal insulation layer and the bulk water temperature could also affect the results. In addition, the uniformity of photothermal coating would also affect the results by affecting the solar absorptance and water transportation on the evaporation surface.

Table 4.1 Solar vapour generation performance under 1 sun (1 kW/m^2) of reported materials and this work.

Materials	Efficiency	Date
Porous graphene [69]	80%	06.2015
Bi-layered reduced graphene oxide [75]	83%	08.2017
Graphene oxide foam [161]	89%	10.2019
Reduced graphene oxide [54]	89.2%	08.2017
Graphene membranes [76]	90%	07.2018
Polypyrrole-Reinforced N,S-Doping Graphene Foam [162]	90.5%	05.2021
Graphene Oxide–Reduced Graphene Oxide Janus Membrane [163]	91.4%	01.2021
Graphene oxide-functionalized electrospun nanofibrous membrane [164]	94.2%	08.2020
Tailoring polypyrrole-based Janus aerogel [165]	94.7%	07.2021
Graphene/MoO3-x coated porous nickel [166]	95%	06.2021
This work	**95.8%**	**-**
Structured graphene [167]	96.2%	03.2020
3D Graphene/Cellulose Nanocrystals [168]	97.5%	06.2021
Reduced graphene oxide composite aerogels [169]	98.4%	03.2021

The quality of the desalinated water was further tested by using simulated seawater (3.5 wt% NaCl). After solar evaporation, the salt concentrations dramatically decreased and were much lower than both WHO and EPA drinking water standards for all three samples (Figure 4.8).

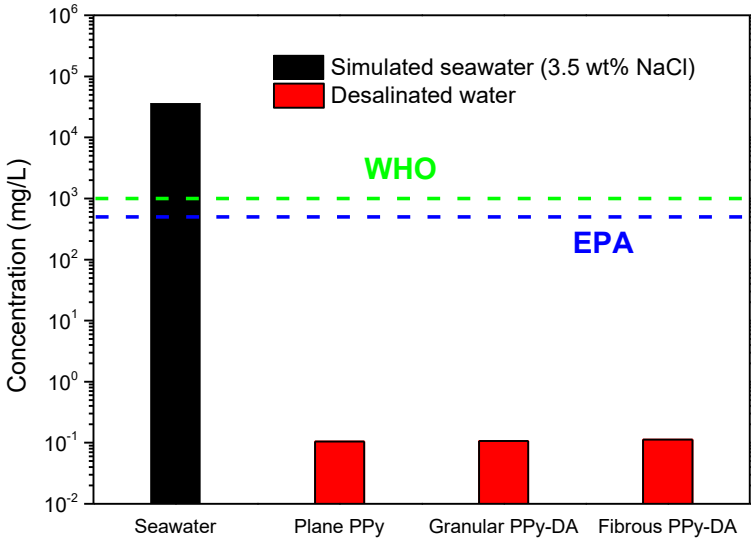

Figure 4.8 Measured salinities before and after solar evaporation.

The solar evaporation of the fibrous PPy-DA coating was repeatedly tested ten times (Figure 4.9), and the evaporation rate was found almost constant, indicating this nanofiber light-trapping coating is satisfactory for long-term solar evaporation.

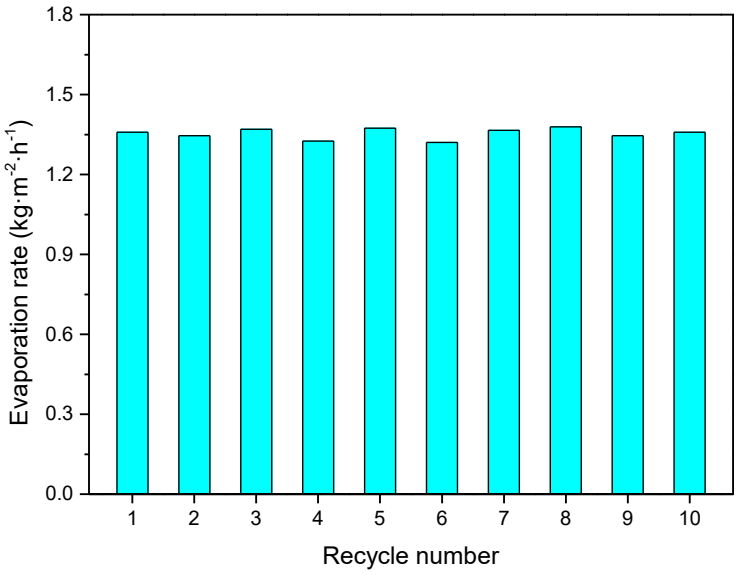

Figure 4.9 Solar evaporation performance over multiple recycles.

To further evaluate the solar evaporation performance under the sunlight in real field environment. The field solar evaporation test was on a sunny day in October in Leeds, UK. As the evaporator is floating on the water surface, it is parallel to the ground. Therefore, the solar power density is tested based on a flat ground, not facing the sunlight, making it lower than vertical irradiation,

as illustrated in the insert in Figure 4.10. During the test, the average solar power density is 361 W/m^2 and the average temperature is 9 °C, humidity is ~70% and wind speed is 4-9 km/h. An easy-to-implement solar evaporation and fresh water collection system was presented, and 4.62 g of fresh water was collected during the test (corresponding to 0.285 kg·m^{-2}·h^{-1}) by a 4.8 cm (diameter) solar evaporator. Lower power density, lower field temperature and the fresh water collection system all slow down the evaporation rate, which makes the evaporation rate much lower than that in a simulated sunlight in the lab.

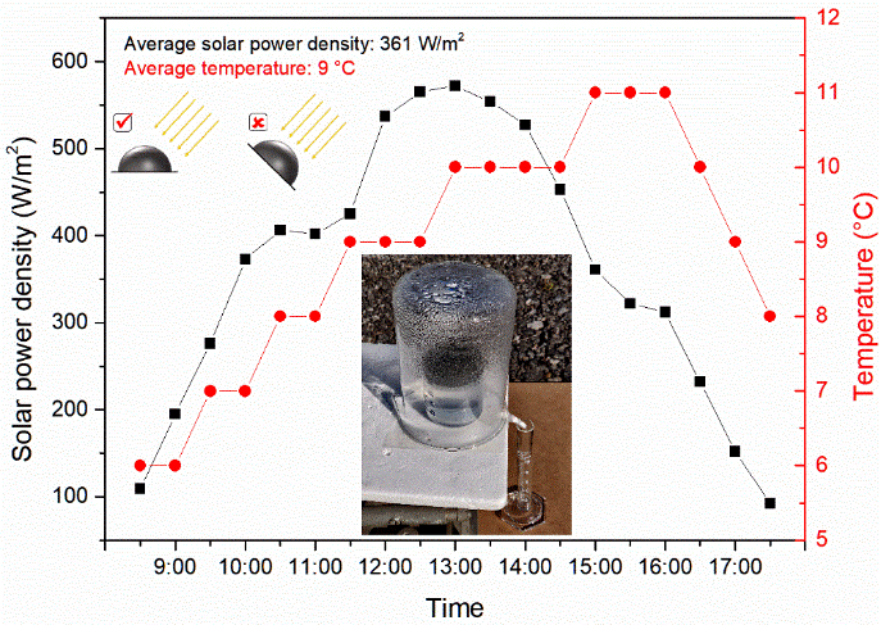

Figure 4.10 Solar power density and temperature variation with time in the field solar evaporation test environment. The insert is a solar evaporation and fresh water collection system. The solar power density test direction illustration is also inserted.

4.5 Evaporation of saline water

In seawater desalination, salt accumulation on the evaporation surface will reflect solar irradiation and cover effective evaporation area, which slows down the evaporation rate. Here, the salt accumulation process was first studied with this interfacial evaporator with simulated salt water (3.5 wt% NaCl) under one sun (1 kW·m^{-2}) for 6 h, and then salt back dissolution process was further tested in dark for 18 h (Figure 4.11). The total irradiation is 6 kW·h·m^{-2}, which is much greater than the US annual average daily solar irradiation (~4.5 kW·h·m^{-2}) [170]. Due to the cross-shaped water transport tapes, salt

accumulates on four separate parts of the surface, which prevents salt from covering the hottest area in the centre (i.e. the highest evaporation rate area).

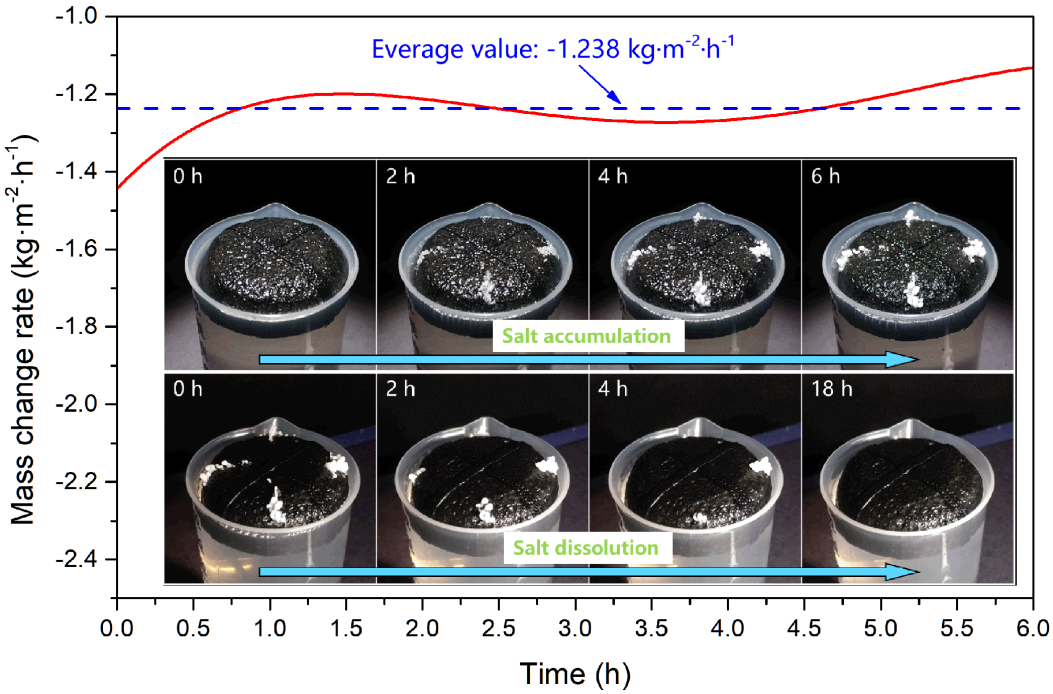

Figure 4.11 Mass change rate on salt water (3.5 wt% NaCl) over 6 h irradiation under one sun. Inserts are the salt accumulation process under one sun over 6 h and salt dissolution process in dark over 18 h (24 h in total).

The evaporation performance was further tested to take the first derivative to evaluate the evaporation rate of salt water (Figure 4.12). The mass change curve is not smooth, and in order to take the first derivative of the mass change curve to obtain the mass change rate curve, a fifth-order polynomial fitted curve was used (R-square: 0.9999), which was then used to take the first derivative. To eliminate the liquid level impact, the salt water level was kept constant by connecting a U-tube salt water supply system to the bottom of the beaker to supply salt water manually by adjusting the salt water level on the other side.

The evaporation rate decreased from the beginning and then fluctuated around 1.238 $kg \cdot m^{-2} \cdot h^{-1}$ in 6 hours (Figure 4.11). It should be noted that, the reason why the evaporation rate of salt water is lower than that of DI water is due to not only the influence of salt accumulation but also the decrease of salt water vapour pressure (Raoult's Law). The salt dissolution process also benefits from the separated salt accumulation, because salt back diffusion to

the bulk water can utilize the whole evaporation surface, realizing self-cleaning of salt in absence of solar irradiation.

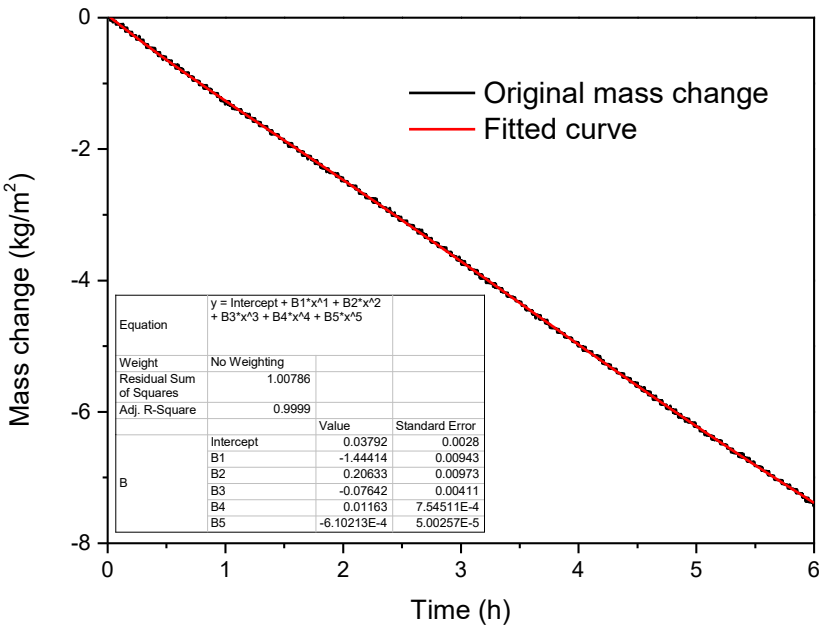

Figure 4.12 Mass change on salt water (3.5 wt% NaCl) over 6 h under one sun and its fifth order polynomial fitted curve.

4.6 Chapter summary

Here, an interfacial solar evaporator was developed that is coated by polypyrrole-dopamine light-trapping nanofibres. The water transport layer is integrated into the solar absorbing layer due to its excellent water transportation. A cross-shaped water transport tape is introduced to ensure enough water supply to keep up with solar evaporation on a large surface. This evaporator achieves the highest solar-to-thermal conversion efficiency of 95.8% at the evaporation rate of 1.385 $kg \cdot m^{-2} \cdot h^{-1}$ under 1 sun, and achieves 0.162 $kg \cdot m^{-2} \cdot h^{-1}$ in dark evaporation. When applied on salt water, salt accumulates on four separate parts of the surface, which prevents salt from covering the central area with the highest evaporation rate and achieves self-cleaning of salt in absence of solar irradiation. The evaporated water quality over satisfies the WHO and EPA drinking standards.

Chapter 5
Double-sided evaporation umbrella evaporator

5.1 Introduction

A typical interfacial evaporator (IE) floats at the air-water interface with a thermal insulation layer below to localize the heat on the evaporation surface, which makes it single-sided evaporation (Figure 5.1). At the same time, the water is usually supplied from the edge on the IE, which would accumulate salts at the centre part. The salts would hinder the evaporation.

In this chapter, a novel umbrella evaporator (UE) is demonstrated, which double-sided evaporation by discarding the thermal insulation layer beneath, and improve the efficiencies of both vapour production and salt collection concurrently (Figure 5.1). And benefiting from the central seawater supply, salts could precipitate at the edge and falls down for harvesting (in Chapter 6). In this chapter, the evaporation performance of the IE and the UE was compared by experiments in the same test environment using deionized water, and the structural advantages of the UE over the IE was analysed by numeric simulations. And finally, based on the simulations, the factors affecting the energy efficiency are discussed.

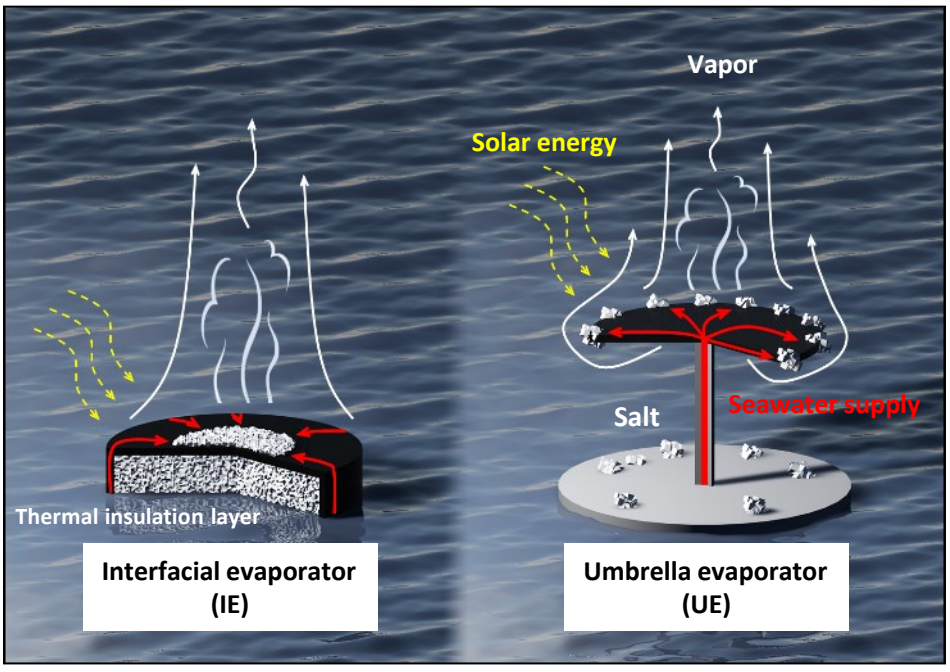

Figure 5.1 Schematic illustration of the IE and UE.

5.2 Experiment comparison of evaporation

5.2.1 Solar evaporators assembly

Based on the coating method in Chapter 3, plane polypyrrole was coated on a filter paper by ultrasonic spray coating to make the black evaporation surfaces. And the coated filter paper was further made into an IE and a UE (Figure 5.2).

Figure 5.2 Assembly of the IE and UE. (a) Assembly of the IE. (b) Assembly of the UE.

The final evaporators for the comparison test are shown in Figure 5.3. To minimize the solar absorption of other parts except for the solar evaporation surface, the main body was surrounded by foils. The solar evaporation surface diameter for both IE and UE is 3 cm. For the IE, a polystyrene foam (1.5 cm in thickness and 5 cm in diameter) was applied to act as the thermal insulation layer. For the UE, a polyester pillar (0.8 cm in diameter) was applied for water transportation. The evaporation surface was directly placed on the top of the pillar and attached by the surface tension of water.

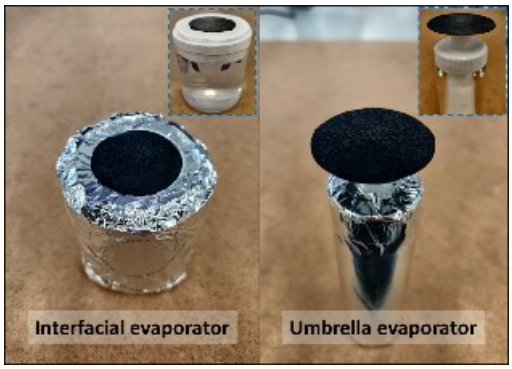

Figure 5.3 The IE and UE used for the evaporation test.

The water supply in the polyester pillar is driven by capillary force of the fibers (Figure 5.4).

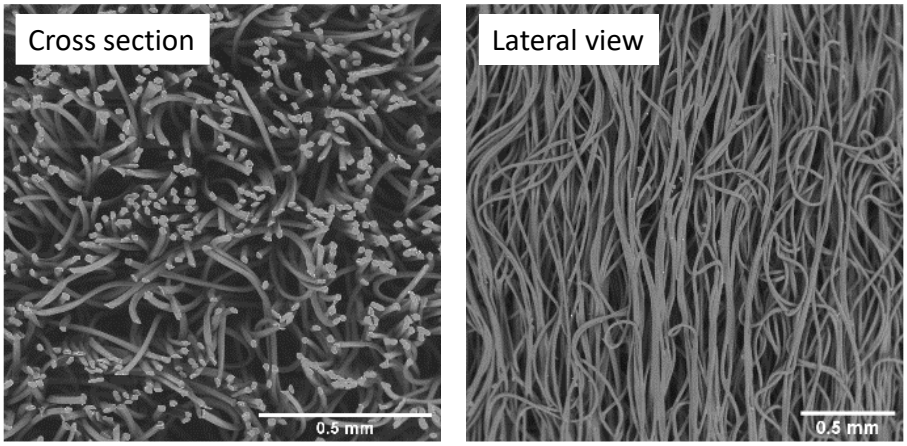

Figure 5.4 Cross section and the lateral view of the polyester pillar.

The capillary pressure in the porous surface was calculated as below:

$$P_c = \frac{2\sigma}{R_c}\cos\theta \tag{5-1}$$

Here P_c is the capillary pressure, σ is the water surface tension (0.072 N/m at room temperature), R_c is the capillary radius (25 μm), θ is the contact angle (can be roughly regarded as 0°) [171]. Based on the above, the capillary pressure is roughly estimated to be 5.76 kPa.

5.2.2 Solar evaporation comparison

In solar evaporation, the UE has a much lower surface average temperature (33.8 ºC) than IE (40.5 ºC) (Figure 5.5), which is caused by a higher evaporation rate (1.25 vs 1.10 $kg \cdot m^{-2} \cdot h^{-1}$, a 13.6% increase). Lower surface temperature would also help reduce heat loss by decreasing the temperature difference from the environment, making a higher energy efficiency of the UE (85.8%) than the IE (75.8%).

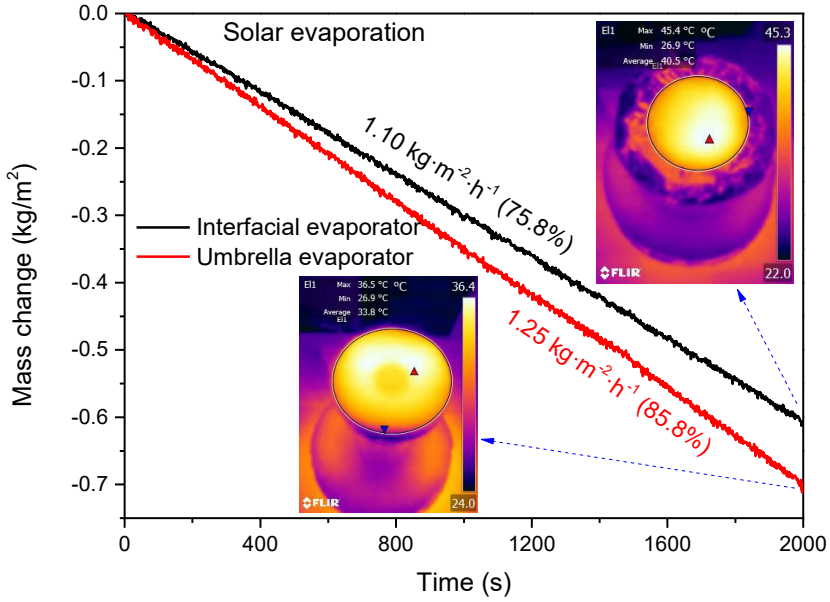

Figure 5.5 Solar evaporation of the IE and UE.

As the UE has a lower surface temperature and a smaller heat transfer area by the pillar to the bulk water, its surface water temperature increased only 0.95 ºC in 2000 s, by contrast, IE increased more rapidly (1.75 ºC), indicating more heat loss to the bulk water (Figure 5.6).

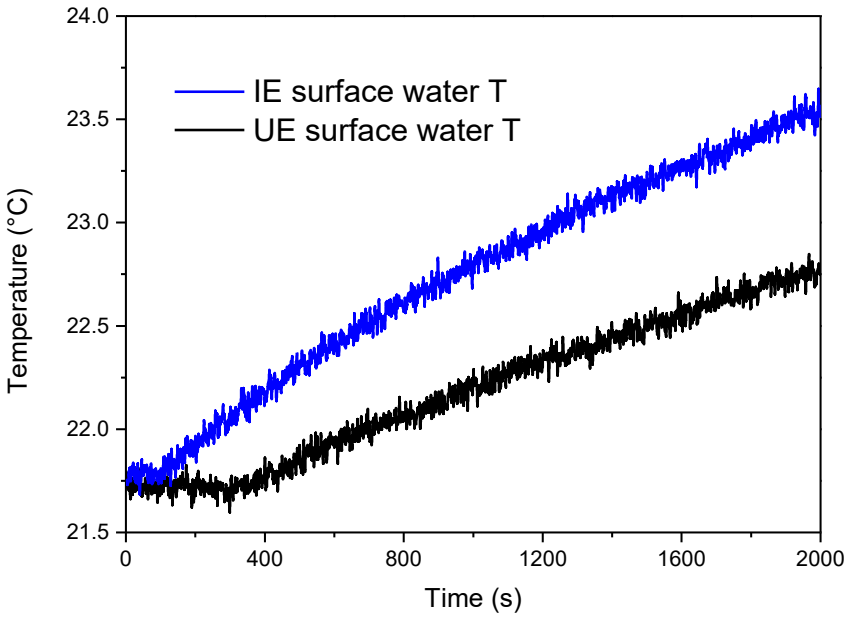

Figure 5.6 Surface water temperature in solar evaporation.

The evaporation performance comparison of different reported evaporators is listed in Table 5.1. It shall be noted that the evaporation rate in this work only comes from the surface evaporation without any side wall evaporation. At the

same time, the theoretical maximum evaporation rate should be around 1.47 $kg \cdot m^{-2} \cdot h^{-1}$ under 1 sun based on the law of conservation of energy.[112] Evaporation rate comparison of different evaporators in Table 5.1 requires great care especially for those values beyond this upper limit. A range of parameters including heat source, light source distance, sample size, water gap, aperture, light intensity calibration, as well as the evaporation conditions (e.g. temperature, humidity and wind speed), will influence the evaporators' performance. Considering all these factors, both the evaporation rate and energy conversion efficiency obtained in this work are highly impressive. More importantly, the comparisons of the two designs under the same conditions provide convincing evidence for the advantages of umbrella structure over the IEs.

Table 5.1 Evaporation performance under 1 sun (1 kW/m^2) of different reported evaporators.

Evaporators	Photothermal material	Solar absorptance	Evaporation rate (kg·m^{-2}·h^{-1})	Efficiency
IE[42]	Exfoliated graphite	97%	1.2	64%
IE[69]	Porous graphene	98%	1.5	80%
IE[75]	Reduced graphene oxide	-	1.31	83%
IE[172]	Carbon black graphene oxide	99%	1.27	87.5%
IE[31]	Polypyrrole gel	-	3.2	94%
IE[145]	Multilayer polypyrrole	95.33%	1.38	92%
IE[173]	Carbon black polypyrrole	95%	1.68	91.5%
IE[174]	Polypyrrole	92.6%	1.35	86.6%
3D evaporator[128]	Carbon nanotubes	-	2.63	96%
3D IE[167]	Structure graphene	95%	1.5	96.2%
3D evaporator[175]	Carbon foam	93%	10.9	-
Single-sided UE[130]	Carbon nanotube	96.5%	1.42	81.2%
Airing evaporator[176]	Carbon black	97%	-	87%
Synthetic tree[132]	Polypyrrole	97%	2.03	75%
Non-contact evaporator[177]	Almeco	95%	0.62	43%
Single-sided UE[178]	MoS_2	98.4%	1.38	84.5%
This work	Polypyrrole	96.2%	1.25	85.8%

5.2.3 Dark evaporation comparison

In dark evaporation (no light), the average temperature of both surfaces (IE 20.4 ºC and UE 19.5 ºC) is lower than the environment (21.8 ºC), indicating that the surfaces could obtain energy from the environment, which drives the evaporation (Figure 5.7). By contrast, in solar evaporation, a hotter surface cannot gain energy from the environment by heat transfer. Due to double-sided heat gaining from the environment, UE has a higher surface average temperature than IE. Combining with the double-sided vapour diffusion, the UE has an remarkable 72% higher evaporation rate (0.31 $kg \cdot m^{-2} \cdot h^{-1}$) than the IE (0.18 $kg \cdot m^{-2} \cdot h^{-1}$). Therefore, UE has a better SVG performance in both solar and dark evaporation.

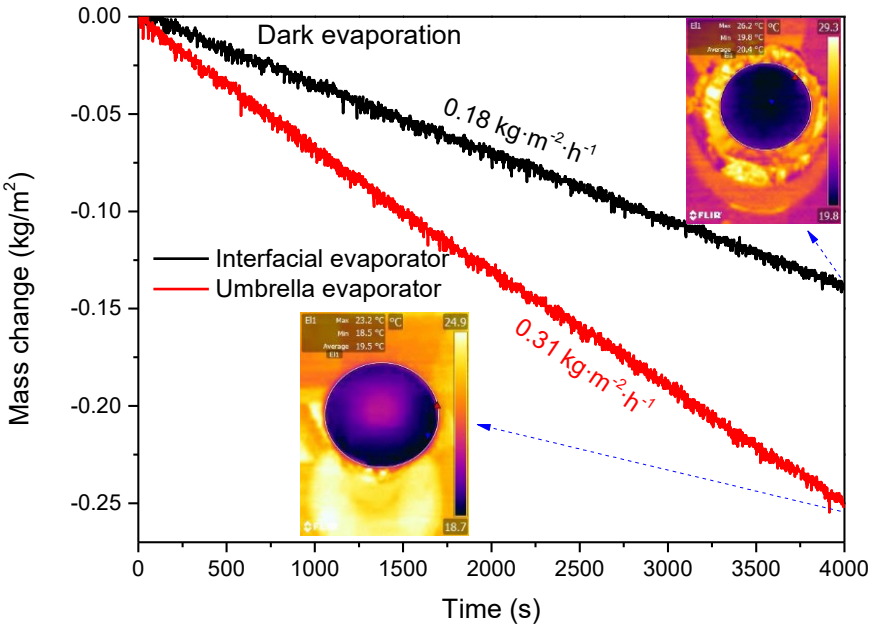

Figure 5.7 Dark evaporation of the IE and UE.

5.3 Evaporation simulation setup

To better understand the UE structural advantages in solar evaporation, the evaporation process was simulated by a commercial finite element software COMSOL Multiphysics 5.3. The model includes the solar evaporator and the air above. Here a 2 dimensional axial symmetry (2D AS) steady state model was used to simulate the evaporation process.

5.3.1 Model description and parameters

The model consists of three domains: air, porous media and polystyrene (PS) foam solid (Figure 5.8). The water supply to the evaporating surface is assumed adequate in the porous media by capillary force, as a result, the channels inside are filled with water. Therefore, water evaporation in the porous media can be regarded as happening at the surface for simplification. In consequence, the vapour concentration in the porous media was set uniform at saturation to simulate surface evaporation. The heat capacity and thermal conductivity of the porous media are calculated by the mixed percentage of filter paper and water.

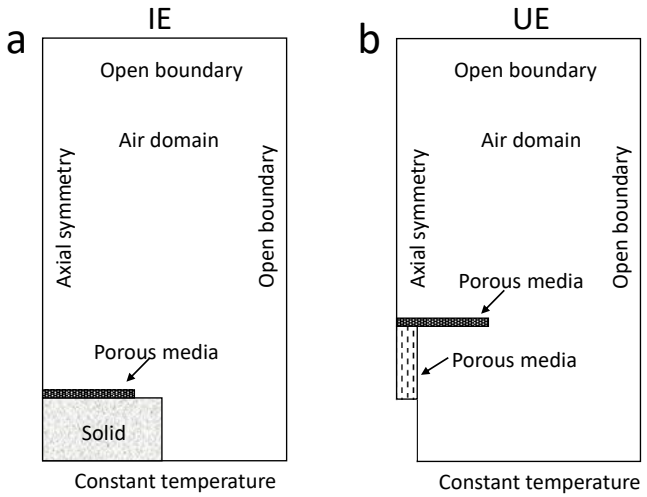

Figure 5.8 Schematic diagram of the computed domains and boundary conditions. (a) IE domains and boundary conditions. (b) UE domains and boundary conditions.

Three physical processes in the model were used: laminar flow, heat transfer and vapour diffusion. In which domains each process applies are listed in Table 5.2.

Table 5.2 The matching relation between physical processes and computed domains.

	Air domain	Porous media	PS foam solid
Laminar flow	Yes	No	No
Vapour diffusion	Yes	Yes	No
Heat transfer	Yes	Yes	Yes

Laminar flow, heat transfer and vapour diffusion process are coupled mutually (Figure 5.9). Heat transfer provides temperature (T) to laminar flow and

vapour diffusion to calculate viscosity, density and diffusion coefficient respectively, which are functions of temperature. Laminar flow provides velocity magnitude to heat transfer and vapour diffusion. Vapour diffusion provides heat source Q (enthalpy of vaporization) to heat transfer in the porous media.

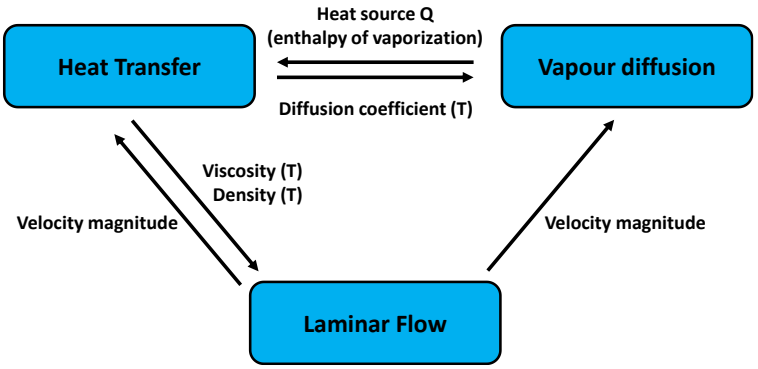

Figure 5.9 Coupling relation of heat transfer, laminar flow and vapour diffusion.

The major assumptions in the modelling are summarized as below. As the temperature change was less than 20 ºC in the system, the heat capacity, thermal conductivity, density, heat transfer coefficient and specific heat capacity of the solid porous media was regarded constant. The ambient temperature and humidity was set uniform and constant. The vapour concentration was always assumed saturated at the interface between the evaporation surface and the air domain. The water supply was always sufficient for evaporation.

These assumptions would not affect the results much but greatly simply the simulation. Higher ambient temperature and lower humidity would promote the evaporation by increasing the saturated vapour pressure and increasing the vapour concentration difference between the sample surface and the environment respectively. The constant thermophysical properties adopted in the modelling would slightly affect the heat transfer process as the sample temperature changed less than 20 ºC. In addition, the potential heat sources would also pump additional energy into the system to promote the evaporation, such as the heat dissipation from the computer and the solar simulator, and the heat from unabsorbed solar irradiation, which should be minimized.

The key parameters in this simulation are listed in Table 5.3.

Table 5.3 Key parameters in the simulation.

	IE	UE
Ambient temperature	21.8 ºC	
Ambient relative humidity	0.5	
Air domain height	16 cm	
Air domain radius	6 cm	
Surface emissivity (surface absorptance)	0.962*	
Evaporation surface porosity	0.806*	
Bulk water surface temperature	22.7 ºC	22.3 ºC
PS foam height	1.5 cm	-
PS foam radius	2.5 cm	-
Polyester pillar porosity	-	0.885*
Polyester pillar radius	-	0.4 cm
Polyester pillar length	-	2 cm

The data (marked *) in Table 5.3 is obtained by the following methods.

The surface emissivity (surface absorptance) is calculated by the following equations:

$$A_{solar} = 1 - R_{solar} - T_{solar} \tag{5-2}$$

$$R_{solar} = \frac{\int R \cdot I_{solar} d\lambda}{\int I_{solar} d\lambda} \tag{5-3}$$

$$T_{solar} = \frac{\int T \cdot I_{solar} d\lambda}{\int I_{solar} d\lambda} \tag{5-4}$$

Where A_{solar} is solar energy absorption across the standard solar spectral irradiance (AM 1.5G), R is reflectance and T is transmittance of the coating (Figure 5.10). I_{solar} is solar spectral irradiance ($W \cdot m^{-2} \cdot nm^{-1}$) and λ is the wavelength (nm). By calculation, the surface absorptance is 0.962.

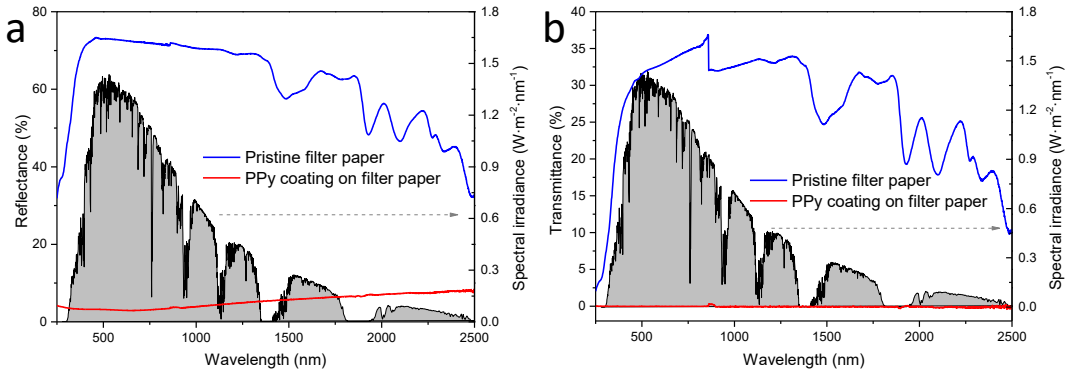

Figure 5.10 Diffuse reflectance spectra and transmittance spectra of the pristine filter and PPy coating on filter paper. (a) Diffuse reflectance spectra. (b) Transmittance spectra. The standard solar spectral irradiance (AM 1.5 G) serves as a background reference.

Evaporation surface porosity is determined by the following method. The evaporation surface (3 cm in diameter and 0.016 cm in thickness) was first soaked in DI water for 1 h and then placed on the polyester pillar inserted in water. The whole structure was held for 12 h to make the evaporation and capillary-driven water supply by the pillar balanced. The pores inside would be filled with water. The porosity is calculated by the following equations.

$$V_{water} = \frac{M_{paper+water} - M_{paper}}{\rho_{water}} \tag{5-5}$$

$$V_{paper} = \pi r_{paper}^2 h_{paper} \tag{5-6}$$

$$Porosity = {V_{water}}/{V_{paper}} \tag{5-7}$$

Where V_{water} is the water volume, $M_{paper+water}$ is the weight of the filter paper saturated with water after holding for 12 h, M_{paper} is the weight of the dry filter paper, and ρ_{water} is the water density (1 kg/m^3). V_{paper} is the filter paper volume, r_{paper} is the radius of the filter paper (1.5 cm), h_{paper} is the thickness of the filter paper (0.016 cm). By calculation, the evaporation surface porosity is 0.806.

Polyester pillar porosity is calculated in a similar way and equals 0.885.

The material properties of water and air derive from COMSOL 5.3 built-in material library. The properties of the filter paper cellulose fibre, PS foam and polyester pillar fibre are listed in Table 5.4.

Table 5.4 Material properties.

	Filter paper fiber	PS foam	Polyester pillar fiber
Density ($kg \cdot m^{-3}$)	1500	20	1380
Heat transfer coefficient ($W \cdot m^{-1} \cdot K^{-1}$)	0.04	0.035	0.05
Specific heat capacity ($J \cdot kg^{-1} \cdot K^{-1}$)	1107	1450	987

5.3.2 Model equations

The evaporation system simulation was calculated by solving the following equations.

For laminar flow:

$$\rho \frac{\partial \mathbf{u}}{\partial t} + \rho \mathbf{u} \cdot \nabla (\mathbf{u}) = -\nabla p + \nabla \cdot \left(\mu \left(\nabla \mathbf{u} + \nabla \mathbf{u}^{\mathrm{T}} \right) \right) + \rho g \tag{5-8}$$

$$\nabla \cdot (\mathbf{u}) = 0 \tag{5-9}$$

Where **u** is the velocity of fluid, ρ is density which is a function of temperature and pressure (the built-in functions in the software were used), μ is viscosity (function of temperature and the built-in functions were used), g is the gravitational acceleration constant (9.81 m/s^2).

For vapour diffusion:

$$\frac{\partial c}{\partial t} - D \nabla^2 c + \mathbf{u} \cdot \nabla c = R \tag{5-10}$$

Where c is the water vapour concentration, D is the corrected diffusion coefficient of vapour. R the reaction rate (i.e. evaporation rate).

$$D = D\_cf \times D_L \tag{5-11}$$

$$D_L = 4.7931 \times 10^{-5} \times \left(\frac{T^{1.9}}{p} \right) \tag{5-12}$$

$$R = K\_evap \times \left(c\_sat - c \right) \tag{5-13}$$

$$c\_sat = \frac{p_{sat}\left(T\right)}{RT} \tag{5-14}$$

Where *D_cf* is the diffusion coefficient correction factor, D_L is water vapour diffusion coefficient in the air [179]. *K_evap* (1/s) is evaporation rate coefficient. To simulate the saturation state of the vapour in the porous media, a large enough value (1000 1/s) was given to *K_evap*, making the vapour concentration in the porous media is uniform at saturation. *c_sat* is the saturation concentration, $p_{sat}(T)$ is the saturation pressure at certain *T*. *R* is ideal gas constant (8.314 $J \cdot mol^{-1} \cdot K^{-1}$). The relative humidity (RH) is calculated as below:

$$RH = \frac{c}{c_{sat}} \tag{5-15}$$

For heat transfer:

$$\rho C_p \frac{\partial T}{\partial t} + \rho C_p \mathbf{u} \cdot \nabla T - k \nabla^2 T = Q \tag{5-16}$$

Where *T* is temperature, C_p is heat capacity at constant pressure, *k* is heat conductivity coefficient. *Q* is a heat source as below:

$$Q = -R \times H\_evap \tag{5-17}$$

$$H\_evap = 45000 - 42.95 \times \left(T - 273 \right) \tag{5-18}$$

Where *H_evap* (J/mol) is the enthalpy of vaporization for water [180].

For heat radiation:

$$q = \varepsilon A \left(G - J \right) \tag{5-19}$$

$$J = \sigma \left(T^4 - T_{amb}^4 \right) \tag{5-20}$$

Where *q* is the radiation heat, *ε* is the surface emissivity (surface absorptance), *A* is the radiation surface area, *G* is the solar irradiation input (1000 $W \cdot m^{-2}$). *J* is the surface radiation, *σ* is the Stefan-Boltzmann constant (5.6704×10^{-8} $W \cdot m^{-2} \cdot K^{-4}$), T_{amb} is the ambient temperature.

5.3.3 Boundary and initial conditions

The boundary conditions are also shown in Figure 5.8. Top and right sides are open boundaries (ambient temperature and ambient relative humidity), meaning heat, air and vapour can freely flow in and out. In heat transfer process, the bottom boundary is constant at 20 °C to simulate water surface below. For laminar flow and vapour diffusions processes, the bottom boundaries in their own calculating domains are set as walls, meaning no flow and no vapour flux can go through the bottoms walls.

As for initial conditions, the whole model was at ambient temperature and under ambient pressure. In air domain, ambient relative humidity was used. In porous media domain, relative humidity was 1 (vapour concentration reached saturation). The initial velocity field was zero for laminar flow, and the following flow was caused by air density difference.

5.3.4 Mesh conditions

The mesh conditions of the IE and UE are shown in Figure 5.11. For the IE case, there are 30503 cells and 1106 boundaries in the mesh. For the UE case, there are 31023 cells and 1073 boundaries. Mesh is refined at the corners and boundaries. The dependence of model mesh size is also examined by evaporator surface temperature distribution using the original and refined mesh cases (Figure 5.12). As the original and refined curves overlaps together, the influence of mesh size is negligible. There is slight difference observed when the mesh is further largely roughened.

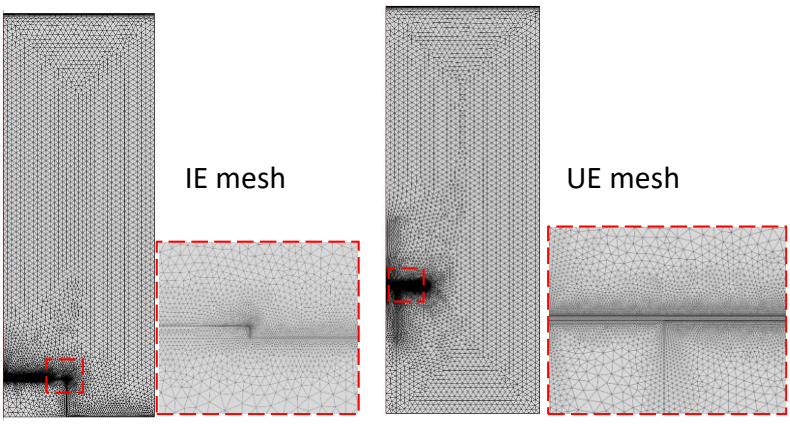

Figure 5.11 Mesh conditions of the models.

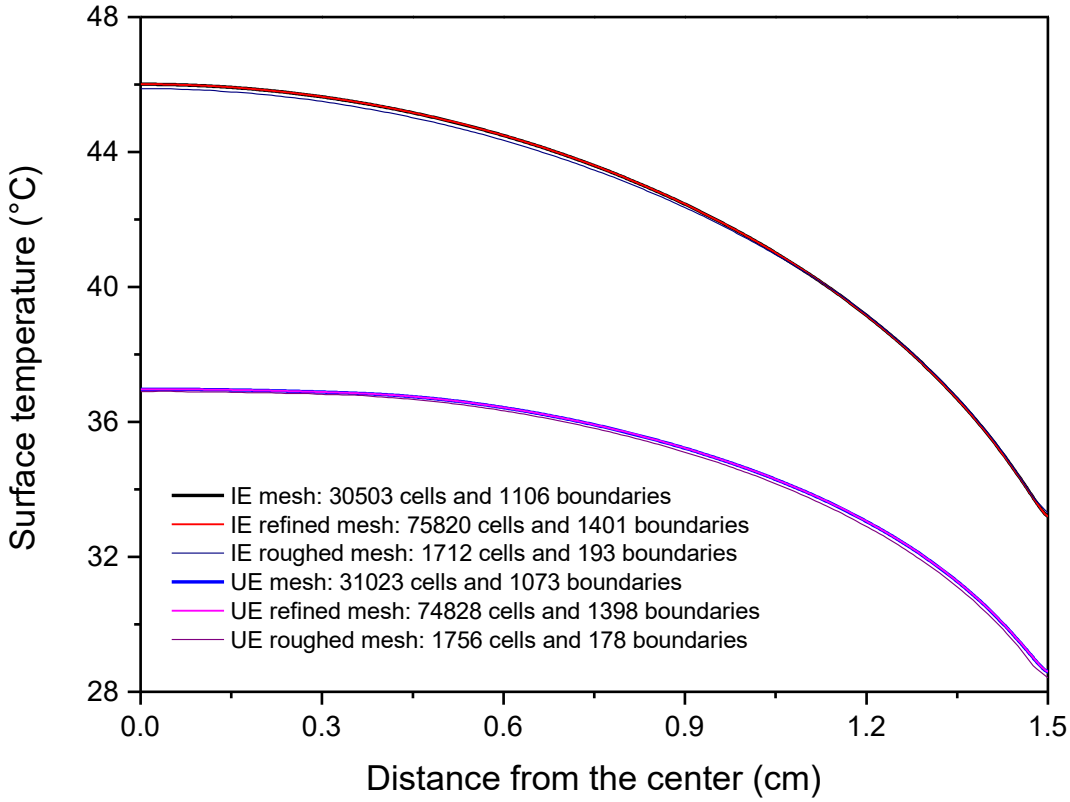

Figure 5.12 Dependence of mesh size by surface temperature distribution using three mesh cases.

5.3.5 Simulation validation

Laminar flow was applied to simulate the moist air. However, laminar flow cannot exactly reproduce the air turbulence flow in real experiments due to the air disturbance under real experimental conditions. The effect of this turbulence flow mainly reflects in diffusion coefficient increase of the water vapour in air. For simplification, a diffusion coefficient correction factor (*D_cf*) was introduced to simulate the effect of air turbulence flow. The *D_cf* was set as 1.9 and 1.8 respectively for the IE and UE to make the surface average temperature equal to the experiment values (Table 5.5). Then the evaporation rate was used to evaluate the model accuracy. The simulation evaporation rates are very close to the experiment rates for both IE and UE, leading to a very high accuracy (93.5% for IE and 91.1% for UE).

Table 5.5 Simulation and experiment results comparisons.

	IE	UE
Diffusion coefficient correction factor (*D_cf*)	1.9	1.8
Simulation surface average temperature (ºC)	40.5	33.8
Experiment surface average temperature (ºC)	40.5	33.8
Simulation evaporation rate (g/s)	2.02×10^{-4}	2.24×10^{-4}
Experiment evaporation rate (g/s)	2.16×10^{-4}	2.46×10^{-4}
Accuracy (Simulation/Experiment)	**93.5%**	**91.1%**

5.4 Results of evaporation simulation comparison

The velocity fields of the IE and the UE are similar, air converges from the periphery over the evaporation surface and then flows up carrying vapour, caused by the density decrease by the solar evaporator heating (Figure 5.13a, b). The temperature of the IE is obviously higher than UE, with the surface central part being the highest for both cases (Figure 5.13c, d). The surface temperature is far from the boiling point. That is the reason why it is supported to name this process “solar vapour generation” instead of “solar steam generation” [58]. Most of all, the UE vapour concentration and relative humidity fields differ a lot from the IE (Figure 5.13e-h). Both sides of the UE surface can evaporate, doubling the mass transfer area. Better mass transfer condition leads to a higher evaporation rate and a lower surface temperature, which increases the energy efficiency.

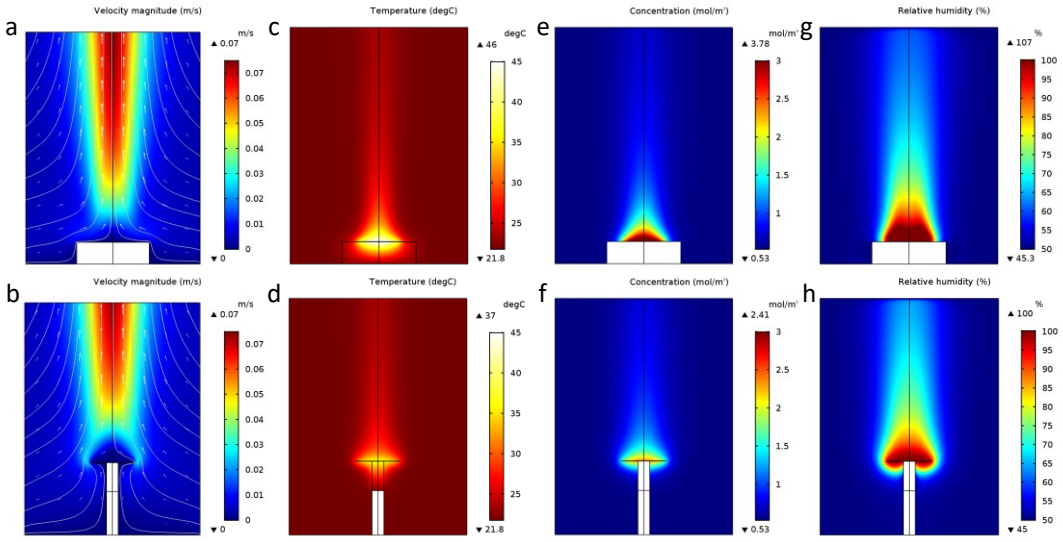

Figure 5.13 Solar evaporation velocity, temperature and relative humidity fields by simulation. (a,b) IE and UE velocity fields. (c,d) IE and UE temperature fields. (e,f) IE and UE vapor concentration fields. (g,h) IE and UE relative humidity fields.

A thermal insulation layer under the UE surface would localize the heat on the surface but hinder the back evaporation, decreasing the overall evaporation rate, which is verified by the following simulation. Figure 5.14 shows the single-sided UE with a thermal insulation layer beneath. There is no essential difference between the single-sided evaporation UE and the IE. Due to the thermal insulation layer, its surface average temperature reaches 38.6 ºC, which is much higher than the double-sided evaporation UE. Its evaporation rate is 2.02×10^{-4} g/s, which is almost equal to the IE and much lower than the double-sided UE (2.24×10^{-4} g/s in Table 5.5). Therefore, double-sided evaporation of the UE is the key factor to surpass the single-sided IE in evaporation performance.

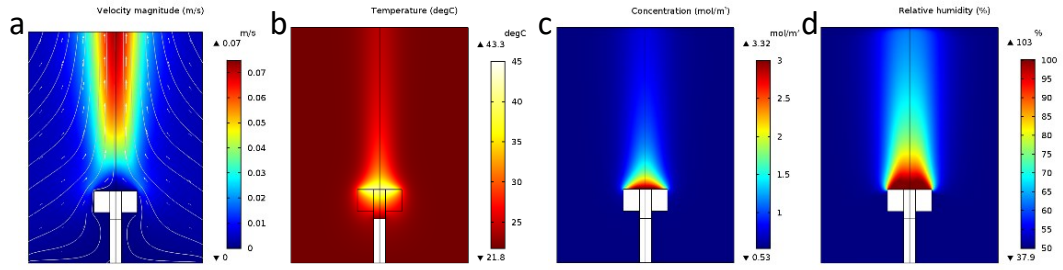

Figure 5.14 Single-side evaporation UE with a thermal insulation layer. (a) Velocity field. (b) Temperature field. (c) Vapor concentration field. (d) Relative humidity field.

5.5 Energy efficiency improvement

Based on the simulation, the key factors affecting the energy efficiency improving were further analysed. Higher ambient temperature decreases the temperature difference between the sample and the environment, which increases the energy efficiency for both UE and IE (Figure 5.15a). Higher ambient humidity deteriorates the vapour diffusion conditions, which decreases the efficiency (Figure 5.15b). Higher bulk water temperature increases the energy efficiency due to less heat loss to the bulk water (Figure 5.15c). Higher surface solar absorptance also increases the energy efficiency due to more solar energy captured into the system (Figure 5.15d).

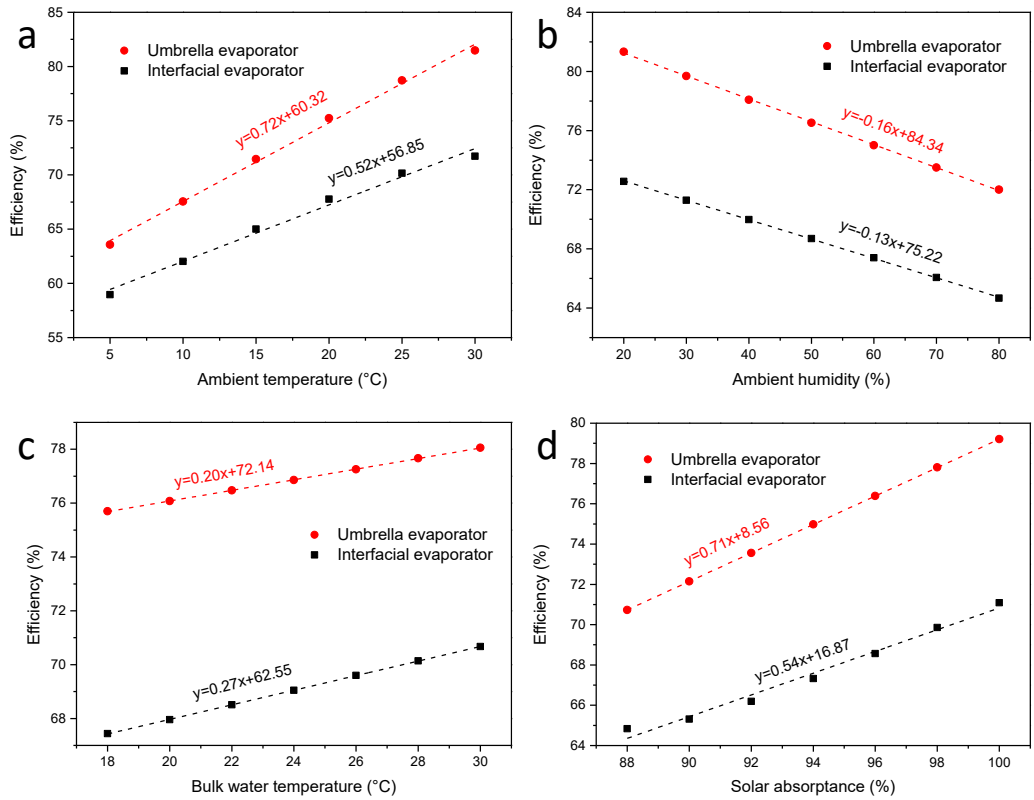

Figure 5. 15 Key factors affecting the energy conversion efficiency. (a) Ambient temperature versus the efficiency. (b) Ambient humidity versus the efficiency. (c) Bulk water temperature versus the efficiency. (d) Solar absorptance of the evaporation surface versus the efficiency.

In addition, the evaporation surface diameter also affects the efficiency. Larger evaporation surface diameter deteriorates the mass transfer conditions to make the vapour in the central part reach saturation, which decreases the evaporation rate and the efficiency for both UE and IE (Figure 5.16). With the evaporation surface diameter increasing, the heat loss to bulk water

percentage decreases for the UE (Figure 5.17). By contrast, the IE heat loss percentage increases due to the increasing heat transfer area.

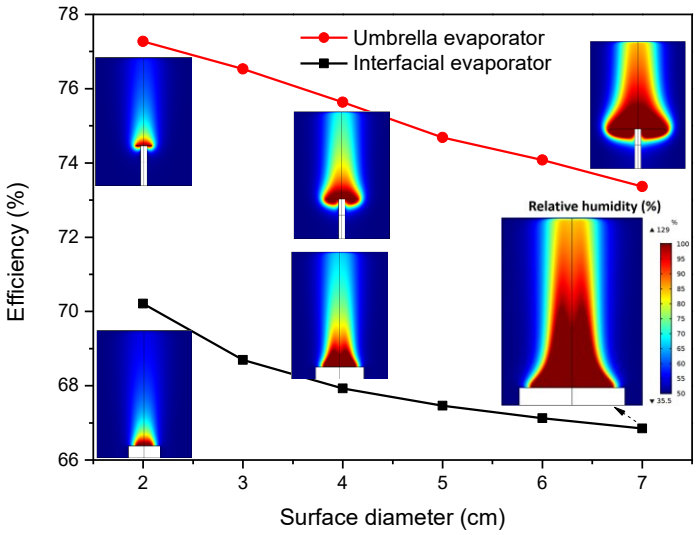

Figure 5.16 Evaporation surface diameter versus the efficiency.

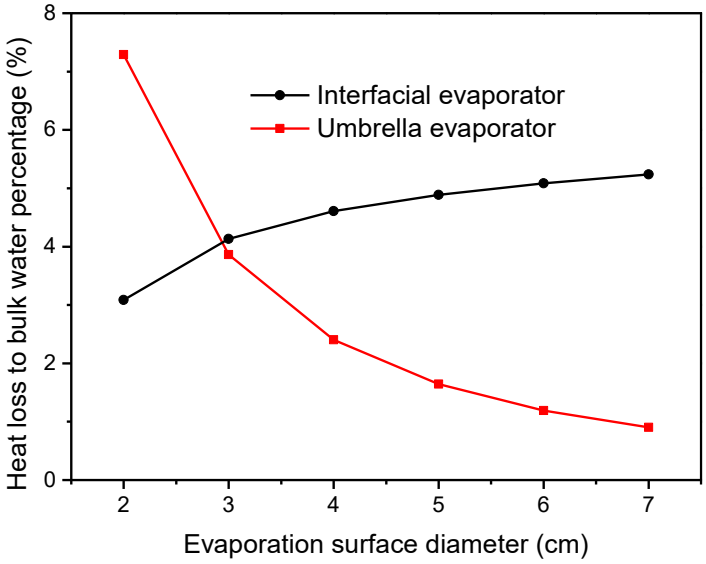

Figure 5.17 Evaporation surface diameter versus heat loss to bulk water percentage.

Specially, for the EU, there are another two factors: surface height and opening angle. If the surface is too low (for 3 cm diameter case, height less than 3 cm), the ground surface would affect the back vapour diffusion (Figure 5.18).

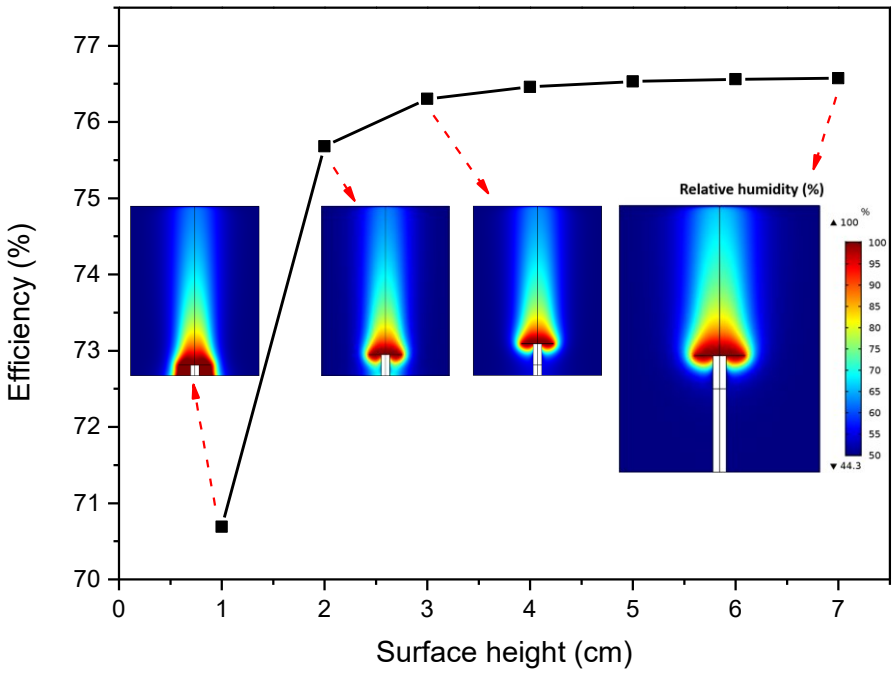

Figure 5.18 Surface height of the UE versus the efficiency.

Opening angle of the evaporation surface also affects the vapour diffusion (Figure 5.19). At the same vertical projection area, a larger opening angle enhances the back diffusion especially when the opening angle is above 105º (Figure 5.20).

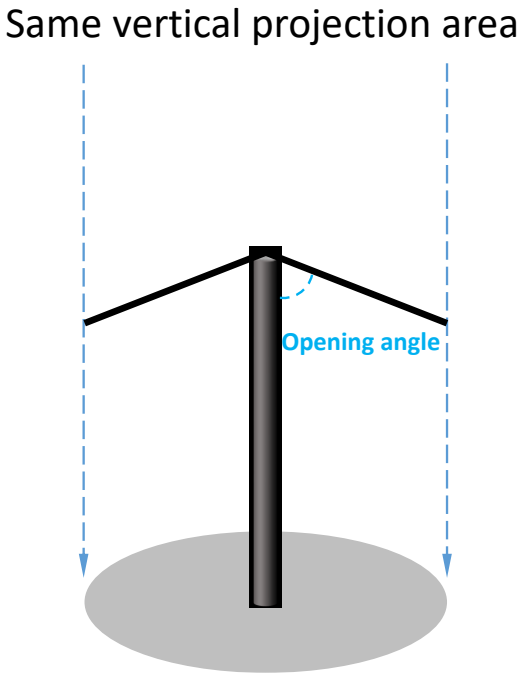

Figure 5.19 Schematic illustration of the opening angle and the vertical projection area of the UE.

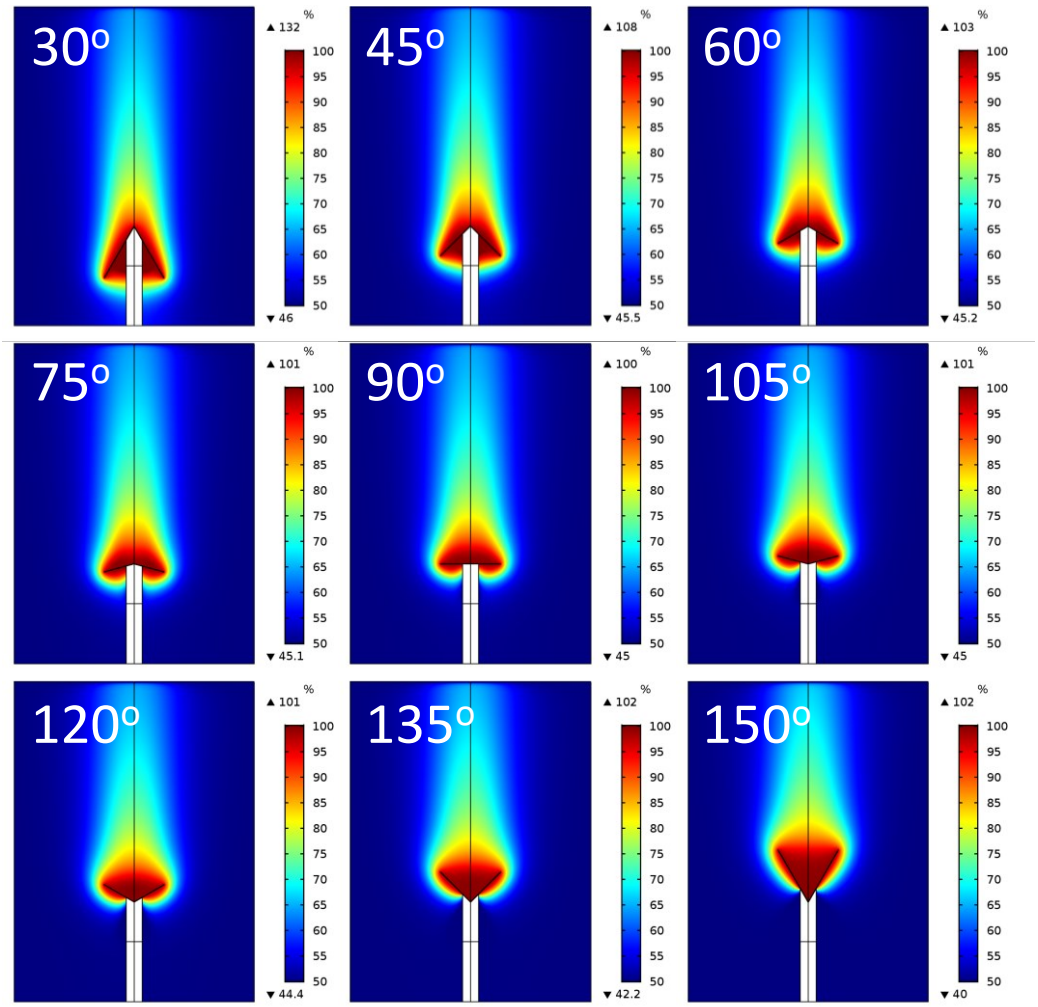

Figure 5.20 Influence of the opening angle of the UE on the relative humidity field.

Meanwhile, smaller or larger opening angles leads to larger surface area. A flat evaporation surface (opening angle = 90º) reaches the highest evaporation rate per unit surface area (Figure 5.21). It should be noted, the UE with any opening angle has a higher evaporation rate than the IE. As demonstrated, the energy conversion efficiency depends on the whole evaporation system. Li et al. have well described the attention points in the efficiency measuring process [160]. Here, some test environment and evaporator structure factors were quantitatively supplemented for a better evaluation of the efficiency.

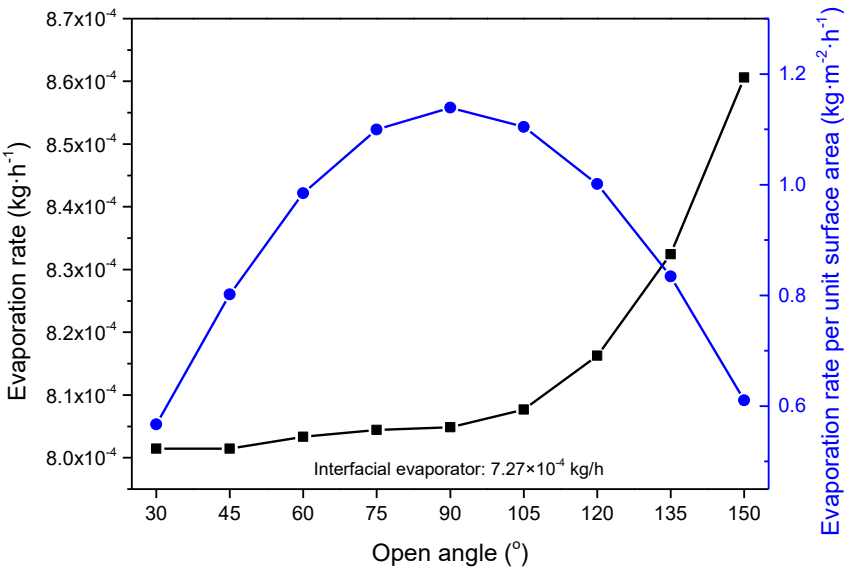

Figure 5.21 Influence of the opening angle of the UE on the evaporation rate in the same projection area and the evaporation rate per unit evaporation surface area.

5.6 Chapter summary

Here, a UE was demonstrated and its structural advantages in solar vapour generation over a typical IE was proved by both experiments and simulations, which owns to its double-sided evaporation feature, leading to a lower surface temperature and a higher energy efficiency. In solar evaporation, the UE has a much lower surface average temperature (33.8 ºC) than IE (40.5 ºC), which is caused by a higher evaporation rate (1.25 vs 1.10 $kg \cdot m^{-2} \cdot h^{-1}$, a 13.6% increase). In dark evaporation, due to double-sided heat gaining from the environment and double-sided vapour diffusion, the UE has an remarkable 72% higher evaporation rate (0.31 $kg \cdot m^{-2} \cdot h^{-1}$) than the IE (0.18 $kg \cdot m^{-2} \cdot h^{-1}$).

Lower ambient temperature, lower humidity, lower bulk water temperature, lower evaporation surface solar absorptance, and larger evaporation surface diameter all decrease the energy conversion efficiency of the system. Specially for the UE, lower evaporation surface height would affect the back vapour diffusion. At the same vertical projection area, a larger opening angle enhances the back diffusion especially when the opening angle is above 105º. Smaller or larger opening angles leads to larger surface area. A flat evaporation surface (opening angle = 90º) reaches the highest evaporation rate per unit surface area.

Chapter 6
Salt harvesting from an umbrella evaporator

6.1 Introduction

When a solar evaporator is applied on real seawater, with evaporation going salt would accumulate on the photothermal material and gradually slow down the evaporation, which would affect the continuous operation of the solar evaporation. At the same time, salt can be treated as a high added-value product. Therefore, harvesting salt while producing fresh water is the optimal strategy to achieve continuous operation and the economic maximization. Benefiting from the central water supply design of the umbrella evaporator, salt can be harvested from the evaporation surface edge. In this chapter, the salt accumulation behaviours on the edge are demonstrated in Section 6.2. The salt harvesting mechanism from the umbrella evaporator is proposed in Section 6.3. The salt falling behaviours of real seawater are different from the simple simulated seawater (3.5 wt% NaCl solution) because of its containing Ca^{2+} , Mg^{2+}, etc. The application situations on real seawater are analysed in Section 6.4. To quickly test if the pre-treated real seawater is satisfied for salt harvesting, a facile test method is proposed in Section 6.5. Conclusions are drawn in Section 6.6.

6.2 Salt accumulation and collection

The most attractive feature of the UE is the salt harvesting feature from the edge. Salt is washed to the edge and accumulates there, and then falls down. A UE with a saline water supply system was designed to adjust the water level using a communicating vessel (Figure 6.1). Water level is fixed at -2 cm below the evaporation surface by adjusting the water tank hight. The evaporaiton surface diameter is 3 cm. Simulated seawater (3.5 wt% NaCl solution) is used for this test. The pre-wetting method is to soak the evaporation surface into the corresponding solution for 1 min.

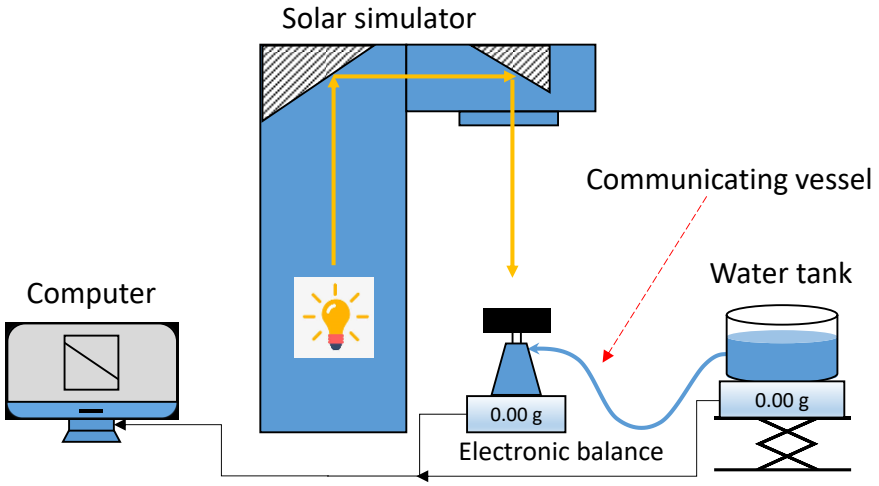

Figure 6.1 Solar evaporation salt harvesting test system under 1 sun (1 kW/m^2). The communicating vessel is used to adjust the saline water level of the sample.

As the water absorption of the filter paper decreases with time (Figure 6.2), to minimize its influence, a number of evaporation surfaces (polypyrrole coating on filter paper) were prepared and a new one was used for every test. The evaporation surface was first dipped in the saline water (3.5 wt% NaCl solution) for 1 min to make it pre-wetted and then placed on the polyester stick. The evaporation surface will be attached to the top of the polyester stick by water surface tension.

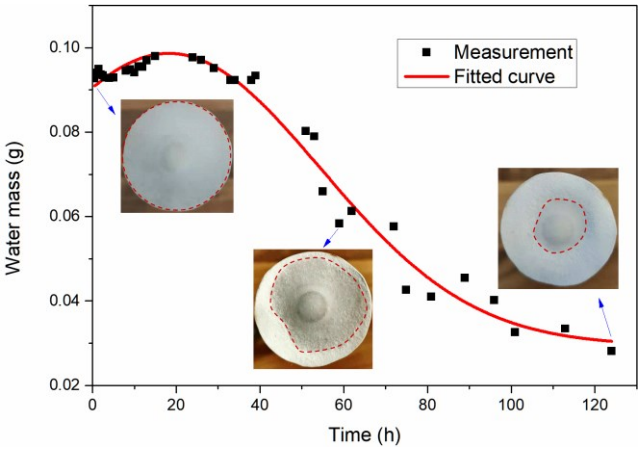

Figure 6.2 Water absorption of filter paper with time.

Water level determines the water supply to the surface, without water supply system, water level creases with evaporation (from -2 to -7.4 cm to the evaporation surface in 24 h), salt accumulates on the edge and does not easily fall (Figure 6.3). The salt falling at the edge is determined by the competition between the evaporation rate and the water supply rate at the edge due to capillarity, which can be simply controlled by adjusting the solar intensity. When the light was turned off (less evaporation to improve water supply), the accumulated salt began to fall piece by piece, and most of the salt fell down in 30 min. When fixed at -6 cm, there are still large salt block hanging at the edge, turning off the light also helped the salt falling; when fixed at -8 cm, salt ring tend to shrink.

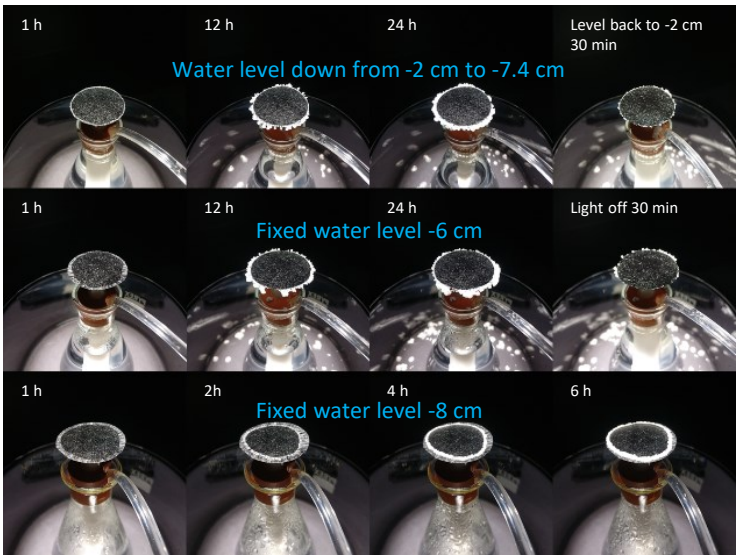

Figure 6.3 Salt accumulation and harvesting performance with different water levels.

The surface diameter is similar, which determines the water supply to the edge. When the water level is fixed at -2 cm, the UE with 3 cm diameter works well, and larger diameter accumulates more salt at the edge (Figure 6.4). Improving the water supply by turning the light off, most salt fell in 30 min.

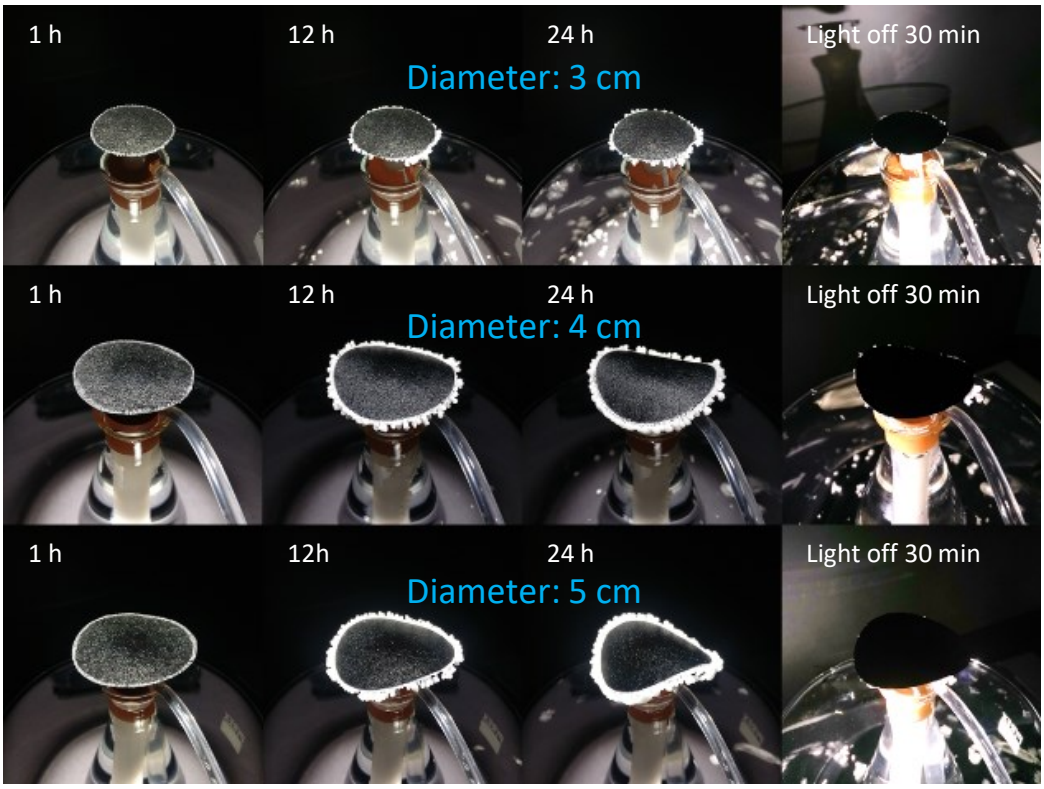

Figure 6.4 Salt accumulation and harvesting performance with different evaporation surface diameters.

When water supply is sufficient (-2 cm water level and 3 cm diameter), prewetting condition (no prewetting, by DI water, or by saturated NaCl solution) does not affect the salt collection (Figure 6.5).

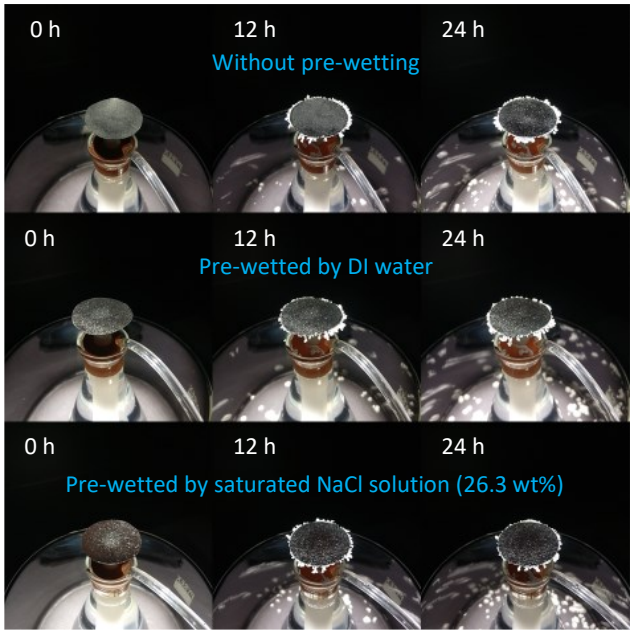

Figure 6.5 Salt accumulation and harvesting performance with different pre-wetting conditions.

The UE is able to deal with up to 7 wt% NaCl solution (2 times seawater concentration), which is the upper limitation of the reversed osmosis waste brine concentration due to hydraulic-pressure limitations [181], indicating UE even has the potential to deal with the reverse osmosis desalination waste brine (Figure 6.6).

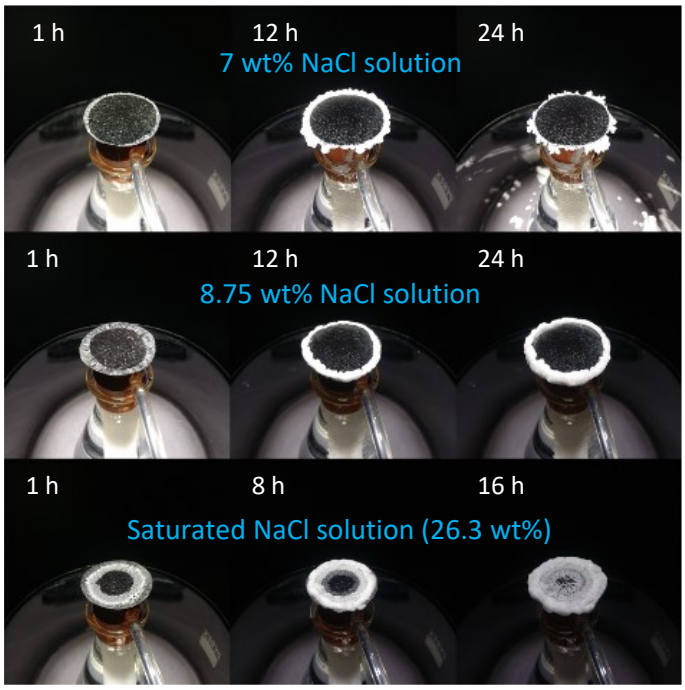

Figure 6.6 Salt accumulation and harvesting performance with different NaCl solution concentrations.

6.3 Salt harvesting mechanism

A UE under a microscope was set up to study the salt harvesting mechanism (Figure 6.7).

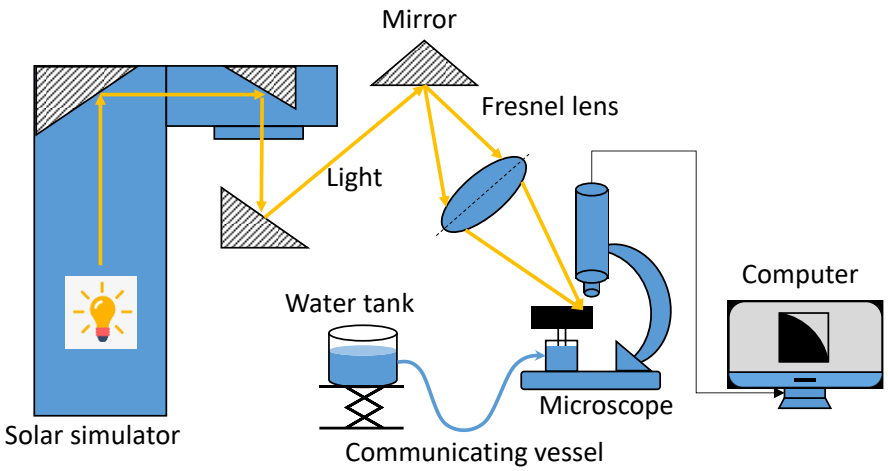

Figure 6.7 Salt precipitation on a UE under a microscope. A water tank is connected to the sample by a communicating vessel to keep the salt water level constant. The light intensity at the sample was calibrated to 1 kW/m^2 by introducing a Fresnel lens and adjusting the incident light intensity from the solar simulator.

NaCl crystallizes from the edge to the centre in a flat manner, and then some parts hump (Figure 6.8). These humps accelerate the dissolution of the small crystals around to make them precipitate on the humps forming 3D structures, which can be explained by Ostwald ripening [182]. Salt crystallization on the evaporation surface is a dynamic equilibrium of crystallization and dissolution, in which way salt moves to the edge. When the salt at the connecting points is dissolved, salt falls, leaving some tiny seed crystals for the following crystallization. The mobility of the salt determines if the salt can precipitate at the edge and fall. As above, insufficient water supply and high salt concentration will reduce the salt mobility to make the salt gradually precipitate to the centre.

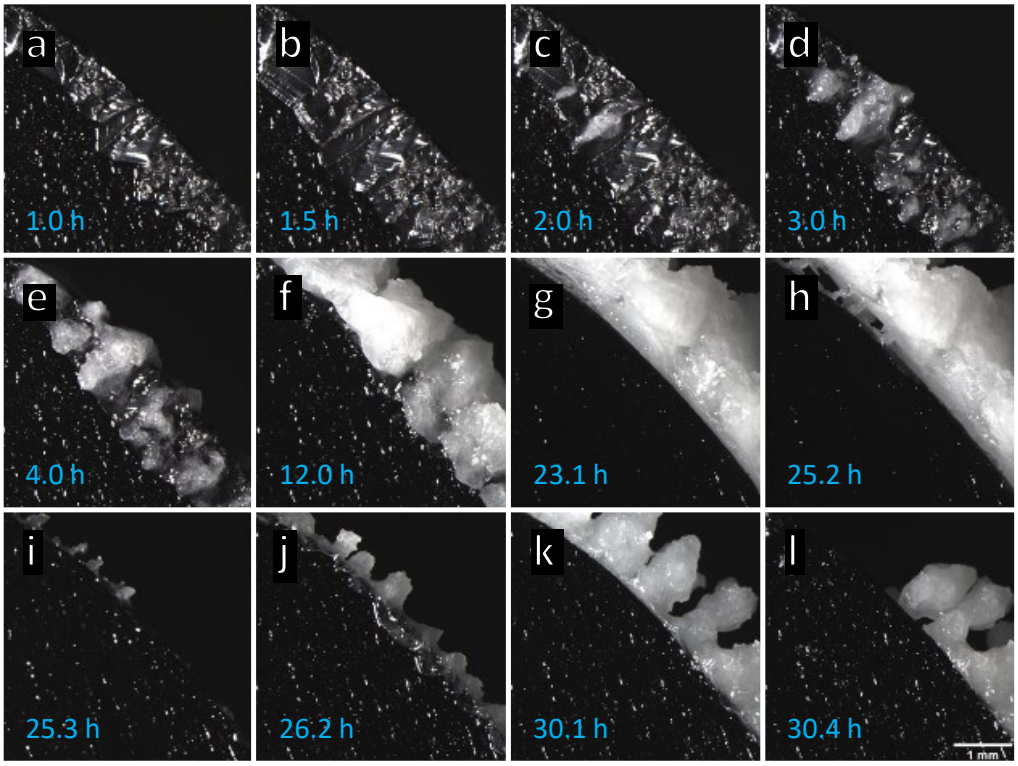

Figure 6.8 Salt precipitation and falling microscopic behaviours at microscale.

Water supply plays an important role in the dynamic equilibrium to harvest salt. It should be noted, salt does not grow from the root pushing forward on the edge, but from the front by wicking the salt water. Therefore, the front shape is changing all the time due to new precipitation (Figure 6.9).

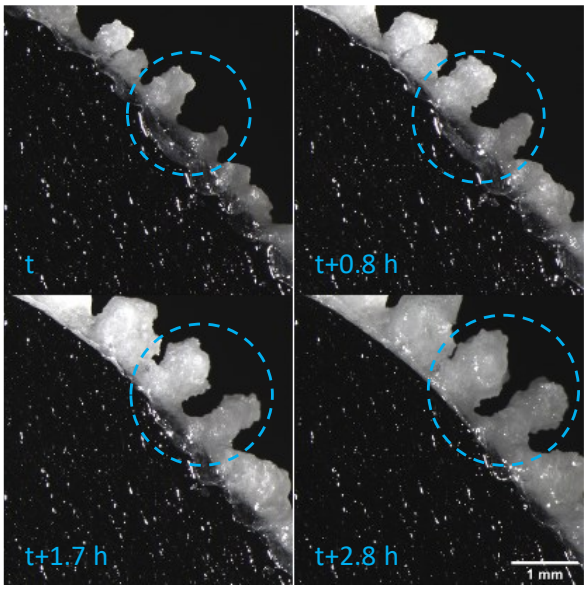

Figure 6.9 The front shape development of the salt precipitation.

The porous structures inside the salt clusters supply the water by capillary force, see the surface and cross section of a fallen salt cluster (Figure 6.10).

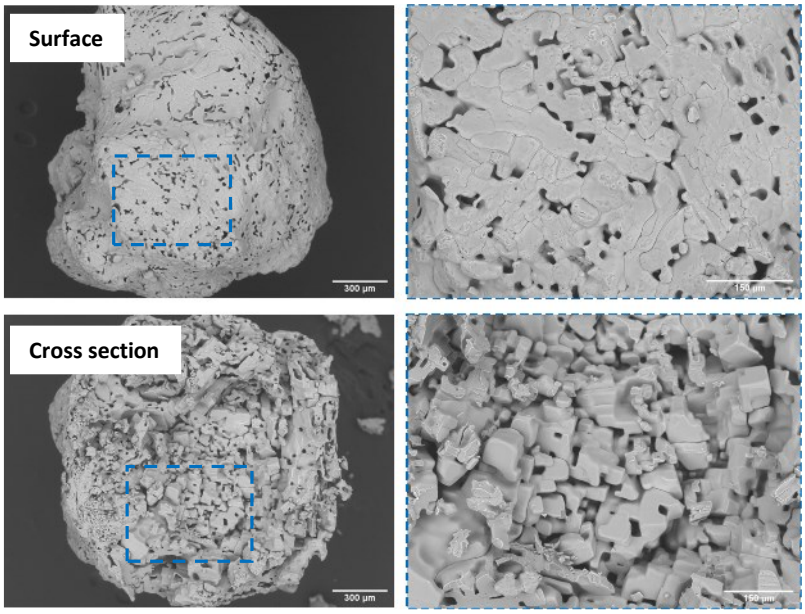

Figure 6.10 Porous surface and cross section of a fallen salt cluster.

Even the fallen salt still retains water, see the salt stains (Figure 6.11).

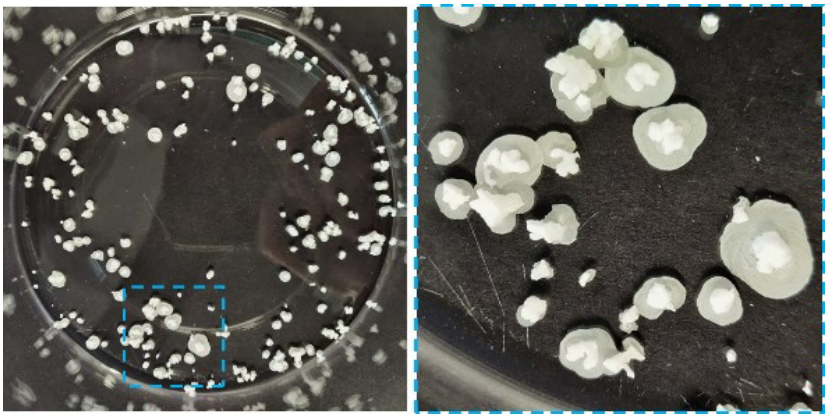

Figure 6.11 The fallen salts on the glass and the salt stains.

To sum up, salt water is wicked to the front by the channels in the salt clusters, during which the connecting salt is dissolved, leading to the salt falling (Figure 6.12).

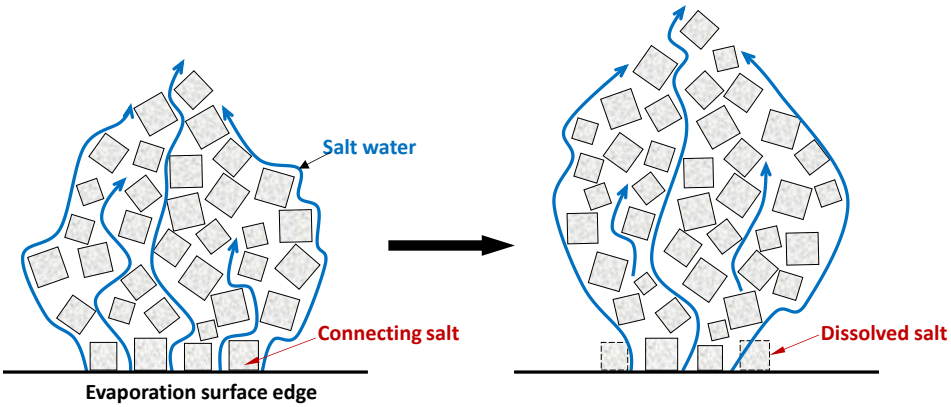

Figure 6.12 Salt falling from the edge mechanism schematic.

6.4 Application on real seawater

The UE works well in both SVG and salt harvesting in the simulated seawater (NaCl 3.5 wt%) above. However when applied on real seawater, the evaporation rate significantly decreases in the first 6 h and keep almost stable in the fallowing time (Figure 6.13). The salt gradually also covers the surface to the centre in the first 6 h and decreases clean evaporation area, after which the salt covering area stops increasing and the salt accumulation become thicker, which explains the change of evaporation rate during this time.

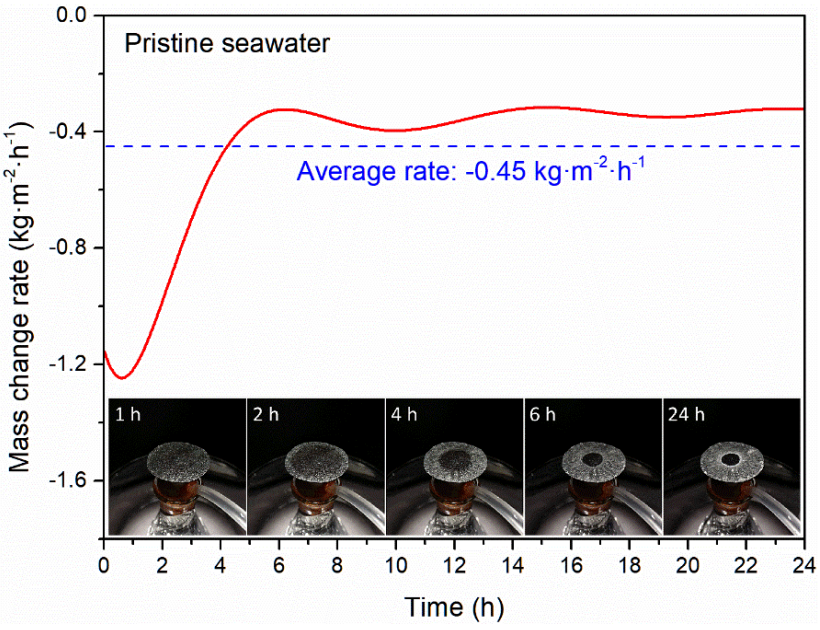

Figure 6.13 Application on pristine seawater.

To find out the reason why the salt does not accumulate at the edge from real seawater, fully simulated seawater was used by adding NaCl, KCl, Na_2SO_4, $CaCl_2 \cdot 2H_2O$, and $MgCl_2 \cdot 6H_2O$ gradually to find out which ions affect the salt falling the most (Table 6.1).

Table 6.1 Simulated seawater ionic concentration [183].

Component	Concentration (g/kg seawater)
Cl^-	19.4
Na^+	10.8
SO_4^{2-}	2.71
Mg^{2+}	1.29
Ca^{2+}	0.41
K^+	0.39
Total	35.0

First, salt harvesting was achieved from the basic simulated seawater (NaCl, Na_2SO_4, and KCl) (Figure 6.14a). The system still works well when Ca^{2+} is added, however, when Mg^{2+} is added (even if its 1%), the salt does not fall until Mg^{2+} is decreased to its 0.1% (Figure 6.14b-f). Notably, higher Ca^{2+} concentration would also stop the system (Figure 6.14g). As a result, Ca^{2+} and Mg^{2+} both affect the salt harvesting, especially Mg^{2+}, which should be decreased to its 0.1% (0.0129 g/L). Based on the above findings, Mg^{2+} was removed by adjusting the seawater pH to 12 by NaOH to precipitate $Mg(OH)_2$ ($Ksp=1.5\times10^{-11}$), the solution was filtered, then pH was adjusted back to 7 by HCl, and the salt harvesting was achieved from the fully simulated seawater (Figure 6.14h). However, when applied on real seawater, salt hangs at the edge due to other ions interferences (Figure 6.14i).

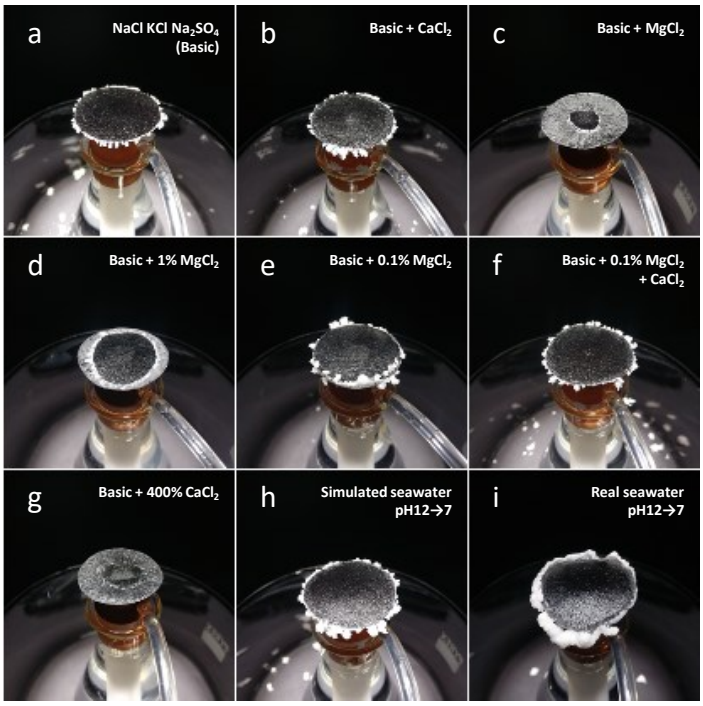

Figure 6.14 Salt harvesting of simulated seawater with different compositions. 1% $MgCl_2$ means Mg^{2+} concentration is decreased to its 1% (0.129 g/L).

Based on the analysis above, for real seawater, Mg^{2+} was first removed by adjusting pH to 12 by adding NaOH (~ 4.64 g per liter seawater), and then further 50% Ca^{2+} by adding Na_2CO_3 to precipitate $CaCO_3$ ($Ksp=4.8\times10^{-9}$) (Figure 6.15). Then a centrifuge was used to separate the sediments out, and the solution pH was adjusted back to 7 by adding HCl. It should be noted, due to the solubility equilibrium of $Mg(OH)_2$ and $CaCO_3$ in water, Mg^{2+} and Ca^{2+} cannot be removed completely. After the pretreatment, continuous operation of SVG and salt harvesting for 100 h was achieved (Figure 6.16). The above concentration of these two ions is the system working higher limit.

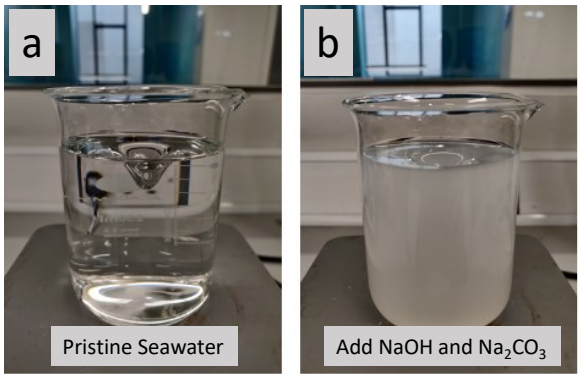

Figure 6.15 Seawater pretreating. (a) Pristine seawater. (b) Seawater after adding NaOH and Na_2CO_3 containing precipitates.

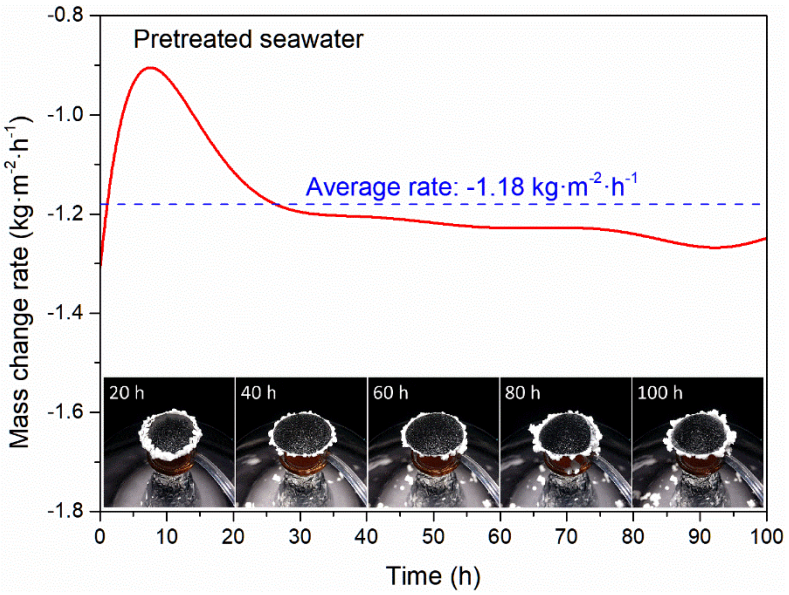

Figure 6.16 Application on pre-treated seawater.

After solar desalination, the ionic concentration (1.91 mg/L total dissolved solids) decreased far below the WHO drinking water standard (less than 1000 mg/L) (Figure 6.17).

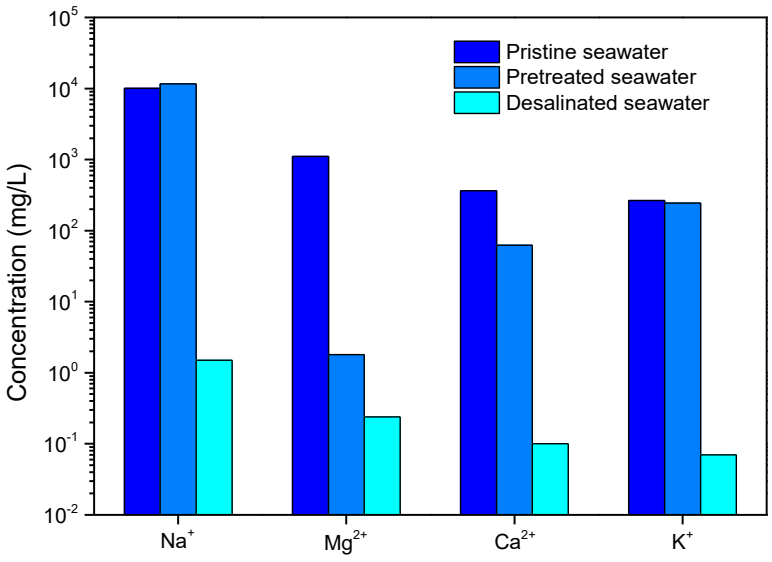

Figure 6.17 Ionic concentrations of pristine, pre-treated, and desalinated seawater.

Ca^{2+} and Mg^{2+} can also reduce the mobility of the salt on the evaporation surface due to their higher ionic potential, which indicates the surface charge density of an ion (Table 6.2).

Table 6.2 The change number, radius and ionic potential of the main ions [184, 185].

	Na^+	K^+	Mg^{2+}	Ca^{2+}	Cl^-	SO_4^{2-}
Charge number (z, e)	1+	1+	2+	2+	1-	2-
Ionic radius (r, nm)	0.116	0.152	**0.086**	**0.114**	0.167	0.258
Ionic potential (z/r, e/nm)	8.62	6.58	**23.26**	**17.54**	-	-

Ions with higher ionic potential more strongly attract opposite ions around. At the same time, Ca^{2+} and Mg^{2+} (especially Mg^{2+}) have the smallest diameters in the system (Table 6.2), making them easier to insert into the NaCl precipitations, and link the precipitations to make them bond stronger, which reduces the liquidity of the salt and make the salt cover the surface gradually to the centre (Figure 6.18). Lower Ca^{2+} and Mg^{2+} concentration make it possible to precipitate at the edge, however, their existence also affects the salt falling. Due to the linking of these two ions, the salts hanging on the edge become bigger and harder, and even bind with their neighbours, making it more difficult to fall (Figure 6.18).

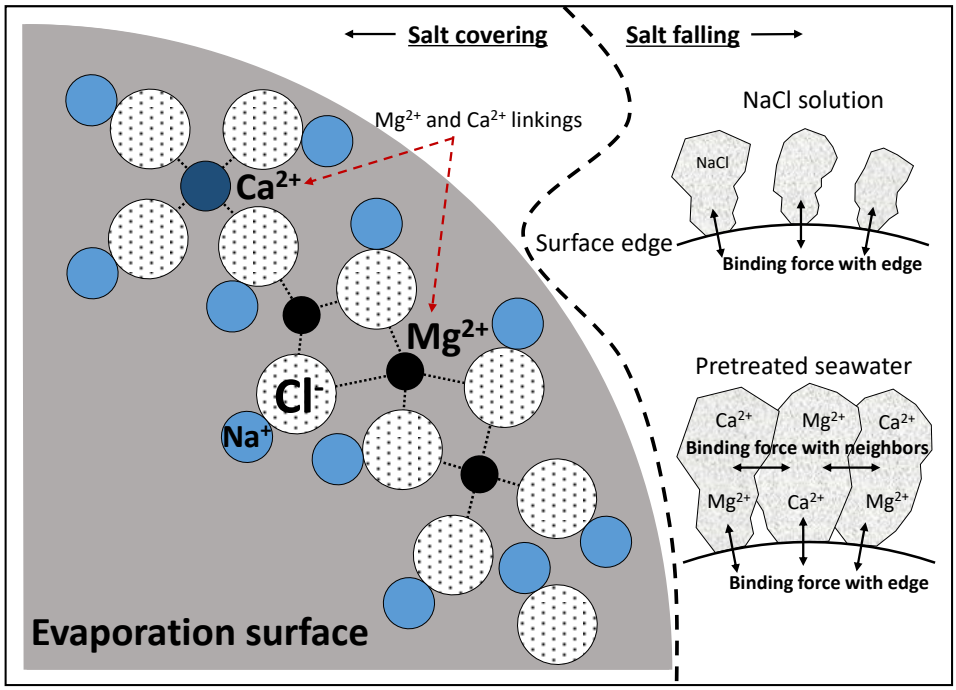

Figure 6.18 Salt covering and falling mechanism schematic for real seawater.

6.5 Facile test for salt harvesting

The pre-treated seawater quality (Mg^{2+} and Ca^{2+} content) determines if salts can be harvested from the edge. Knowing the ion contents usually requires professional equipment (e.g. ICP-MS or AAS). Here, a facile method is proposed to test if the pre-treated seawater is satisfied for salt harvesting by simply dipping a drop on a glass slide. When the drop is naturally dry, the salt creeping that can be seen by naked eyes indicates the possibility of salt falling. Salt creeping is a common phenomenon that salt precipitate far from the evaporation boundary [186]. NaCl solution has the typical salt creeping behaviour, with fine crystals spreads out from the boundary (Figure 6.19).

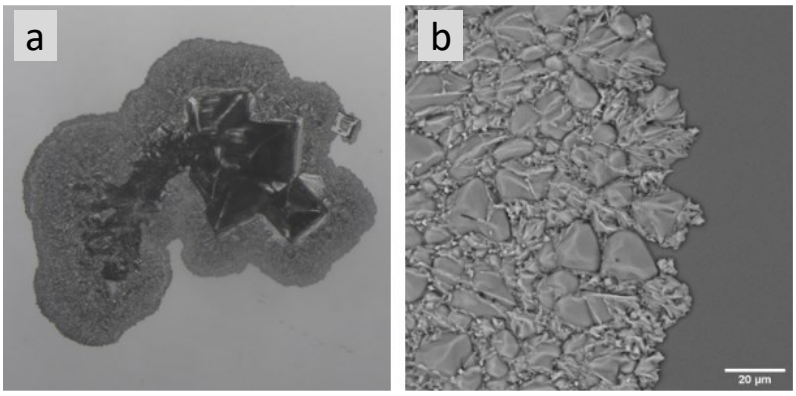

Figure 6.19 Salt creeping of NaCl solution (3.5 wt%). The salt stain was created by dipping 20 µm salt water on a glass slide and making it naturally dry. (a) Salt creeping image by microscope. (b) Salt creeping image by SEM.

The pre-treated seawater has a similar behaviour by naked eyes, however, at the micro level, the crystals are closer with a top covering (Figure 6.20a, b). There is no such salt creeping behaviour for pristine seawater (Figure 6.20c).

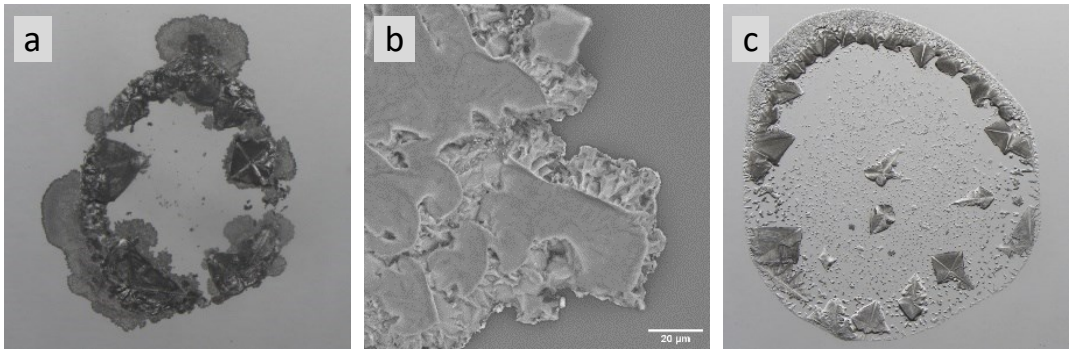

Figure 6.20 Salt creeping of the pre-treated seawater. (a) Salt creeping image by microscope. (b) Salt creeping image by SEM. (c) Pristine seawater.

To verify the correlation of the salt creeping phenomenon and salt falling, different solutions were tested (Figure 6.21). The concentrations of the salts derive from the simulated seawater content above. The pretreating method for the fully simulated seawater and real seawater is to adjust the solution pH to 12 by adding NaOH and separate the sediments, and then adjust the solution pH back to 7 by adding HCl. To sum up, salt falling happens when the salt creeping phenomenon appears.

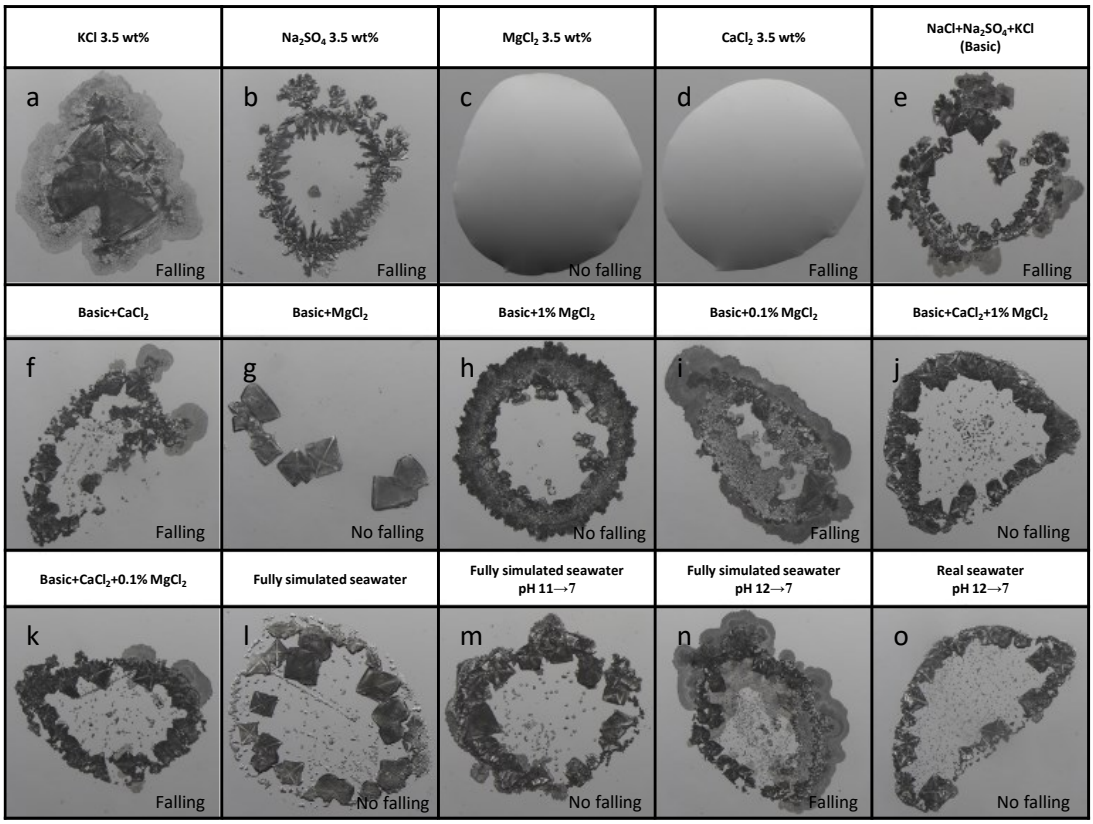

Figure 6.21 Different salt creeping images and whether their falling happens. (a-d) Pure 3.5 wt% KCl, Na_2SO_4, $MgCl_2$ and $CaCl_2$ respectively. (e) NaCl, Na_2SO_4, and KCl as basic solution. (f) Basic and $CaCl_2$. (g) Basic and $MgCl_2$. (h) Basic and 1% $MgCl_2$. (i) Basic and 0.1% $MgCl_2$. (j) Basic, $CaCl_2$ and 1% $MgCl_2$. (k) Basic, $CaCl_2$ and 0.1% $MgCl_2$. (l) Fully simulated seawater. (m) Fully simulated seawater after adjusting pH to 11 and back to 7 to remove Mg^{2+}. (n) Fully simulated seawater after adjusting pH to 12 and back to 7 to remove Mg^{2+}. (o) Real seawater after adjusting pH to 12 and back to 7 to remove Mg^{2+}.

For salt creeping behaviour, at the end of drying, salt at the boundary forms many scattered crystals in a planar way, leaving channels between them to transport water to the frontline by capillary force (Figure 6.22).

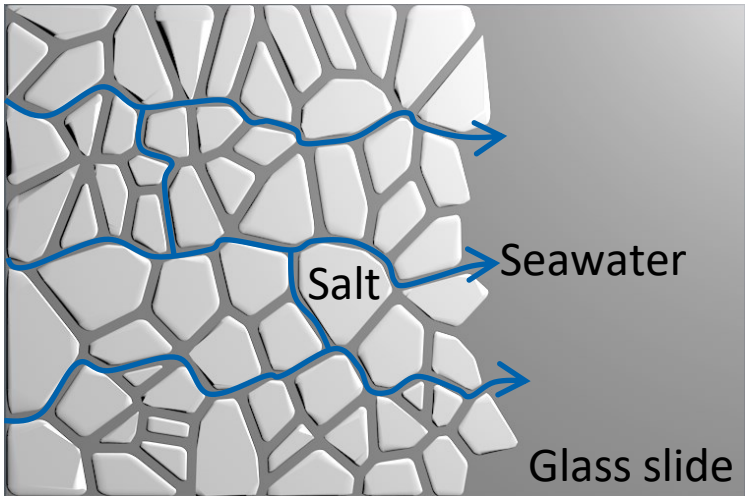

Figure 6.22 Salt creeping mechanism schematic.

When Ca^{2+} and Mg^{2+} content is high, due to their higher ionic potential (stronger ability to attract particles with opposite charge), they link the water with salts to hold the water from flowing forward, and there will be no salt creeping (Figure 6.23). Therefore, it can be determined if Ca^{2+} and Mg^{2+} content is low enough for the UE salt harvesting by observing the salt creeping. Overall, the more obvious the salt creeping phenomenon, the easier it is for the salt to fall for harvesting.

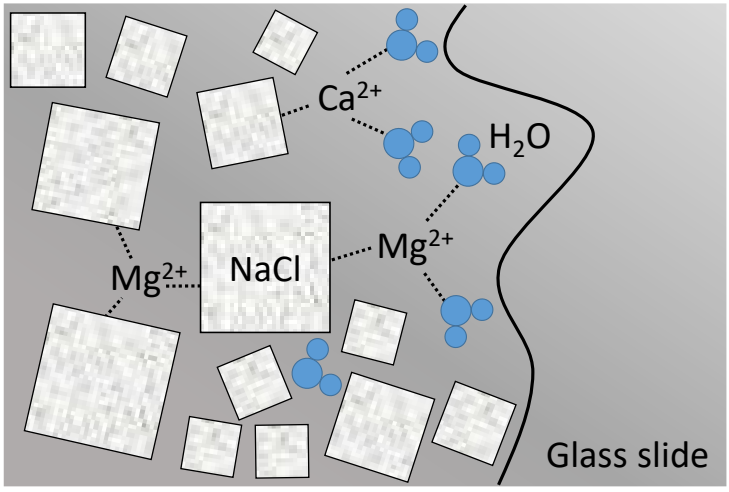

Figure 6.23 Schematic of the restraining salt creeping by Ca^{2+} and Mg^{2+}.

6.6 Chapter summary

This chapter showed the salt harvesting performance of the umbrella evaporator. In addition, the salt falling mechanism was proposed and how the components in real seawater affect the salt falling was also analysed. Water level determines the water supply to the surface, and similarly the surface diameter determines the water supply to the edge. A lower water level or larger surface diameter makes more salt accumulate on the edge and not fall easily. When water supply is sufficient, prewetting condition (no prewetting, by DI water, or by saturated NaCl solution) does not affect the salt collection. The umbrella evaporator is capable of harvesting salt from saline water containing up to 7 wt%. Salt accumulation on the evaporation surface is a dynamic equilibrium of crystallization and dissolution, in which way salt moves to the edge. The mobility of the salt determines if the salt can precipitate at the edge and fall. Insufficient water supply, high salinity, and the presentation of Mg^{2+} (especially) and Ca^{2+} will all reduce the salt mobility to make the salt gradually precipitate to the centre. The salt on the edge grows from the front by wicking the water through its porous structures inside and falls due to the dissolution of its connecting parts. By removing Mg^{2+} and Ca^{2+} through sedimentations, continuous solar vapour generation with salt harvesting from real seawater for 100 h was achieved. Finally, a facile method was proposed to determine the water quality for salt harvesting by simply dipping a drop on a glass slide to observe the salt creeping behaviours. The more obvious the salt creeping phenomenon, the easier it is for the salt to fall for harvesting.

Chapter 7
Suspending evaporator with top water supply

7.1 Introduction

Solar evaporation utilizes photothermal materials to convert solar energy into heat for water evaporation and generates high-quality drinkable fresh water [68, 118, 145]. It is a promising desalination technology to mitigate fresh water scarcity problem in a green and sustainable way [56, 187, 188]. In recent years, the exploration of photothermal materials has received extensive interest [3, 189, 190]. It is clear that the energy conversion efficiency for the evaporation system is determined by two major factors: solar absorptance of the photothermal materials (from solar energy to heat) and vapour generation efficiency (VGE) of the evaporator (from heat to vapour). Compared to the intensive study of photothermal materials, the investigation of the structural improvement of evaporators is still insufficient. Proper structural optimization could improve the VGE by reducing heat loss, supplying sufficient water for evaporation and improving the vapour transport conditions.

A typical IE floats at the water-air interface, with a top solar absorbing layer, and a thermal insulation layer below to localize the heat on the evaporation surface [58, 119, 191]. Water supply is typically driven by capillary force originated from the middle porous layer. One of the key design considerations of IE is to reduce heat leak into the bulk fluid, which relies on the insulation layer. Either waterproof insulation layer or porous insulation layer has been used. Employing waterproof thermal insulation layers reduces heat leak but forces water go through the side walls to the evaporation surface centre [75, 103], which can hardly satisfy the evaporation rate on a larger evaporation surface. Using porous thermal insulation layer allows the below water to be directly transported to the evaporation surface, which solves the water supply issue for large evaporation surfaces [69, 192], but suffers greatly the heat loss problem through water channels. More importantly, when applied on seawater, salt would accumulate on the photothermal materials and gradually slow down the evaporation rate [193, 194].

The umbrella evaporator in Chapter 5 and 6 uses a central archive structure to supply water to the evaporation surface and accumulates salts at the edge, where salts can automatically fall down by gravity. The structure improvement leads to impressive results for continuous water production and salt harvesting concurrently. However, its water transport rate is still limited by the capillary force, which is difficult for higher evaporation rate. For example, the evaporator used had a maximum evaporation surface diameter of 3 cm and surface height of 8 cm, which greatly limits the larger area applications of the umbrella evaporator.

To address this limitation, a double-sided suspending evaporator was further developed with top water supply and surface water distribution systems for high-efficient concurrent solar evaporation and salt harvesting. The water supply for this evaporator is from the top and is dripped onto the evaporation surface centre, which gets away from the capillary limitation while completely cuts off the heat loss to the bulk fluid below. Owning to the central top water supply, salt accumulates at the evaporation surface edge and falls down due to gravity for harvesting. The evaporation rate (3 cm in diameter case) reached 1.40 $kg \cdot m^{-2} \cdot h^{-1}$ with DI water under 1 sun (1 kW/m^2), whose corresponding energy conversion efficiency is 95.7%, with a remarkable low surface average temperature of 28.2 ºC. Through both simulations and experiments, a radial arterial water distribution system was further designed to efficiently distribute the water to a larger evaporation surface, and 70 h continuous solar evaporation and salt harvesting at 1.04 $kg \cdot m^{-2} \cdot h^{-1}$ (based on the complete circle area with 11 cm in diameter) was achieved with 3.5 wt% NaCl solution on the floriform evaporation surface. This work reveals the water supply and salt accumulation problems in scaling up the solar evaporators and advances new ideas for the structural design of the evaporators for high-efficient large area applications.

7.2 Suspending evaporator conception

The most widely studied IEs float at the water-air interface, relying on only single-sided evaporation (Figure 7.1). Generally, a thermal insulation layer floats the whole structure and reduces the heat loss to the bulk water by the

bottom surface. Recently, an umbrella-shaped evaporator is drawing more and more attention. It utilizes a pillar to support the evaporation surface and supply water to the top by capillary force. This umbrella evaporator achieves double-sided evaporation, which has been proved more efficient than single-sided evaporation in the previous section. The suspending evaporator proposed in this work adopts top water supply to achieve double-sided evaporation and completely cuts off the heat loss to the bulk water (Figure 7.1). In addition, the water supply rate should meet the evaporation rate to keep the system working at a high efficiency. The water supply of interfacial and umbrella evaporators heavily relays on the capillary force of the water transport system, which limits their scale-up. The proposed top water supply system is able to provide sufficient water for evaporation.

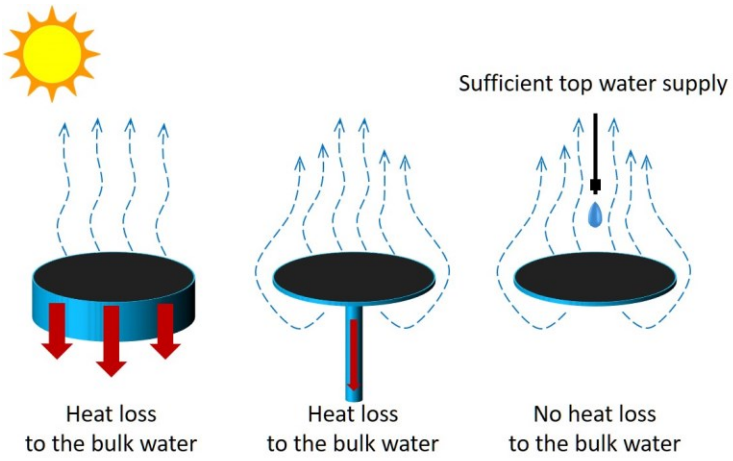

Figure 7.1 Interfacial evaporation, umbrella evaporator and suspending evaporator comparison in evaporation and heat loss.

7.3 Evaporation performance

Figure 7.2a show the schematic view of the application of the suspending solar evaporator. Polypyrrole was coated on a filter paper to obtain the black evaporation surface (0.16 mm in thickness), whose solar absorptance is 96.2% and porosity is 0.806. To examine its solar evaporation performance, a syringe pump than can control the flow rate was used to supply water to the evaporation surface under a solar simulator (1 kW/m^2) (Figure 7.2b).

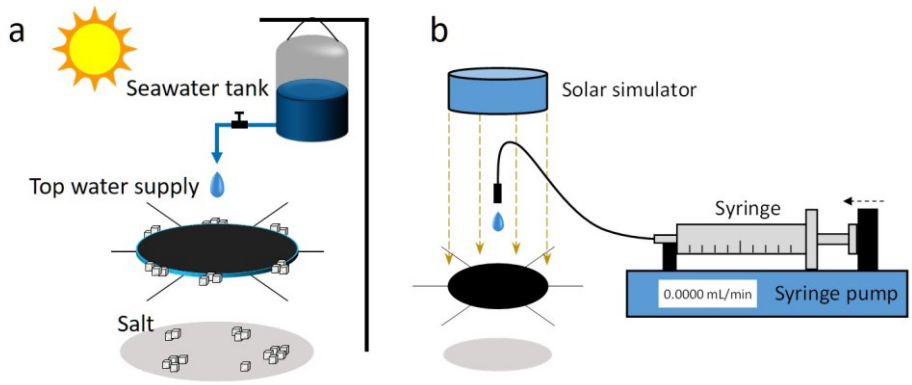

Figure 7.2 Schematic illustration of the application and experiment systems. (a) Schematic illustration of the suspending solar evaporator with salt harvesting system. (b) Solar evaporation experiment system under 1 kW/m^2.

The ambient temperature is around 21 ºC and the humidity is around 50% during the test. The water supply rate is determined by following two requirements: no dry part on the top evaporation surface and no water accumulation on the back surface by observation. The suspending evaporator (3 cm in diameter) works steady with DI water at the top water supply rate of 0.0165 mL/min, corresponding to 1.40 kg·m^{-2}·h^{-1}, and the corresponding energy conversion efficiency is 95.7% (Figure 7.3a). The surface average temperature is 28.2 ºC, which is much lower than a typical IE (40.3 ºC) under the same test environment in our previous work [195]. For this suspending evaporator, lower surface average temperature indicates higher energy conversion efficiency. The energy loss for the suspending evaporator only comes from the heat loss to the environment, mainly due to natural convection. Therefore, lower surface average temperature decreases the temperate difference with the surrounding environment, leading to a higher efficiency. Notably, the evaporator achieves salt harvesting from the evaporation surface edge at the same salt water supply rate (0.0165 mL/min) with a surface average temperature of 29.3 ºC (Figure 7.3b). The suspending evaporator can work at a wide range of water supply. Lower water supply (0.0132 mL/min, i.e. 80% of the steady rate) makes the surface dry, and the salt accumulates to the center instead of at the edge (Figure 7.3c), while the system works well again when it is set back at the steady rate. Insufficient water supply increases the surface average temperature to 33.2 ºC, indicating a lower efficient. By contrast, higher water supply (0.0215 mL/min, i.e. 130% of the steady rate)

makes the surface wet and salt-free. Excess water takes the salt down by drops, leaving few salt precipitates at the edge (Figure 7.3d). Excess water supply decreases the surface average temperature to 28.3 ºC, which is almost equal to the DI water case.

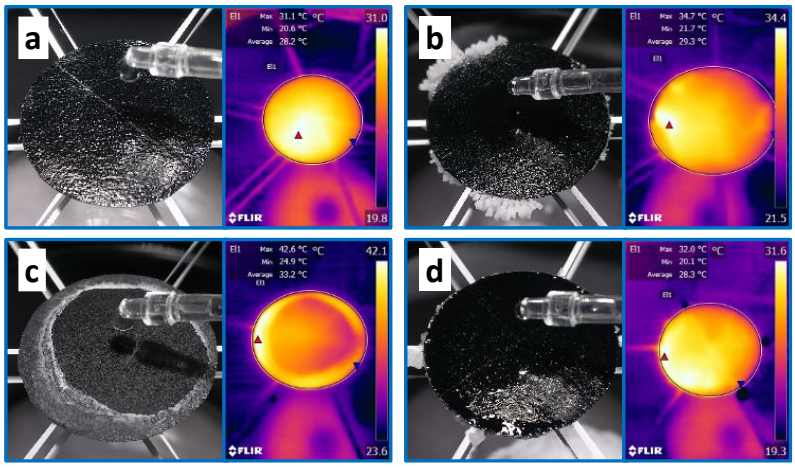

Figure 7.3 Solar evaporation performance of the suspending evaporator (3 cm in diameter) with top water supply. (a) Evaporation with DI water at 0.0165 mL/min. (b) Evaporation with 3.5 wt% NaCl solution at 0.0165 mL/min (100%). (c) Dry evaporation with 3.5 wt% NaCl solution at 0.0132 mL/min (80%). (d) Wet evaporation with 3.5 wt% NaCl solution at 0.0215 mL/min (130%).

7.4 Simulation of salt distribution

To better understand the salt accumulation behaviours on the evaporation surface, the saltwater flow and salt accumulation process was simulated by a 2-dimensional plane model using the commercial software COMSOL Multiphysics. The salt transport is achieved by both fluid flow and diffusion in water. The fluid flow (Darcy's law) and salt transport processes are used in the model. The fluid flow is a steady-state process, which is simulated first. The velocity magnitude results obtained is provided to the salt transport process for its dynamic process calculation. The evaporation surface was set as a porous media that can transport water by capillary force. The water supply was continuous from a centre part circle (3 mm in diameter). The diameter of the evaporation surface was 3 cm, and its temperature was set uniform at 29.3 ºC. For simplification, each part of the surface was set to evaporate at a uniform rate of 1.40 $kg \cdot m^{-2} \cdot h^{-1}$.

Model equations. Darcy's law is applied to simulate the water flow in the porous media, and the NaCl diffusion coefficient in water is modified by

Bruggeman model to fit in the porous media. Water properties derive from the software built-in database. For fluid flow:

$$\frac{\partial}{\partial t}\left(\varepsilon_p \rho\right) + \nabla \cdot \left(\rho \mathbf{u}\right) = Q_m \tag{7-1}$$

$$Q_m = -\frac{m\_evap}{h\_disc} \tag{7-2}$$

$$\mathbf{u} = -\frac{\kappa}{\mu}\nabla p \tag{7-3}$$

here ε_p is the porosity of the porous media (0.806), ρ is fluid density, $\mathbf{u}$ is the fluid velocity. Q_m is the mass source which relates to the evaporation rate (*m_evap*: 1.40 kg·m^{-2}·h^{-1}), *h_disc* is the thickness of the evaporating layer (0.16 mm), κ is the permeability of the porous media (1×10^{-13} m^2), μ is the fluid viscosity, and p is the fluid pressure. For salt diffusion:

$$\frac{\partial c}{\partial t} - D\nabla^2 c + \mathbf{u}\cdot\nabla c = 0 \tag{7-4}$$

$$D = \frac{\varepsilon_p}{\tau} D_{inwater} \tag{7-5}$$

here c is NaCl concentration, D is NaCl diffusion coefficient in the porous media, $D_{inwater}$ is NaCl diffusion coefficient in water (1.5×10^{-9} m^2/s), τ is the tortuosity of the porous media which can be got by Bruggeman model as below:

$$\tau = \varepsilon_p^{-1/2} \tag{7-6}$$

Boundary and initial conditions. The pressure at the inlet boundary is set zero, thus water can flow in when evaporation decreases the internal pressure. The flow rate is controlled by pressure to reach mass balance. The inlet concentration of salt water is 0.6 mol/L (containing 3.5 wt% NaCl) to simulate seawater. The initial NaCl concentration on the surface equals to the inlet concentration (0.6 mol/L), meaning the surface is pre-wetted by salt water. The initial pressure is zero. Extremely fine mesh of the evaporation surface was automatically generated by COMSOL. The dependence of the mesh size has been tested and its influence is negligible. The simulation results agree

well with the experiment results, which can be directly validated by the salt distribution results in the following sections.

Simulation results. The salt water flows from the centre of to the edge accompanied with evaporation, and along the flow the velocity rapidly decreases at first and then decreases steadily to the minimum at the edge, whose maximum velocity is 0.2063 mm/s (Figure 7.4a). The saltwater flow carries NaCl to the edge and its concentration increases with evaporation. At 700 s, the edge reached saturation (27 wt% at 29.3 ºC). Although salt accumulation will block the saltwater flow, which affects salt transportation on the evaporating surface, salt precipitation process takes time and trends to firstly occur on the surface instead of inside the channels [196]. Hence the simulation was calculated a little further (1300 s) to show the saturated area variation trend in the near future after reaching saturation. With evaporation, NaCl concentration increases rapidly only at the edge, leaving most parts of the surface unsaturated (Figure 7.4b). This edge accumulation behaviour makes it possible to harvest salts from the edge and leaves the remaining surface work normally. After a certain salt accumulation time, the saturated area percentage soars from 0 in a short time and its growth is slowing down in the near following time (Figure 7.4c). Salt distribution on the evaporating surface is determined by both convective mass transfer to the edge and diffusive mass transfer to the centre. At the beginning of saturation (700 s), the average convective flux is 0.0215 $mol \cdot m^{-2} \cdot s^{-1}$ and the average diffusive flux is 3.192×10^{-4} $mol \cdot m^{-2} \cdot s^{-1}$. The convective flux is over 67 times larger than the diffusive flux, thus the convective flux dominates the salt distribution. Therefore, the total NaCl flux field is similar to the velocity field, with slight difference at the edge due to back diffusive flux (Figure 7.4d).

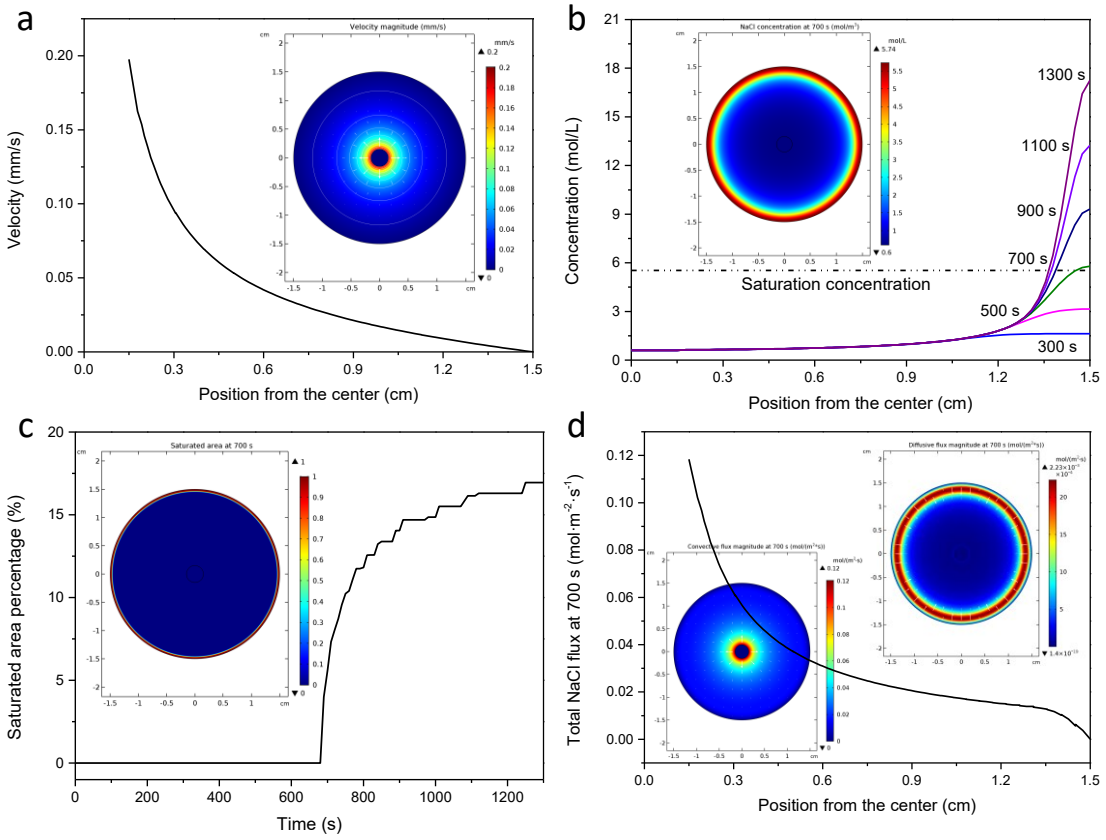

Figure 7.4 Simulation results of the salt distribution on the evaporation surface. (a) Velocity distribution along the radius. Insert is the velocity magnitude. (b) Salt concentration distribution along the radius from 300 s to 1300 s. Insert is NaCl concentration magnitude at initial saturation time (700 s). (c) Saturated area percentage with time. Insert is the saturated area (red ring) at initial saturation time (700 s). (d) Total NaCl flux at initial saturation time (700 s). Inserts are the convective and diffusive flux magnitudes at 700 s.

7.5 Water distribution for larger area evaporation

In theory, if the saltwater supply is sufficient, central saltwater supply would accumulate the salt at the edge of the evaporation surface in regardless of the surface diameter. However, it is not easy to uniformly distribute the saltwater on the whole surface. Larger evaporation surface requires faster water supply rate to keep up the evaporation rate, e.g. the average flow rate on the 3 cm surface is 0.0229 mm/s and that of the 11 cm case reaches 0.0937 mm/s from the simulation. Water cannot be easily transported to the surface edge in time by capillary force. Increasing the top central water supply can only make the water flow to one side edge in a path of least resistance, leaving the other side covered by salt gradually (11 cm in diameter, Figure 7.5a). The average surface temperature reached 36.7 ºC with the hottest point of 53.1 ºC at 4 h.

To solve the water non-uniform distribution and inefficient water transport to the edge, a radial arterial water distribution system was designed. It consists of 6 radial branches, which are made of airlaid paper and also coated by polypyrrole. Due to the additional better water transport of the airlaid paper and the water flow between the evaporation surface and the airlaid paper driven by capillary force, water first quickly runs to the edge through the branches and then wets all the remaining surface at the saltwater supply rate of 0.1650 ml/min (i.e. 1.04 $kg \cdot m^{-2} \cdot h^{-1}$, Figure 7.5b). The radial arterial water distribution system solves the water inefficient distribution problem, while it accumulates the salt on the surface in parts instead of at the edge (Figure 7.5c, d). Salt accumulated on the surface cannot fall down automatically for harvesting. At the same time, the surface average temperature also increased from 32.1 to 35.9 ºC, and the hottest point increased more obviously from 36.9 to 51.8 ºC, indicating that the efficiency is decreasing.

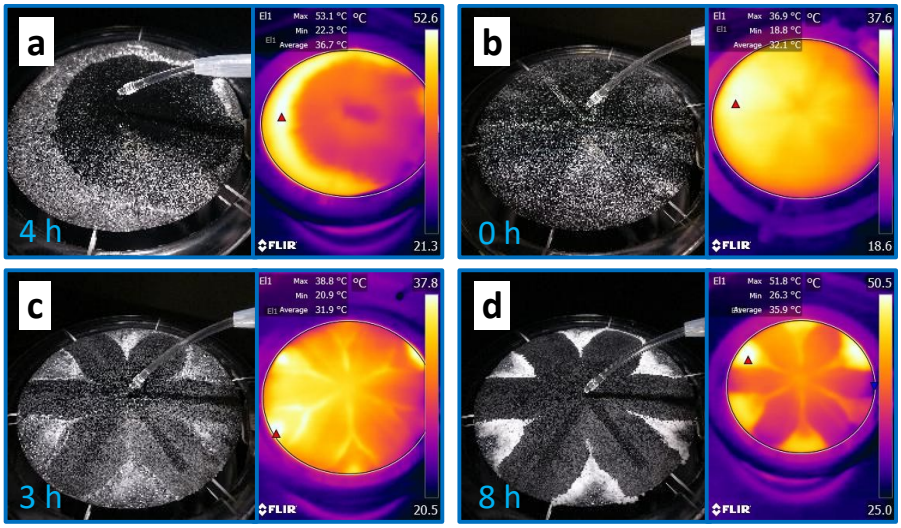

Figure 7.5 Saltwater (3.5 wt% NaCl solution) evaporation and salt distribution on larger evaporation surfaces (11 cm in diameter). (a) Saltwater evaporation. (b-d) Saltwater evaporation and salt distribution with a radial arterial water distribution system at the saltwater supply rate of 0.1650 ml/min (i.e. 1.04 $kg \cdot m^{-2} \cdot h^{-1}$) at 0 h, 3 h and 8 h respectively.

To solve the salt accumulation on the surface problem, the salt distribution on the evaporation surface with the radial arterial water distribution system was simulated. To ensure a sufficient water supply in the distribution system, the permeability (κ) of the distribution system was set 100 times that of the evaporation surface. The water transport system changed the original water

supply way and the water supply in the radial branches is obviously faster than the remaining surface (Figure 7.6a). The parts far from the center and the radial branches have the slowest water supply rate. It only takes 70 s to reach initial saturation for this larger evaporation surface (11cm in diameter and 700 s for the 3 cm case above, Figure 7.6b). The saturated area is the same area with the slowest water supply rate (Figure 7.6c), and the simulation result agrees well with the experiment result in Figure 7.5d. To make the salt accumulate at the edge for automatic falling, the saturated area (16.4%) was cut out to create a floriform evaporation surface (Figure 7.6d). The salt only accumulates at the edge, leaving the main surface at a low concentration for evaporation (Figure 7.6e). The saturated area at the edge makes it possible for the accumulated salt to fall down (Figure 7.6f).

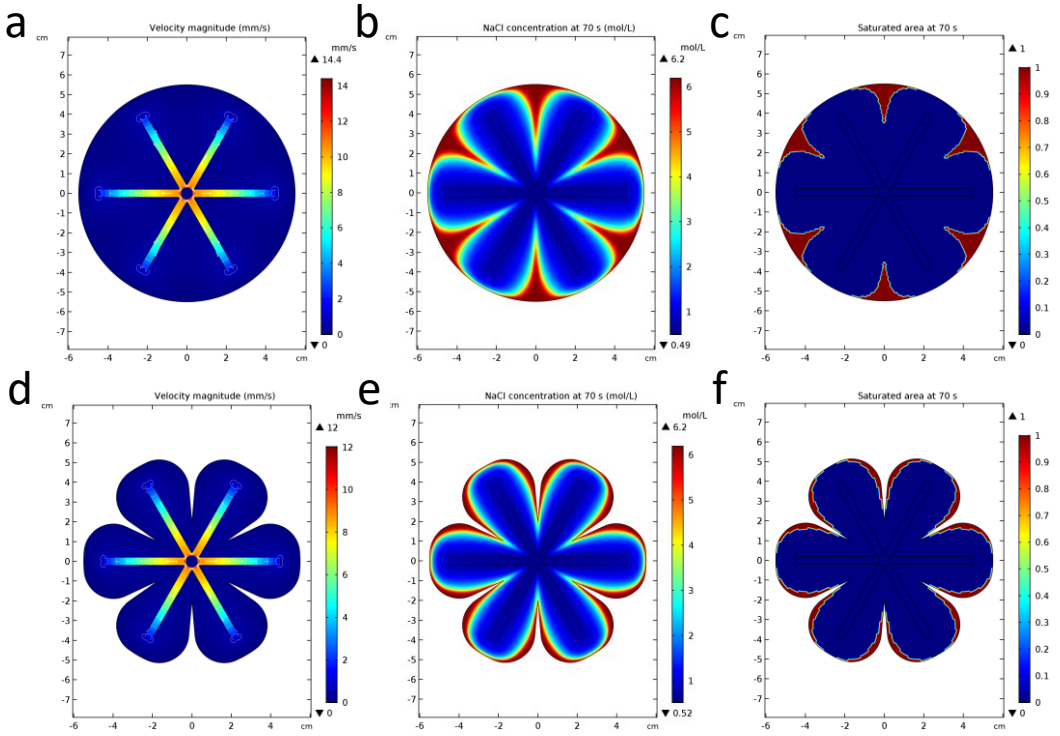

Figure 7.6 Simulations of salt distribution on the evaporation surfaces (11 cm in diameter) with radical water transport artery system. (a) Velocity magnitude. (b) NaCl concentration at initial saturation time (70 s). (c) Saturated area at initial saturation time. (d) Velocity magnitude of the floriform surface. (e) NaCl concentration at initial saturation time (70 s) of the floriform surface. (f) Saturated area at initial saturation time of the floriform surface.

Based on the simulation, a floriform evaporator was designed and the salt water (3.5 wt% NaCl solution) evaporation experiments (11 cm in diameter)

were performed. The experiment results agree well with the simulation results (Figure 7.7a-e). Salts only accumulate at the edge and fall automatically for harvesting. The evaporation continuously ran for 70 h at the evaporation rate of 0.1650 ml/min (i.e. 1.04 $kg \cdot m^{-2} \cdot h^{-1}$ based on the complete circle area, and 1.24 $kg \cdot m^{-2} \cdot h^{-1}$ based on the actual surface area), which is the same as the uncut surface. This is due to both the robustness of the evaporator and the influence of the salt accumulation on the uncut surface. The harvested salts in 70 h are shown in Figure 7.7f.

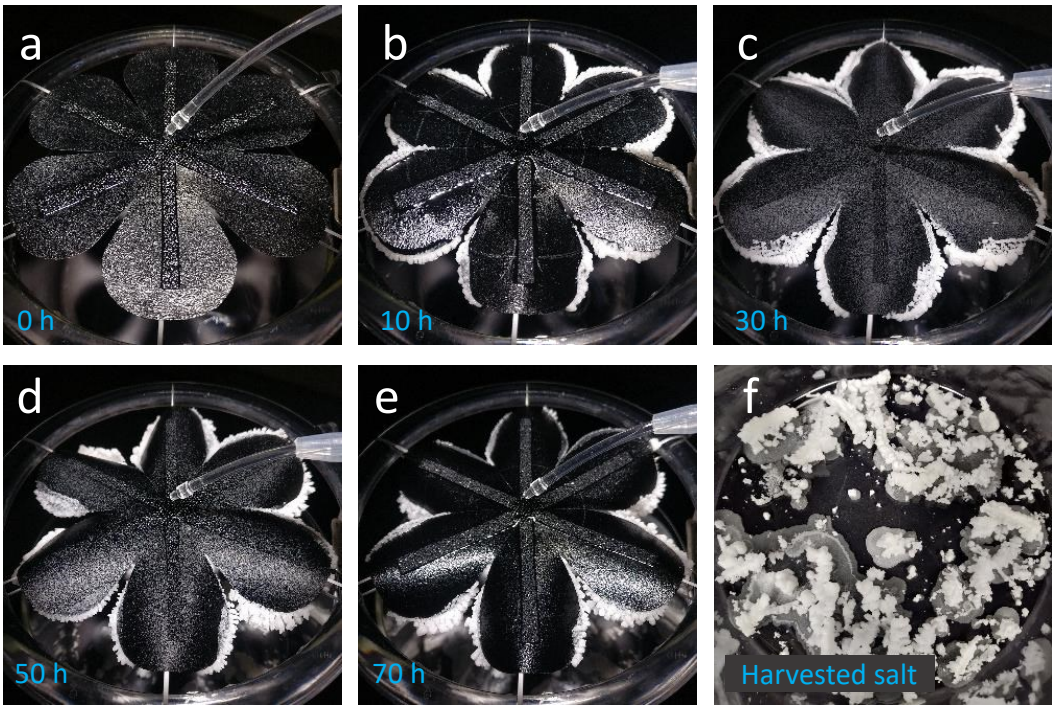

Figure 7.7 Saltwater evaporation and salt harvesting from the floriform evaporation surface (11 cm in diameter). (a-e) Saltwater evaporation at 0.1650 ml/min and salt harvesting at 0, 10, 30, 50 and 70 h respectively. (f) Harvested salt at 70 h.

7.6 Chapter summary

Here, a double-sided suspending evaporator with top water supply and surface water distribution systems was demonstrated for solar evaporation and salt harvesting concurrently. This design discards the thermal insulation layer and the water transport pillar, and achieves efficient vapour generation via double-sided evaporation with no heat loss to the bulk water. Top water supply is able to supply sufficient water to the evaporation surface for its larger area application. The evaporation rate (3 cm in diameter case) reached 1.40 $kg \cdot m^{-2} \cdot h^{-1}$ under 1 sun (1 kW/m^2), whose corresponding energy conversion efficiency is 95.7%, with a remarkable low surface average temperature of 28.2 ºC. By both simulations and experiments, a radial arterial water distribution system on the evaporation surface was designed to efficiently distribute the water on the larger evaporation surface (11 cm in diameter). By cutting out the salt accumulation area (16.4%) on the surface with the radial arterial water distribution system, salt accumulates at the edge again. 70 h continuous solar evaporation was achieved with salt harvesting at 1.04 $kg \cdot m^{-2} \cdot h^{-1}$ (based on the complete circle area with 11 cm in diameter) on the floriform evaporation surface. This work provides new ideas for the structural design of solar evaporators and advances a step closer to the large area application of the efficient double-sided evaporator.

Chapter 8
Conclusions and suggestions for future work

8.1 Conclusions

This work demonstrated high-efficient solar evaporators that achieve continuous solar vapour generation and salt harvesting from seawater concurrently, with improved salt harvesting mechanism understanding. Primarily four parts were focused: i) light-trapping photothermal material development, ii) evaporator structure improvement for continuous concurrent solar vapour generation and salt harvesting, iii) salt harvesting mechanism understanding improvement, and iv) scale-up of the evaporator for large evaporation surface area applications. The conclusions are reached as below.

First, a high efficient fibrous polypyrrole-dopamine photothermal material with light-trapping properties was developed. This nanofiber coating can be directly synthesized without using any prepared template as the substrate by ultrasonic spray coating and can be easily coated on various substrates at room temperature rapidly. The surface structure can be tuned by simply using APS as oxidant to obtain a granular structure, or using SDBS as surfactant to obtain plane-fibrous or plane-granular composite structures. This nanofiber coating has excellent water spreading for water transportation. The special light-trapping design at the nanoscale promotes multiple reflections and significantly improves the solar absorption at different incidence angles across the full solar spectrum. The highest solar absorptance reached 97.73%. It was then coated on a polystyrene foam to make an interfacial evaporator. The water transport layer was integrated into the solar absorbing layer due to its excellent water transportation. To ensure enough water supply to keep up with solar evaporation on a large surface, a cross-shaped water transport tape was applied on the evaporation surface. This evaporator achieved a highest solar-to-thermal conversion efficiency of 95.8% at the evaporation rate of 1.385 $kg \cdot m^{-2} \cdot h^{-1}$ under 1 sun. When applied on salt water, this solar evaporator achieved self-cleaning by salt back diffusion in absence of solar irradiation.

Then a central water supply umbrella evaporator (UE) was proposed, which achieves high efficiencies of continuous fresh water production and salt

harvesting concurrently. Its structural advantages over a typical interfacial evaporator (IE) were proved by both experiments and simulations, which owns to its double-sided evaporation feature, leading to a higher evaporation rate, i.e. 13.6% increase under 1 sun, and a higher energy efficiency. In dark evaporation, due to double-sided heat gaining from the environment and double-sided vapour diffusion, the UE has a remarkable 72% higher evaporation rate (0.31 $kg \cdot m^{-2} \cdot h^{-1}$) than the IE (0.18 $kg \cdot m^{-2} \cdot h^{-1}$). Lower ambient temperature, lower humidity, lower bulk water temperature, lower evaporation surface solar absorptance, and larger evaporation surface diameter all decrease the energy conversion efficiency of the system. Specially for UE, lower evaporation surface height would affect the back vapour diffusion. At the same vertical projection area, a larger opening angle enhances the back diffusion especially when the opening angle is above 105º. Smaller or larger opening angles leads to a larger surface area. A flat evaporation surface reaches the highest evaporation rate per unit surface area.

Benefiting from the rational design, salt will fall down automatically from the edge by gravity. The salt accumulation and falling behaviours were explored from macroscale to microscale, and notably the salt nucleation, growth, and falling mechanisms were also proposed. The UE is capable of harvesting salt from saline water containing up to 7 wt%. Salt precipitation on the evaporation surface is a dynamic equilibrium of crystallization and dissolution, in which way salt moves to the edge. The mobility of the salt determines if the salt can accumulate at the edge to fall. Insufficient water supply, high salinity, and the presentation of Mg^{2+} (especially) and Ca^{2+} will all reduce the salt mobility to make the salt gradually precipitate to the centre. The salt on the edge grows from the front by wicking the water through its porous structures inside and falls due to the dissolution of its connecting parts. By removing Mg^{2+} and Ca^{2+} through sedimentations, continuous solar vapour generation was achieved with salt harvesting from real seawater for 100 h. Finally, a facile method was further proposed to determine the water quality for salt harvesting by simply dipping a drop on a glass slide to observe the salt creeping behaviours. The more obvious the salt creeping phenomenon, the easier it is for the salt to fall for harvesting.

To address the water supply and distribution problems of the evaporators, a suspending evaporator with top water supply and surface water distribution systems was developed. This design discards the thermal insulation layer and the water transport pillar, and achieves efficient vapour generation via double-sided evaporation with no heat loss to the bulk water. Top water supply is able to supply sufficient water to the evaporation surface for its larger area application. The evaporation rate (3 cm in diameter case) reached 1.40 $kg \cdot m^{-2} \cdot h^{-1}$ under 1 sun (energy efficiency 95.7%) with a remarkable low surface average temperature of 28.2 ºC. By both simulations and experiments, a radial arterial water distribution system on the evaporation surface was designed to efficiently distribute the water on the larger evaporation surface (11 cm in diameter). By cutting out the salt accumulation area (16.4%) on the surface with the radial arterial water distribution system, salt accumulates at the edge again. 70 h continuous solar evaporation with salt harvesting was achieved at 1.04 $kg \cdot m^{-2} \cdot h^{-1}$ on the floriform evaporation surface.

This work shows great potential of the fibrous polypyrrole-dopamine light-trapping coating as photothermal materials for solar vapour generation, provides new ideas for the structure design of the continuous evaporators that achieve solar vapour generation and salt harvesting concurrently, and allows us to better understand and control the salt harvesting process.

8.2 Suggestions for future work

In this work, fibrous polypyrrole-dopamine photothermal material was explored and applied on an interfacial evaporator. An umbrella evaporator was proposed to achieve high-efficient continuous solar vapour generation and salt harvesting concurrently. To solve the water supply problem for large area application, top water supply and water distribution systems were designed for a suspending evaporator. All the evaporators work well at the laboratory scale. However, for real applications, some future works are suggested as follows:

- The material degradation problem should be analysed in real seawater and under natural sunlight irradiation in a long-term test for real application, as pure DI water and simulated sunlight environment is relatively stable. Real seawater containing all kinds of inorganic salts and even organics is more corrosive. The life cycle of the material should also be further analysed to evaluate its application possibilities.
- Low-cost, durable and sustainable photothermal materials with light-trapping and salt-resisting microstructures should be further developed. Light-trapping structures would help further improve the solar absorptance of the materials itself and salt-resisting structures would reduce the salt load on the evaporators.
- The water supply rate should match the evaporation rate. The water transport properties of the material limit the scale-up of the evaporators. Developing more hydrophilic materials with faster water transport porous structures would help supply more water for larger evaporators.
- At present, most research mainly focus on the solar evaporation part. However, the water vapour condensing and collecting process is equally important for solar fresh water production. The vapour condensing and collecting process should be studied from system structure design to efficiency improvement methods.
- High-efficient solar evaporation mainly produces low-temperature vapour, which is slightly higher than the environment temperature and difficult to condense. Efficient cold vapour collection method should be developed for higher efficiency, e.g. vapour absorption by porous materials.

Alternatively, the evaporation temperature should be optimized for the whole process from evaporation to condensation.

- At present, even adopting top water supply with water distribution system, the evaporation surface size is still limited due to the water transport by capillary force of the surface. Therefore, a larger solar evaporator which gets rid of capillary force should be considered for large scale solar desalination and salt harvesting system.
- Water evaporation consumes much energy known as enthalpy of vaporization, however, when the vapour is condensed, it gives the energy back. Collecting the condensation latent heat back for the evaporation would break the theoretical energy efficiency limit (100%) of the evaporation process.
- In real seawater, Ca^{2+} and Mg^{2+} affect the continuous operation of the umbrella evaporator, which should be removed during the pre-treating procedure. Developing economical and sustainable methods to remove these ions or developing some additives to eliminate their affections would lower the pre-treating fees or simplify the pre-treating procedures to make the whole process more economical.
- For the continuous solar evaporation and salt harvesting from seawater, current separation method requires pre-treatment of seawater to remove Ca^{2+} and Mg^{2+} ions. Developing a continuous solar water and salt separator which does not require pre-treatment procedures would simplify the whole process and make this solar desalination and salt harvesting technology more competitive.

List of references

[1] C.A. Schlosser, K. Strzepek, X. Gao, C. Fant, E. Blanc, S. Paltsev, H. Jacoby, J. Reilly, A. Gueneau, The future of global water stress: An integrated assessment, Earths Future 2 (2014) 341-361.
[2] M.A. Shannon, P.W. Bohn, M. Elimelech, J.G. Georgiadis, B.J. Marinas, A.M. Mayes, Science and Technology for Water Purification in the Coming Decades, Nature 452 (2008) 301-310.
[3] F. Zhao, Y. Guo, X. Zhou, W. Shi, G. Yu, Materials for Solar-Powered Water Evaporation, Nat. Rev. Mater. 5 (2020) 388-401.
[4] H.C. Jin, G.P. Lin, L.Z. Bai, A. Zeiny, D.S. Wen, Steam Generation in a Nanoparticle-Based Solar Receiver, Nano Energy 28 (2016) 397-406.
[5] Y. Tian, C.Y. Zhao, A Review of Solar Collectors and Thermal Energy Storage in Solar Thermal Applications, Appl. Energy 104 (2013) 538-553.
[6] L. Zhou, Y. Tan, J. Wang, W. Xu, Y. Yuan, W. Cai, S. Zhu, J. Zhu, 3D Self-Assembly of Aluminium Nanoparticles for Plasmon-Enhanced Solar Desalination, Nat. Photonics 10 (2016) 393-398.
[7] X. Li, C. Guan, X. Gao, X. Zuo, W. Yang, H. Yan, M. Shi, H. Li, M. Sain, High Efficiency Solar Membranes Structurally Designed with 3D Core-2D Shell SiO2@Amino-Carbon Hybrid Advanced Composite for Facile Steam Generation, ACS Appl. Mater. Inter. 12 (2020) 35493-35501.
[8] P.S. Goh, Y.Y. Liang, A.F. Ismail, Energy Efficient Seawater Desalination: Strategies and Opportunities, Energy Technology 9 (2021).
[9] Y. Cohen, R. Semiat, A. Rahardianto, A perspective on reverse osmosis water desalination: Quest for sustainability, AIChE J. 63 (2017) 1771-1784.
[10] A.J. Toth, Modelling and Optimisation of Multi-Stage Flash Distillation and Reverse Osmosis for Desalination of Saline Process Wastewater Sources, Membranes 10 (2020).
[11] H. Baig, M.A. Antar, S.M. Zubair, Performance characteristics of a once-through multi-stage flash distillation process, Desalination and Water Treatment 13 (2010) 174-185.
[12] A. Al-Karaghouli, L.L. Kazmerski, Energy consumption and water production cost of conventional and renewable-energy-powered desalination processes, Renewable & Sustainable Energy Reviews 24 (2013) 343-356.
[13] D.C. Alarcon-Padilla, L. Garcia-Rodriguez, J. Blanco-Galvez, Assessment of an absorption heat pump coupled to a multi-effect distillation unit within AQUASOL project, Desalination 212 (2007) 303-310.
[14] E. Ali, J. Orfi, H. AlAnsary, S. Soukane, H. Elcik, A. Alpatova, N. Ghaffour, Cost analysis of multiple effect evaporation and membrane distillation hybrid desalination system, Desalination 517 (2021).
[15] E.J. Okampo, N. Nwulu, Optimisation of renewable energy powered reverse osmosis desalination systems: A state-of-the-art review, Renewable & Sustainable Energy Reviews 140 (2021).
[16] S.M. Shalaby, S.W. Sharshir, A.E. Kabeel, A.W. Kandeal, H.F. Abosheiasha, M. Abdelgaied, M.H. Hamed, N.U. Yang, Reverse osmosis desalination systems powered by solar energy: Preheating techniques and brine disposal challenges - A detailed review, Energy Convers. Manage. 251 (2022).
[17] B.D. Coday, P. Xu, E.G. Beaudry, J. Herron, K. Lampi, N.T. Hancock, T.Y. Cath, The sweet spot of forward osmosis: Treatment of produced water,

drilling wastewater, and other complex and difficult liquid streams, Desalination 333 (2014) 23-35.
[18] A. Altaee, G. Zaragoza, H.R. van Tonningen, Comparison between Forward Osmosis-Reverse Osmosis and Reverse Osmosis processes for seawater desalination, Desalination 336 (2014) 50-57.
[19] R.W. Field, J.J. Wu, Mass transfer limitations in forward osmosis: Are some potential applications overhyped?, Desalination 318 (2013) 118-124.
[20] S.F. Zhao, L. Zou, C.Y.Y. Tang, D. Mulcahy, Recent developments in forward osmosis: Opportunities and challenges, J. Membr. Sci. 396 (2012) 1-21.
[21] R.L. McGinnis, M. Elimelech, Energy requirements of ammonia-carbon dioxide forward osmosis desalination, Desalination 207 (2007) 370-382.
[22] M. Elimelech, W.A. Phillip, The Future of Seawater Desalination: Energy, Technology, and the Environment, Science 333 (2011) 712-717.
[23] T.Y. Cath, A.E. Childress, M. Elimelech, Forward osmosis: Principles, applications, and recent developments, J. Membr. Sci. 281 (2006) 70-87.
[24] Y.F. Cai, W.M. Shen, J. Wei, T.H. Chong, R. Wang, W.B. Krantz, A.G. Fane, X. Hu, Energy-efficient desalination by forward osmosis using responsive ionic liquid draw solutes, Environmental Science-Water Research & Technology 1 (2015) 341-347.
[25] Y.F. Cai, X. Hu, A critical review on draw solutes development for forward osmosis, Desalination 391 (2016) 16-29.
[26] P. Compain, Solar Energy for Water desalination, 1st International Symposium on Innovation and Technology in the Phosphate Industry (SYMPHOS)OCP, Marrakesh, MOROCCO, 2011, pp. 220-227.
[27] M. Thomson, D. Infield, A photovoltaic-powered seawater reverse-osmosis system without batteries, Desalination 153 (2003) 1-8.
[28] X.L. Fan, H.L. Liu, Y.T. Gao, Z. Zou, V.S.J. Craig, G.Z. Zhang, G.M. Liu, Forward-Osmosis Desalination with Poly(Ionic Liquid) Hydrogels as Smart Draw Agents, Adv. Mater. 28 (2016) 4156-4161.
[29] Y.J. Zhong, X.S. Feng, W. Chen, X.B. Wang, K.W. Huang, Y. Gnanou, Z.P. Lai, Using UCST Ionic Liquid as a Draw Solute in Forward Osmosis to Treat High-Salinity Water, Environ. Sci. Technol. 50 (2016) 1039-1045.
[30] M. Amjad, J. Gardy, A. Hassanpour, D.S. Wen, Novel draw solution for forward osmosis based solar desalination, Appl. Energy 230 (2018) 220-231.
[31] F. Zhao, X.Y. Zhou, Y. Shi, X. Qian, M. Alexander, X.P. Zhao, S. Mendez, R.G. Yang, L.T. Qu, G.H. Yu, Highly efficient solar vapour generation via hierarchically nanostructured gels, Nature Nanotechnology 13 (2018) 489.
[32] Y.L. Wang, H. Liu, C.J. Chen, Y.D. Kuang, J.W. Song, H. Xie, C. Jia, S. Kronthal, X. Xu, S.M. He, L.B. Hu, All Natural, High Efficient Groundwater Extraction via Solar Steam/Vapor Generation, Adv. Sustain. Syst. 3 (2019).
[33] M. Thirugnanasambandam, S. Iniyan, R. Goic, A review of solar thermal technologies, Renewable & Sustainable Energy Reviews 14 (2010) 312-322.
[34] A. Raza, J.Y. Lu, S. Alzaim, H.X. Li, T.J. Zhang, Novel Receiver-Enhanced Solar Vapor Generation: Review and Perspectives, Energies 11 (2018).
[35] N.S. Lewis, Toward cost-effective solar energy use, Science 315 (2007) 798-801.
[36] E. Kabir, P. Kumar, S. Kumar, A.A. Adelodun, K.H. Kim, Solar energy: Potential and future prospects, Renewable & Sustainable Energy Reviews 82 (2018) 894-900.

[37] K.Q. Peng, S.T. Lee, Silicon Nanowires for Photovoltaic Solar Energy Conversion, Adv. Mater. 23 (2011) 198-215.
[38] N.J. Jeon, J. Lee, J.H. Noh, M.K. Nazeeruddin, M. Gratzel, S.I. Seok, Efficient Inorganic Organic Hybrid Perovskite Solar Cells Based on Pyrene Arylamine Derivatives as Hole-Transporting Materials, J. Am. Chem. Soc. 135 (2013) 19087-19090.
[39] M.A. Green, A. Ho-Baillie, H.J. Snaith, The emergence of perovskite solar cells, Nat. Photonics 8 (2014) 506-514.
[40] F.H. Alharbi, S. Kais, Theoretical limits of photovoltaics efficiency and possible improvements by intuitive approaches learned from photosynthesis and quantum coherence, Renewable & Sustainable Energy Reviews 43 (2015) 1073-1089.
[41] L. Kazmerski, Best Research-Cell Efficiencies, 2018.
[42] H. Ghasemi, G. Ni, A.M. Marconnet, J. Loomis, S. Yerci, N. Miljkovic, G. Chen, Solar Steam Generation by Heat Localization, Nat. Commun. 5 (2014) 4449-4455.
[43] O. Neumann, C. Feronti, A.D. Neumann, A.J. Dong, K. Schell, B. Lu, E. Kim, M. Quinn, S. Thompson, N. Grady, P. Nordlander, M. Oden, N.J. Halas, Compact solar autoclave based on steam generation using broadband light-harvesting nanoparticles, Proc. Natl. Acad. Sci. U. S. A. 110 (2013) 11677-11681.
[44] S. Youcef-Ali, J.Y. Desmons, Influence of the aerothermic parameters and the product quantity on the production capacity of an indirect solar dryer, Renewable Energy 32 (2007) 496-511.
[45] K. Schwarzer, M.E.V. da Silva, Characterisation and design methods of solar cookers, Solar Energy 82 (2008) 157-163.
[46] S.D. Pohekar, D. Kumar, M. Ramachandran, Dissemination of cooking energy alternatives in India - a review, Renewable & Sustainable Energy Reviews 9 (2005) 379-393.
[47] S. Karsli, Performance analysis of new-design solar air collectors for drying applications, Renewable Energy 32 (2007) 1645-1660.
[48] J.M. Chang, M.C. Shen, B.J. Huang, A criterion study of solar irradiation patterns for the performance testing of thermosyphon solar water heaters, Solar Energy 73 (2002) 287-292.
[49] S.L. Abreu, S. Colle, An experimental study of two-phase closed thermosyphons for compact solar domestic hot-water systems, Solar Energy 76 (2004) 141-145.
[50] L.Z. Ren, X.G. Zhao, Y.Z. Zhang, Y.B. Li, The economic performance of concentrated solar power industry in China, Journal of Cleaner Production 205 (2018) 799-813.
[51] M.J. Wagner, W.T. Hamilton, A. Newman, J. Dent, C. Diep, R. Braun, Optimizing dispatch for a concentrated solar power tower, Solar Energy 174 (2018) 1198-1211.
[52] Y.W. Hu, Y.R. He, Z.D. Zhang, D.S. Wen, Effect of Al2O3 nanoparticle dispersion on the specific heat capacity of a eutectic binary nitrate salt for solar power applications, Energy Convers. Manage. 142 (2017) 366-373.
[53] A. Kasaeian, G. Nouri, P. Ranjbaran, D.S. Wen, Solar collectors and photovoltaics as combined heat and power systems: A critical review, Energy Convers. Manage. 156 (2018) 688-705.

[54] A. Guo, X. Ming, Y. Fu, G. Wang, X. Wang, Fiber-Based, Double-Sided, Reduced Graphene Oxide Films for Efficient Solar Vapor Generation, ACS Appl. Mater. Inter. 9 (2017) 29958-29964.
[55] O. Neumann, A.D. Neumann, E. Silva, C. Ayala-Orozco, S. Tian, P. Nordlander, N.J. Halas, Nanoparticle-Mediated, Light-Induced Phase Separations, Nano Lett. 15 (2015) 7880-7885.
[56] X.F. Lin, J.Y. Chen, Z.K. Yuan, M.J. Yang, G.J. Chen, D.S. Yu, M.Q. Zhang, W. Hong, X.D. Chen, Integrative solar absorbers for highly efficient solar steam generation, J. Mater. Chem. A 6 (2018) 4642-4648.
[57] J. Wang, Y. Li, L. Deng, N. Wei, Y. Weng, S. Dong, D. Qi, J. Qiu, X. Chen, T. Wu, High-Performance Photothermal Conversion of Narrow-Bandgap Ti2 O3 Nanoparticles, Adv. Mater. 29 (2017) 1603730-1603735.
[58] P. Tao, G. Ni, C. Song, W. Shang, J. Wu, J. Zhu, G. Chen, T. Deng, Solar-Driven Interfacial Evaporation, Nat. Energy 3 (2018) 1031-1041.
[59] S.T. Yu, Y. Zhang, H.Z. Duan, Y.M. Liu, X.J. Quan, P. Tao, W. Shang, J.B. Wu, C.Y. Song, T. Deng, The impact of surface chemistry on the performance of localized solar-driven evaporation system, Sci. Rep. 5 (2015).
[60] J. Zhou, Y. Gu, Z. Deng, L. Miao, H. Su, P. Wang, J. Shi, The Dispersion of Au Nanorods Decorated on Graphene Oxide Nanosheets for Solar Steam Generation, Sustain. Mater. Techno. 19 (2019) 842-850.
[61] A. Zeiny, H.C. Jin, L.Z. Bai, G.P. Lin, D.S. Wen, A comparative study of direct absorption nanofluids for solar thermal applications, Solar Energy 161 (2018) 74-82.
[62] J. Fang, Q.L. Liu, W. Zhang, J.J. Gu, Y.S. Su, H.L. Su, C.P. Guo, D. Zhang, Ag/diatomite for highly efficient solar vapor generation under one-sun irradiation, J. Mater. Chem. A 5 (2017) 17817-17821.
[63] F. Noor, A. Vorozhtsov, M. Lerner, E.P. Bandarra Filho, D. Wen, Thermal-Chemical Characteristics of Al–Cu Alloy Nanoparticles, J. Phys. Chem. C 119 (2015) 14001-14009.
[64] L. Shi, Y.R. He, Y.M. Huang, B.C. Jiang, Recyclable Fe3O4@CNT nanoparticles for high-efficiency solar vapor generation, Energy Convers. Manage. 149 (2017) 401-408.
[65] S. Wu, C.H. Cheng, Y.J. Hsiao, R.C. Juang, W.F. Wen, Fe2O3 films on stainless steel for solar absorbers, Renewable & Sustainable Energy Reviews 58 (2016) 574-580.
[66] D. Jeong, J. Lee, H. Hong, D. Choi, J.-W. Cho, S.-K. Kim, Y. Nam, Absorption Mechanism and Performance Characterization of CuO Nanostructured Absorbers, Sol. Energy Mater. Sol. Cells 169 (2017) 270-279.
[67] L. Zhu, L. Sun, H. Zhang, D.F. Yu, H. Aslan, J.G. Zhao, Z.L. Li, M. Yu, F. Besenbacher, Y. Sun, Dual-phase molybdenum nitride nanorambutans for solar steam generation under one sun illumination, Nano Energy 57 (2019) 842-850.
[68] G.H. Liu, J.L. Xu, K.Y. Wang, Solar water evaporation by black photothermal sheets, Nano Energy 41 (2017) 269-284.
[69] Y. Ito, Y. Tanabe, J. Han, T. Fujita, K. Tanigaki, M. Chen, Multifunctional Porous Graphene for High-Efficiency Steam Generation by Heat Localization, Adv. Mater. 27 (2015) 4302-4307.
[70] Y.M. Liu, J.W. Chen, D.W. Guo, M.Y. Cao, L. Jiang, Floatable, Self-Cleaning, and Carbon-Black-Based Superhydrophobic Gauze for the Solar Evaporation Enhancement at the Air-Water Interface, ACS Appl. Mater. Inter. 7 (2015) 13645-13652.

[71] J.J. Wang, Z.H. Liu, X.L. Dong, C.E. Hsiung, Y.H. Zhu, L.M. Liu, Y. Han, Microporous cokes formed in zeolite catalysts enable efficient solar evaporation, J. Mater. Chem. A 5 (2017) 6860-6865.
[72] O. Neumann, A.S. Urban, J. Day, S. Lal, P. Nordlander, N.J. Halas, Solar Vapor Generation Enabled by Nanoparticles, Acs Nano 7 (2013) 42-49.
[73] Y. Wang, L. Zhang, P. Wang, Self-Floating Carbon Nanotube Membrane on Macroporous Silica Substrate for Highly Efficient Solar-Driven Interfacial Water Evaporation, ACS Sustain. Chem. Eng. 4 (2016) 1223-1230.
[74] L. Gao, G.X. Ni, Y. Liu, B. Liu, A.H. Castro Neto, K.P. Loh, Face-to-face Transfer of Wafer-Scale Graphene Films, Nature 505 (2014) 190-194.
[75] L. Shi, Y. Wang, L. Zhang, P. Wang, Rational Design of a Bi-Layered Reduced Graphene Oxide Film on Polystyrene Foam for Solar-Driven Interfacial Water Evaporation, J. Mater. Chem. A 5 (2017) 16212-16219.
[76] G.J. Li, W.C. Law, K.C. Chan, Floating, Highly Efficient, and Scalable Graphene Membranes for Seawater Desalination Using Solar Energy, Green Chem. 20 (2018) 3689-3695.
[77] J.U. Kim, S. Lee, S.J. Kang, T.I. Kim, Materials and Design of Nanostructured Broadband Light Absorbers for Advanced Light-to-Heat Conversion, Nanoscale 10 (2018) 21555-21574.
[78] X. Wu, G.Y. Chen, W. Zhang, X. Liu, H. Xu, A Plant-Transpiration-Process-Inspired Strategy for Highly Efficient Solar Evaporation, Adv. Sustain. Syst. 1 (2017) 1700046-1700052.
[79] X.Y. Huang, Y.H. Yu, O.L. de Llergo, S.M. Marquez, Z.D. Cheng, Facile polypyrrole thin film coating on polypropylene membrane for efficient solar-driven interfacial water evaporation, RSC Adv. 7 (2017) 9495-9499.
[80] H.H. Wang, C.F. Guo, S.L. Zhou, X. Hu, Y. Hu, F.F. Li, Y.G. Miao, One-step synthesis and self-organization of polypyrrole ultrathin films inlayed with Prussian blue nanoparticles induced by a drop of toluene solution on water surface, Thin Solid Films 520 (2012) 2026-2031.
[81] S.R. Yun, G.O. Kim, C.W. Lee, N.J. Jo, Y. Kang, K.S. Ryu, Synthesis and Control of the Shell Thickness of Polyaniline and Polypyrrole Half Hollow Spheres Using the Polystyrene Cores, Journal of Nanomaterials (2012).
[82] D. Hao, Y. Yang, B. Xu, Z. Cai, Efficient Solar Water Vapor Generation Enabled by Water-Absorbing Polypyrrole Coated Cotton Fabric with Enhanced Heat Localization, Appl. Therm. Eng. 141 (2018) 406-412.
[83] W. Zhang, F.K. Yang, Z. Pan, J. Zhang, B. Zhao, Bio-inspired Dopamine Functionalization of Polypyrrole for Improved Adhesion and Conductivity, Macromol. Rapid Commun. 35 (2014) 350-354.
[84] W. Zhang, Z. Pan, F.K. Yang, B. Zhao, A Facile In Situ Approach to Polypyrrole Functionalization Through Bioinspired Catechols, Adv. Funct. Mater. 25 (2015) 1588-1597.
[85] A.E. Kabeel, S.A. El-Agouz, Review of researches and developments on solar stills, Desalination 276 (2011) 1-12.
[86] A. Lenert, E.N. Wang, Optimization of nanofluid volumetric receivers for solar thermal energy conversion, Solar Energy 86 (2012) 253-265.
[87] F. Yu, Y.Y. Chen, X.B. Liang, J.L. Xu, C.S. Lee, Q. Liang, P. Tao, T. Deng, Dispersion stability of thermal nanofluids, Progress in Natural Science-Materials International 27 (2017) 531-542.
[88] R. Prasher, P.E. Phelan, P. Bhattacharya, Effect of aggregation kinetics on the thermal conductivity of nanoscale colloidal solutions (nanofluid), Nano Lett. 6 (2006) 1529-1534.

[89] O.A. Yeshchenko, N.V. Kutsevol, A.P. Naumenko, Light-Induced Heating of Gold Nanoparticles in Colloidal Solution: Dependence on Detuning from Surface Plasmon Resonance, Plasmonics 11 (2016) 345-350.
[90] A.G. Skirtach, C. Dejugnat, D. Braun, A.S. Susha, A.L. Rogach, W.J. Parak, H. Mohwald, G.B. Sukhorukov, The role of metal nanoparticles in remote release of encapsulated materials, Nano Lett. 5 (2005) 1371-1377.
[91] S. Lal, S.E. Clare, N.J. Halas, Nanoshell-Enabled Photothermal Cancer Therapy: Impending Clinical Impact, Acc. Chem. Res. 41 (2008) 1842-1851.
[92] D. Boyer, P. Tamarat, A. Maali, B. Lounis, M. Orrit, Photothermal imaging of nanometer-sized metal particles among scatterers, Science 297 (2002) 1160-1163.
[93] J.S. Donner, G. Baffou, D. McCloskey, R. Quidant, Plasmon-Assisted Optofluidics, Acs Nano 5 (2011) 5457-5462.
[94] X.L. Chen, A. Munjiza, K. Zhang, D.S. Wen, Molecular Dynamics Simulation of Heat Transfer from a Gold Nanoparticle to a Water Pool, J. Phys. Chem. C 118 (2014) 1285-1293.
[95] J. Lombard, T. Biben, S. Merabia, Kinetics of Nanobubble Generation Around Overheated Nanoparticles, Phys. Rev. Lett. 112 (2014).
[96] G. Ni, N. Miljkovic, H. Ghasemi, X.P. Huang, S.V. Boriskina, C.T. Lin, J.J. Wang, Y.F. Xu, M.M. Rahman, T.J. Zhang, G. Chen, Volumetric solar heating of nanofluids for direct vapor generation, Nano Energy 17 (2015) 290-301.
[97] J. Jeon, S. Park, B.J. Lee, Analysis on the performance of a flat-plate volumetric solar collector using blended plasmonic nanofluid, Solar Energy 132 (2016) 247-256.
[98] A. Zeiny, H.C. Jin, G.P. Lin, P.X. Song, D.S. Wen, Solar evaporation via nanofluids: A comparative study, Renewable Energy 122 (2018) 443-454.
[99] G. Ni, G. Li, Svetlana V. Boriskina, H. Li, W. Yang, T. Zhang, G. Chen, Steam Generation under One Sun Enabled by a Floating Structure with Thermal Concentration, Nat. Energy 1 (2016) 16126-16132.
[100] Y.C. Wang, C.Z. Wang, X.J. Song, M.H. Huang, S.K. Megarajan, S.F. Shaukat, H.Q. Jiang, Improved light-harvesting and thermal management for efficient solar-driven water evaporation using 3D photothermal cones, J. Mater. Chem. A 6 (2018) 9874-9881.
[101] Z. Wang, Y. Liu, P. Tao, Q. Shen, N. Yi, F. Zhang, Q. Liu, C. Song, D. Zhang, W. Shang, T. Deng, Bio-inspired Evaporation through Plasmonic Film of Nanoparticles at the Air-Water Interface, Small 10 (2014) 3234-3239.
[102] D.D.L. Chung, Materials for thermal conduction, Appl. Therm. Eng. 21 (2001) 1593-1605.
[103] X. Li, W. Xu, M. Tang, L. Zhou, B. Zhu, S. Zhu, J. Zhu, Graphene Oxide-Based Efficient and Scalable Solar Desalination under One Sun with a Confined 2D Water Path, Proc. Natl. Acad. Sci. U. S. A. 113 (2016) 13953-13958.
[104] J. Huang, Y.R. He, M.J. Chen, X.Z. Wang, Separating photo-thermal conversion and steam generation process for evaporation enhancement using a solar absorber, Appl. Energy 236 (2019) 244-252.
[105] J.W. Lou, Y. Liu, Z.Y. Wang, D.W. Zhao, C.Y. Song, J.B. Wu, N. Dasgupta, W. Zhang, D. Zhang, P. Tao, W. Shang, T. Deng, Bioinspired Multifunctional Paper-Based rGO Composites for Solar-Driven Clean Water Generation, ACS Appl. Mater. Inter. 8 (2016) 14628-14636.
[106] Y.X. Chen, Y.M. Shi, H. Kou, D.L. Liu, Y. Huang, Z.G. Chen, B. Zhang, Self-Floating Carbonized Tissue Membrane Derived from Commercial Facial

Tissue for Highly Efficient Solar Steam Generation, ACS Sustain. Chem. Eng. 7 (2019) 2911-2915.
[107] P. Mu, Z. Zhang, W. Bai, J.X. He, H.X. Sun, Z.Q. Zhu, W.D. Liang, A. Li, Superwetting Monolithic Hollow-Carbon-Nanotubes Aerogels with Hierarchically Nanoporous Structure for Efficient Solar Steam Generation, Adv. Energy Mater. 9 (2019).
[108] N. Xu, X.Z. Hu, W.C. Xu, X.Q. Li, L. Zhou, S.N. Zhu, J. Zhu, Mushrooms as Efficient Solar Steam-Generation Devices, Adv. Mater. 29 (2017).
[109] H.D. Liu, X.T. Zhang, Z.X. Hong, Z.G. Pu, Q.Y. Yao, J.C. Shi, G.B. Yang, B.W. Mi, B. Yang, X. Liu, H.F. Jiang, X.J. Hu, A bioinspired capillary-driven pump for solar vapor generation, Nano Energy 42 (2017) 115-121.
[110] J.G. Zhou, Z.L. Sun, M.Q. Chen, J.T. Wang, W.M. Qiao, D.H. Long, L.C. Ling, Macroscopic and Mechanically Robust Hollow Carbon Spheres with Superior Oil Adsorption and Light-to-Heat Evaporation Properties, Adv. Funct. Mater. 26 (2016) 5368-5375.
[111] Y. Zeng, J. Yao, B.A. Horri, K. Wang, Y. Wu, D. Li, H. Wang, Solar Evaporation Enhancement Using Floating Light-Absorbing Magnetic Particles, Energy Environ. Sci. 4 (2011) 4074-4078.
[112] X.Q. Li, J.L. Li, J.Y. Lu, N. Xu, C.L. Chen, X.Z. Min, B. Zhu, H.X. Li, L. Zhou, S.N. Zhu, T.J. Zhang, J. Zhu, Enhancement of Interfacial Solar Vapor Generation by Environmental Energy, Joule 2 (2018) 1331-1338.
[113] H.M. Song, Y.H. Liu, Z.J. Liu, M.H. Singer, C.Y. Li, A.R. Cheney, D.X. Ji, L. Zhou, N. Zhang, X. Zeng, Z.M. Bei, Z.F. Yu, S.H. Jiang, Q.Q. Gan, Cold Vapor Generation beyond the Input Solar Energy Limit, Advanced Science 5 (2018).
[114] Z.J. Liu, H.M. Song, D.X. Ji, C.Y. Li, A. Cheney, Y.H. Liu, N. Zhang, X. Zeng, B.R. Chen, J. Gao, Y.S. Li, X. Liu, D. Aga, S.H. Jiang, Z.F. Yu, Q.Q. Gan, Extremely Cost-Effective and Efficient Solar Vapor Generation under Nonconcentrated Illumination Using Thermally Isolated Black Paper, Global Challenges 1 (2017).
[115] K. Bae, G. Kang, S.K. Cho, W. Park, K. Kim, W.J. Padilla, Flexible thin-film black gold membranes with ultrabroadband plasmonic nanofocusing for efficient solar vapour generation, Nat. Commun. 6 (2015).
[116] Q.S. Jiang, L.M. Tian, K.K. Liu, S. Tadepalli, R. Raliya, P. Biswas, R.R. Naik, S. Singamaneni, Bilayered Biofoam for Highly Efficient Solar Steam Generation, Adv. Mater. 28 (2016) 9400-+.
[117] J. Jia, W.D. Liang, H.X. Sun, Z.Q. Zhu, C.J. Wang, A. Li, Fabrication of bilayered attapulgite for solar steam generation with high conversion efficiency, Chem. Eng. J. 361 (2019) 999-1006.
[118] D. Hao, Y. Yang, B. Xu, Z. Cai, Bifunctional Fabric with Photothermal Effect and Photocatalysis for Highly Efficient Clean Water Generation, ACS Sustain. Chem. Eng. 6 (2018) 10789-10797.
[119] Y. Xia, Y. Kang, Z.Y. Wang, S. Yuan, Y. Li, L. Gao, H.T. Wang, X.W. Zhang, Rational designs of interfacial-heating solar-thermal desalination devices: recent progress and remaining challenges, J. Mater. Chem. A 9 (2021) 6612-6633.
[120] P.F. Wang, X.Y. Wang, S.Y. Chen, J.H. Zhang, X.J. Mu, Y.L. Chen, Z.Q. Sun, A.Y. Wei, Y.Z. Tian, J.H. Zhou, X.X. Liang, L. Miao, N. Saito, Reduced Red Mud as the Solar Absorber for Solar-Driven Water Evaporation and Vapor-Electricity Generation, ACS Appl. Mater. Inter. 13 (2021) 30556-30564.

[121] Y.W. Yang, W.X. Que, J.Q. Zhao, Y. Han, M.M. Ju, X.T. Yin, Membrane assembled from anti-fouling copper-zinc-tin-selenide nanocarambolas for solar-driven interfacial water evaporation, Chem. Eng. J. 373 (2019) 955-962.
[122] V. Kashyap, A. Al-Bayati, S.M. Sajadi, P. Irajizad, S.H. Wang, H. Ghasemi, A flexible anti-clogging graphite film for scalable solar desalination by heat localization, J. Mater. Chem. A 5 (2017) 15227-15234.
[123] Y.D. Kuang, C.J. Chen, S.M. He, E.M. Hitz, Y.L. Wang, W.T. Gan, R.Y. Mi, L.B. Hu, A High-Performance Self-Regenerating Solar Evaporator for Continuous Water Desalination, Adv. Mater. 31 (2019).
[124] Q. Zhang, R. Hu, Y.L. Chen, X.F. Xiao, G.M. Zhao, H.J. Yang, J.H. Li, W.L. Xu, X.B. Wang, Banyan-inspired hierarchical evaporators for efficient solar photothermal conversion, Appl. Energy 276 (2020).
[125] G. Ni, S.H. Zandavi, S.M. Javid, S.V. Boriskina, T.A. Cooper, G. Chen, A salt-rejecting floating solar still for low-cost desalination, Energy Environ. Sci. 11 (2018) 1510-1519.
[126] W.C. Xu, X.Z. Hu, S.D. Zhuang, Y.X. Wang, X.Q. Li, L. Zhou, S.N. Zhu, J. Zhu, Flexible and Salt Resistant Janus Absorbers by Electrospinning for Stable and Efficient Solar Desalination, Adv. Energy Mater. 8 (2018).
[127] Y. Xia, Y. Li, S. Yuan, Y. Kang, M.P. Jian, Q.F. Hou, L. Gao, H.T. Wang, X.W. Zhang, A self-rotating solar evaporator for continuous and efficient desalination of hypersaline brine, J. Mater. Chem. A 8 (2020) 16212-16217.
[128] L. Wu, Z. Dong, Z. Cai, T. Ganapathy, N.X. Fang, C. Li, C. Yu, Y. Zhang, Y. Song, Highly Efficient Three-Dimensional Solar Evaporator for High Salinity Desalination by Localized Crystallization, Nat. Commun. 11 (2020) 521-532.
[129] Y. Shi, C.L. Zhang, R.Y. Li, S.F. Zhuo, Y. Jin, L. Shi, S. Hong, J. Chang, C.S. Ong, P. Wang, Solar Evaporator with Controlled Salt Precipitation for Zero Liquid Discharge Desalination, Environ. Sci. Technol. 52 (2018) 11822-11830.
[130] Y. Xia, Q.F. Hou, H. Jubaer, Y. Li, Y. Kang, S. Yuan, H.Y. Liu, M.W. Woo, L. Zhang, L. Gao, H.T. Wang, X.W. Zhang, Spatially isolating salt crystallisation from water evaporation for continuous solar steam generation and salt harvesting, Energy Environ. Sci. 12 (2019) 1840-1847.
[131] X.X. Chen, Z.Y. Wu, D.G. Lai, M. Zheng, L. Xu, J.B. Huo, Z.X. Chen, B.L. Yuan, M.L. Fu, Resilient biomass-derived hydrogel with tailored topography for highly efficient and long-term solar evaporation of high-salinity brine, J. Mater. Chem. A 8 (2020) 22645-22656.
[132] Y. Shao, J.B. Tang, N.B. Li, T.Y. Sun, L.P. Yang, D. Chen, H. Zhi, D.J. Wang, H. Liu, G.B. Xue, Designing a bioinspired synthetic tree by unidirectional freezing for simultaneous solar steam generation and salt collection, Ecomat 2 (2020) 12018.
[133] H.Y. Peng, D. Wang, S.H. Fu, Artificial transpiration with asymmetric photothermal textile for continuous solar-driven evaporation, spatial salt harvesting and electrokinetic power generation, Chem. Eng. J. 426 (2021).
[134] G. Ballard, Z.Y. Al-Saigh, Solubility and Surface Thermodynamics of Conducting Polymers by Inverse Gas Chromatography, IV: Polypyrrole/Titanium Oxide, Chromatographia 83 (2020) 451-466.
[135] A. Yussuf, M. Al-Saleh, S. Al-Enezi, G. Abraham, Synthesis and Characterization of Conductive Polypyrrole: The Influence of the Oxidants and Monomer on the Electrical, Thermal, and Morphological Properties, Int. J. Polym. Sci. 2018 (2018) 1-8.

[136] J. Yan, Y. Huang, X. Liu, X. Zhao, T. Li, Y. Zhao, P. Liu, Polypyrrole-Based Composite Materials for Electromagnetic Wave Absorption, Polym. Rev. 1 (2021) 464-687.
[137] C.P. Han, R.Y. Shi, D. Zhou, H.F. Li, L. Xu, T.F. Zhang, J.Q. Li, F.Y. Kang, G.X. Wang, B.H. Li, High-Energy and High-Power Nonaqueous Lithium-Ion Capacitors Based on Polypyrrole/Carbon Nanotube Composites as Pseudocapacitive Cathodes, ACS Appl. Mater. Inter. 11 (2019) 15646-15655.
[138] W. Yao, S.J. He, J.G. Xu, J.S. Wang, M. He, Q.F. Zhang, Y. Li, X. Xiao, Polypyrrole Nanotube Sponge Host for Stable Lithium-Metal Batteries under Lean Electrolyte Conditions, ACS Sustain. Chem. Eng. 9 (2021) 2543-2551.
[139] J. Liu, X.J. Xu, R.Z. Hu, L.C. Yang, M. Zhu, Uniform Hierarchical Fe3O4@Polypyrrole Nanocages for Superior Lithium Ion Battery Anodes, Adv. Energy Mater. 6 (2016) 1600256-1600262.
[140] C.Y. Wang, W. Zheng, Z.L. Yue, C.O. Too, G.G. Wallace, Buckled, Stretchable Polypyrrole Electrodes for Battery Applications, Adv. Mater. 23 (2011) 3580-3584.
[141] D.J. Kim, J.W. Yoon, C.S. Lee, Y.S. Bae, J.H. Kim, Covalent Organic Framework-Derived Microporous Carbon Nanoparticles Coated with Conducting Polypyrrole as an Electrochemical Capacitor, Appl. Surf. Sci. 439 (2018) 833-838.
[142] Q. Li, D. Xu, J.N. Guo, X. Ou, F. Yan, Protonated g-C3N4@Polypyrrole Derived N-doped Porous Carbon for Supercapacitors and Oxygen Electrocatalysis, Carbon 124 (2017) 599-610.
[143] D. Wang, X. Zhou, R.F. Song, C.Q. Fang, Z. Wang, C.X. Wang, Y.W. Huang, Freestanding Silver/Polypyrrole Composite Film for Multifunctional Sensor with Biomimetic Micropattern for Physiological Signals Monitoring, Chem. Eng. J. 404 (2021) 126940-126949.
[144] W. Zhang, Y. Zhou, K. Feng, J. Trinidad, A. Yu, B. Zhao, Morphologically Controlled Bioinspired Dopamine-Polypyrrole Nanostructures with Tunable Electrical Properties, Adv. Electron. Mater. 1 (2015) 1500205-1500214.
[145] X. Wang, Q. Liu, S. Wu, B. Xu, H. Xu, Multilayer Polypyrrole Nanosheets with Self-Organized Surface Structures for Flexible and Efficient Solar-Thermal Energy Conversion, Adv. Mater. 31 (2019) 1807716-1807724.
[146] A. Umer, F. Liaqat, A. Mahmood, MoO3 Nanobelts Embedded Polypyrrole/SIS Copolymer Blends for Improved Electro-Mechanical Dual Applications, Polymers 12 (2020) 353-365.
[147] M. Sharma, G.I. Waterhouse, S.W. Loader, S. Garg, D. Svirskis, High Surface Area Polypyrrole Scaffolds for Tunable Drug Delivery, Int. J. Pharm. 443 (2013) 163-168.
[148] H. Luo, C. Gu, W. Zheng, F. Dai, X. Wang, Z. Zheng, Facile Synthesis of Novel Size-Controlled Antibacterial Hybrid Spheres Using Silver Nanoparticles Loaded with Poly-dopamine Spheres, RSC Adv. 5 (2015) 13470-13477.
[149] F. Ghorbani, A. Zamanian, M. Sahranavard, Mussel-Inspired Polydopamine-Mediated Surface Modification of Freeze-Cast Poly (epsilon-caprolactone) Scaffolds for Bone Tissue Engineering Applications, Biomed. Eng.-Biomed. Te. 65 (2020) 273-287.
[150] S. Wang, J. Zhu, Y. Rao, B. Li, S. Zhao, H. Bai, J. Cui, Polydopamine Modified Graphene Oxide-TiO2 Nanofiller for Reinforcing Physical Properties

and Anticorrosion Performance of Waterborne Epoxy Coatings, Appl. Sci. 9 (2019) 3760-3777.
[151] C.M. Parnell, B.P. Chhetri, T.B. Mitchell, F. Watanabe, G. Kannarpady, A.B. RanguMagar, H. Zhou, K.M. Alghazali, A.S. Biris, A. Ghosh, Simultaneous Electrochemical Deposition of Cobalt Complex and Poly(pyrrole) Thin Films for Supercapacitor Electrodes, Sci. Rep. 9 (2019) 5650-5662.
[152] J. Tabačiarová, M. Mičušík, P. Fedorko, M. Omastová, Study of Polypyrrole Aging by XPS, FTIR and Conductivity Measurements, Polym. Degradation Stab. 120 (2015) 392-401.
[153] P. Delparastan, K.G. Malollari, H. Lee, P.B. Messersmith, Direct Evidence for the Polymeric Nature of Polydopamine, Angew. Chem. Int. Ed. Engl. 58 (2019) 1077-1082.
[154] J. Joo, J.K. Lee, J.S. Baeck, K.H. Kim, E.J. Oh, J. Epstein, Electrical, Magnetic, and Structural Properties of Chemically and Electrochemically Synthesized Polypyrroles, Synth. Met. 117 (2001) 45-51.
[155] Z. Morávková, O. Taboubi, I.M. Minisy, P. Bober, The Evolution of the Molecular Structure of Polypyrrole during Chemical Polymerization, Synth. Met. 271 (2021) 116608-116613.
[156] E. Filippidi, T.R. Cristiani, C.D. Eisenbach, J.H. Waite, J.N. Israelachvili, B.K. Ahn, M.T. Valentine, Toughening Elastomers Using Mussel-Inspired Iron-Catechol Complexes, Science 358 (2017) 502-505.
[157] C. Fan, J. Fu, W. Zhu, D.A. Wang, A Mussel-Inspired Double-Crosslinked Tissue Adhesive Intended for Internal Medical Use, Acta Biomater. 33 (2016) 51-63.
[158] S. Hong, K.Y. Kim, H.J. Wook, S.Y. Park, K.D. Lee, D.Y. Lee, H. Lee, Attenuation of the In Vivo Toxicity of Biomaterials by Polydopamine Surface Modification, Nanomedicine 6 (2011) 793-801.
[159] E. Chalmers, H. Lee, C. Zhu, X. Liu, Increasing the Conductivity and Adhesion of Polypyrrole Hydrogels with Electropolymerized Polydopamine, Chem. Mater. 32 (2019) 234-244.
[160] X. Li, G. Ni, T. Cooper, N. Xu, J. Li, L. Zhou, X. Hu, B. Zhu, P. Yao, J. Zhu, Measuring Conversion Efficiency of Solar Vapor Generation, Joule 3 (2019) 1798-1803.
[161] W. Fang, L. Zhao, H. Chen, X. He, W.X. Li, X. Du, Z.M. Sun, T. Zhang, Y. Shen, Graphene Oxide Foam Fabricated with Surfactant Foaming Method for Efficient Solar Vapor Generation, J. Mater. Sci. 54 (2019) 12782-12793.
[162] L.F. Su, Y.Y. Ning, Z.Q. Ma, Y.H. Zhang, C.L. Liu, Y.L. Zhang, L. Miao, J.H. Zhou, B. Wu, J.S. Qian, Polypyrrole-Reinforced N,S-Doping Graphene Foam for Efficient Solar Purification of Wastewater, Sol. RRL 5 (2021) 2100210-2100217.
[163] H.X. Zhang, H.L. Xie, W. Han, X. Yan, X.J. Liu, L.F. He, P. Lin, Y.Y. Xia, K. Zhang, J.A. Zapien, K.B. Yoon, Graphene Oxide-Reduced Graphene Oxide Janus Membrane for Efficient Solar Generation of Water Vapor, ACS Appl. Nano Mater. 4 (2021) 1916-1923.
[164] X.X. Guo, H. Gao, S.Y. Wang, L.F. Yin, Y.R. Dai, Scalable, Flexible and Reusable Graphene Oxide-Functionalized Electrospun Nanofibrous Membrane for Solar Photothermal Desalination, Desalination 488 (2020) 114535-114543.
[165] B.Y. Wen, X.Y. Zhang, Y.H. Yan, Y.Q. Huang, S. Lin, Y.L. Zhu, Z.P. Wang, B.H. Zhou, S.H. Yang, J. Liu, Tailoring Polypyrrole-Based Janus

Aerogel for Efficient and Stable Solar Steam Generation, Desalination 516 (2021) 115228-115237.
[166] L.K. Gong, C.Z. Li, N. Wei, J. Li, J.Y. Shen, R.Q. Xu, Q. Li, J. Tian, H.Z. Cui, Highly Efficient Solar Evaporator Based on Graphene/MoO3-x Coated Porous Nickel for Water Purification, Sep. Purif. Technol. 275 (2021) 119139-119147.
[167] K.-T. Lin, H. Lin, T. Yang, B. Jia, Structured Graphene Metamaterial Selective Absorbers for High Efficiency and Omnidirectional Solar Thermal Energy Conversion, Nat. Commun. 11 (2020) 1-10.
[168] H.X. Li, D.D. Jia, M.C. Ding, L.J. Zhou, K. Wang, J.Q. Liu, C.Y. Liu, C.W. Li, Robust 3D Graphene/Cellulose Nanocrystals Hybrid Lamella Network for Stable and Highly Efficient Solar Desalination, Sol. RRL 5 (2021) 202100317-202100327.
[169] M.L. Chen, X.K. Lin, C.G. Zeng, Q. He, Poly(p-Phenylene Benzobisoxazole) Nanofiber/Reduced Graphene Oxide Composite Aerogels Toward High-Efficiency Solar Steam Generation, Colloid Surf. A-Physicochem. Eng. Asp. 612 (2021) 125997-126005.
[170] Z. Xu, L. Zhang, L. Zhao, B. Li, B. Bhatia, C. Wang, K.L. Wilke, Y. Song, O. Labban, J.H. Lienhard, Ultrahigh-Efficiency Desalination via a Thermally-Localized Multistage Solar Still, Energy Environ. Sci. 13 (2020) 830-839.
[171] S. Patari, P.S. Mahapatra, Liquid Wicking in a Paper Strip: An Experimental and Numerical Study, Acs Omega 5 (2020) 22931-22939.
[172] Y.J. Li, T.T. Gao, Z. Yang, C.J. Chen, Y.D. Kuang, J.W. Song, C. Jia, E.M. Hitz, B. Yang, L.B. Hu, Graphene oxide-based evaporator with one-dimensional water transport enabling high-efficiency solar desalination, Nano Energy 41 (2017) 201-209.
[173] S.J. Sun, B.B. Sun, Y.M. Wang, M.F. Antwi-Afari, H.Y. Mi, Z.H. Guo, C.T. Liu, C.Y. Shen, Carbon black and polydopamine modified non-woven fabric enabling efficient solar steam generation towards seawater desalination and wastewater purification, Sep. Purif. Technol. 278 (2022) 119621.
[174] S.A. Cheng, Z. Yu, Z.F. Lin, L.X. Li, Y.H. Li, Z.Z. Mao, A lotus leaf like vertical hierarchical solar vapor generator for stable and efficient evaporation of high-salinity brine, Chem. Eng. J. 401 (2020) 126108.
[175] J. Li, X. Wang, Z. Lin, N. Xu, X. Li, J. Liang, W. Zhao, R. Lin, B. Zhu, G. Liu, Over 10 kg m− 2 h− 1 Evaporation Rate Enabled by a 3D Interconnected Porous Carbon Foam, Joule (2020).
[176] G.L. Peng, S.C. Deng, S.W. Sharshir, D.K. Ma, A.E. Kabeel, N. Yang, High efficient solar evaporation by airing multifunctional textile, Int. J. Heat Mass Transfer 147 (2020) 118866.
[177] A.K. Menon, I. Haechler, S. Kaur, S. Lubner, R.S. Prasher, Enhanced solar evaporation using a photo-thermal umbrella for wastewater management, Nature Sustainability 3 (2020) 144-+.
[178] H.Y. Peng, D. Wang, S.H. Fu, Programmable Asymmetric Nanofluidic Photothermal Textile Umbrella for Concurrent Salt Management and In Situ Power Generation During Long-Time Solar Steam Generation, ACS Appl. Mater. Inter. 13 (2021) 47549-47559.
[179] T.L. Norman, Steam-air mixture condensation in a subcooled water pool, Purdue University2007.
[180] B. Hendersonsellers, A NEW FORMULA FOR LATENT-HEAT OF VAPORIZATION OF WATER AS A FUNCTION OF TEMPERATURE, Quarterly Journal of the Royal Meteorological Society 110 (1984) 1186-1190.

[181] D.M. Davenport, A. Deshmukh, J.R. Werber, M. Elimelech, High-Pressure Reverse Osmosis for Energy-Efficient Hypersaline Brine Desalination: Current Status, Design Considerations, and Research Needs, Environmental Science & Technology Letters 5 (2018) 467-475.
[182] P.W. Voorhees, THE THEORY OF OSTWALD RIPENING, J. Stat. Phys. 38 (1985) 231-252.
[183] J.F. Anthoni, The chemical composition of seawater, Magnesium 2701 (2006) e9062.
[184] R.D. Shannon, REVISED EFFECTIVE IONIC-RADII AND SYSTEMATIC STUDIES OF INTERATOMIC DISTANCES IN HALIDES AND CHALCOGENIDES, Acta Crystallographica Section A 32 (1976) 751-767.
[185] H.D.B. Jenkins, K.P. Thakur, REAPPRAISAL OF THERMOCHEMICAL RADII FOR COMPLEX-IONS, J. Chem. Educ. 56 (1979) 576-577.
[186] M.J. Qazi, H. Salim, C.A.W. Doorman, E. Jambon-Puillet, N. Shahidzadeh, Salt creeping as a self-amplifying crystallization process, Science Advances 5 (2019).
[187] C. Zhang, H.Q. Liang, Z.K. Xu, Z.K. Wang, Harnessing Solar-Driven Photothermal Effect toward the Water-Energy Nexus, Advanced Science 6 (2019) 1900883.
[188] L.L. Zhu, M.M. Gao, C.K.N. Peh, X.Q. Wang, G.W. Ho, Self-Contained Monolithic Carbon Sponges for Solar-Driven Interfacial Water Evaporation Distillation and Electricity Generation, Adv. Energy Mater. 8 (2018) 1702149.
[189] W.X. Guan, Y.H. Guo, G.H. Yu, Carbon Materials for Solar Water Evaporation and Desalination, Small 17 (2021) 2007176.
[190] S.S. Cao, Q.S. Jiang, X.H. Wu, D. Ghim, H.G. Derami, P.I. Chou, Y.S. Jun, S. Singamaneni, Advances in solar evaporator materials for freshwater generation, J. Mater. Chem. A 7 (2019) 24092-24123.
[191] L.L. Zang, C. Finnerty, S.X. Zheng, K. Conway, L.G. Sun, J. Ma, B.X. Mi, Interfacial solar vapor generation for desalination and brine treatment: Evaluating current strategies of solving scaling, Water Res. 198 (2021) 117135.
[192] L.N. Zhang, X.Y. Li, Y. Zhong, A. Leroy, Z.Y. Xu, L. Zhao, E.N. Wang, Highly efficient and salt rejecting solar evaporation via a wick-free confined water layer, Nat. Commun. 13 (2022) 849.
[193] G.H. Liu, T. Chen, J.L. Xu, G.S. Yao, J. Xie, Y.P. Cheng, Z. Miao, K.Y. Wang, Salt-Rejecting Solar Interfacial Evaporation, Cell Reports Physical Science 2 (2021) 100310.
[194] C. Finnerty, L. Zhang, D.L. Sedlak, K.L. Nelson, B.X. Mi, Synthetic Graphene Oxide Leaf for Solar Desalination with Zero Liquid Discharge, Environ. Sci. Technol. 51 (2017) 11701-11709.
[195] X. Ma, X. Jia, H. Gao, D. Wen, Polypyrrole–Dopamine Nanofiber Light-Trapping Coating for Efficient Solar Vapor Generation, ACS Appl. Mater. Inter. (2021) 57153-57162.
[196] S. Veran-Tissoires, M. Marcoux, M. Prat, Discrete Salt Crystallization at the Surface of a Porous Medium, Phys. Rev. Lett. 108 (2012) 054502.